©Copyright 2021
Ryan Beck

Examination of Defect-Induced Properties in Nanomaterial Systems

Ryan Beck

A dissertation
submitted in partial fulfillment of the
requirements for the degree of

Doctor of Philosophy

University of Washington

2021

Reading Committee:

Xiaosong Li, Chair

Brandi Cossairt

Stefan Stoll

Program Authorized to Offer Degree:
UW Chemistry

University of Washington

Abstract

Examination of Defect-Induced Properties in Nanomaterial Systems

Ryan Beck

Chair of the Supervisory Committee:
Xiaosong Li
Chemistry

Doped, semiconducting nanomaterial systems can be widely used for sensing, spintronic, light harvesting, and display applications to name a few. The ability to tune the response of these systems through modulation of their size or the inclusion of specific atoms and defect centers enables many of these applications. An in-depth understanding of the origin of observed responses, as well as the prediction of the performance of novel systems is highly sought-after. Density functional theory (DFT) is a fairly accurate method which enables examination into systems approaching the experimental size of nanoparticles. In the first part of this work, the spectroscopic signatures of dopants within a nanodiamond lattice are examined. Since nanodiamonds are wide-band-gap semiconductors with a rigid lattice that are stable under large temperatures and pressures, they are an excellent candidate for several applications such as high pressure and temperature sensors. The abiltiy to control the doping within the lattice enables the design of defects with long lasting coherence enabling their use as spin sensors or qubits. The spectroscopic signatures of several of these dopants are examined to see the effects on the vibrational, optical, and X-ray absorption spectroscopies to inform on the structure of these systems, and provide methods for their identification within a given sample. The second part investigates how atomically percise chemical doping can create and control complex magnetic patterns within a 2-D magnetic device.

ACKNOWLEDGMENTS

I would like to express my appreciation to Xiaosong Li, my advisor, for his guidance, patience, and support during my research. The candid discussions of projects, and, most importantly, his willingness to go over the good and the bad of my work have been integral to my growth as a scientist. I would also like to thank the other members of my committee (Ting Cao, Brandi Cossairt, Peter Pauzauskie, and Stefan Stoll) who have provided valuable insights into projects that I have worked on. By asking questions from their wide-ranging backgrounds, they have enabled me me to think beyond the theory and consider problems that I would not have otherwise.

From Xiaosong's group I would like to thank Alessio Petrone, Joseph Kasper, and Hongbin Liu for their support, guidence, and friendship during my first years as they let me bounce ideas off them, and gave helpful insights when my projects seemed to be stuck. I would also like to extend my thanks to the still-present group members, especially Andrew Wildman, Torin Stetina, Lauren Koulias, Chad Hoyer, and Andrew Valentine for their friendship and interesting conversation topics.

Finally, outside of the UW, I would like to thank Kathleen Halligan and James Foresman whose encouragement led me out to Seattle in the first place, and my family whose support (and patience) I would not be here without.

Chapter 1

INTRODUCTION

1.1 Theoretical Computation of Electronic Ground State

1.1.1 Wavefunction Ground State

The start for obtaining theoretical insights into chemical systems starts by solving (or approximately solving) the Schrödinger equation (for the purposes of this discussion time-dependence and relativity are left out):

$$\hat{H} \left|\Psi\right\rangle = E \left|\Psi\right\rangle \tag{1.1}$$

Due to the complexity of solving the full equation, several approximations are used, beginning with the Born–Oppenheimer approximation which decouples the full Hamiltonian into nuclear and electronic components:

$$\hat{H} = \hat{T}_{nuc} + \hat{H}_{el} \tag{1.2}$$

where:

$$\hat{T}_{nuc} = -\sum_{\mu} \frac{1}{2m_{\mu}} \nabla_{\mu}^{2} \tag{1.3}$$

with Z_μ noting the charge on atomic center μ, and:

$$\hat{H}_{el} = -\sum_{i} \frac{1}{2} \nabla_{i}^{2} - \sum_{\mu,i} \frac{Z_{\mu}}{|\mathbf{r}_{\mu} - \mathbf{r}_{i}|} + \sum_{i<j} \frac{1}{|\mathbf{r}_{i} - \mathbf{r}_{j}|} + \sum_{\mu<\nu} \frac{Z_{\mu} Z_{\nu}}{|\mathbf{r}_{\mu} - \mathbf{r}_{\nu}|} \tag{1.4}$$

with $\mathbf{r}_\lambda$ designating the position of particle λ in space, indices i, j running over the electrons, and μ, ν running over the nuclei. The electronic problem can now be solved for a fixed geometry of nuclei leading to the *clamped-nuclei* approximation:

$$\hat{H}_{el}(\mathbf{r},\mathbf{R}) = E_{el}(\mathbf{R})\psi_{el}(\mathbf{r},\mathbf{R}) \tag{1.5}$$

with $\mathbf{r}$ and $\mathbf{R}$ noting electronic and nuclear coordinates, respectively. Thus the energy can be obtained by adding the nuclear kinetic energy ($\hat{T}_{nuc}$) back in:

$$\{\hat{T}_{nuc}(\mathbf{R}) + E_{el}(\mathbf{R})\}\psi_{nuc}(\mathbf{R}) = E_{Tot}\psi_{nuc}(\mathbf{R}) \tag{1.6}$$

Solving for the E_{el} is still quite complex, however, and as such, the following discussion will focus on it, and the *el* subscript is dropped for brevity.

We can further split $\hat{H}$ from Eq. (1.4) into:

$$\hat{H} = \sum_i \hat{h}_i + \sum_{i,j} \hat{g}_{i,j} + \hat{h}_0 \tag{1.7}$$

where the terms now reflect the one-electron, two-electron, and nuclear energy, respectively given by:

$$\hat{h}_i = -\frac{1}{2}\nabla_i^2 - \sum_{\mu} \frac{Z_\mu}{r_{i\mu}} \tag{1.8}$$

$$\hat{g}_{i,j} = \frac{1}{r_{ij}} \tag{1.9}$$

$$\hat{h}_0 = \sum_{\mu<\nu} \frac{Z_\mu Z_\nu}{r_{\mu\nu}} \tag{1.10}$$

The two-electron term ($\hat{g}_{i,j}$) is commonly broken up into Coulomb ($\hat{J}$) and exchange ($\hat{K}$) terms. Unfortunately, we don't know the orbitals yet, and thus variational theory is used to determine the orbitals that minimize E. In order to do so the orbitals are changed by a small (infinitesimal) amount: $\phi_i \to \phi_i + \delta\phi_i$ leading to a change in the total wave function

$\Psi \rightarrow \Psi_i + \delta\Psi_i$. The energy can thus be written:

$$\begin{aligned} E[\Psi + \delta\Psi] = &\sum_i \langle \phi_i + \delta\phi_i | \hat{h} | \phi_i + \delta\phi_i \rangle \\ &+ \frac{1}{2} \sum_{i,j} \langle (\phi_i + \delta\phi_i)(\phi_j + \delta\phi_j) | \hat{g} | (\phi_i + \delta\phi_i)(\phi_j + \delta\phi_j) \rangle \\ &- \frac{1}{2} \sum_{i,j} \langle (\phi_i + \delta\phi_i)(\phi_j + \delta\phi_j) | \hat{g} | (\phi_j + \delta\phi_j)(\phi_i + \delta\phi_i) \rangle \end{aligned} \tag{1.11}$$

In order to get the first-order variation $\delta^{(1)}E[\Psi]$ terms linear in $\delta\phi$ are collected:

$$\begin{aligned} \delta^{(1)}E[\Psi] &= \sum_i \langle \delta\phi_i | \hat{h} | \phi_i \rangle + \sum_{i,j} \{ \langle \delta\phi_i \phi_j | \hat{g} | \phi_i \phi_j \rangle - \langle \delta\phi_i \phi_j | \hat{g} | \phi_j \phi_i \rangle \} + c.c. \\ &= \sum_i \langle \delta\phi_i | \hat{h} | \phi_i \rangle + \sum_i \{ \langle \delta\phi_i | \hat{J} - \hat{K} | \phi_i \rangle \} + c.c. \\ &= \sum_i \langle \delta\phi_i | \hat{F} | \phi_i \rangle + c.c. \end{aligned} \tag{1.12}$$

where *c.c.* is the complex conjugate. The term $\hat{F}$ is the Fock operator ($\hat{F} = \hat{h} + \hat{J} - \hat{K}$), and the energy minimum can only exist when the variation ($\delta^{(1)}E$) vanishes. Writing $\delta\phi_i$ in terms of occupied (ϕ_j) and unoccupied (ϕ_a) molecular orbitals (MOs):

$$\delta\phi_i = \sum_i \alpha_{i,j}\phi_j + \sum_a \alpha_{i,a}\phi_a \tag{1.13}$$

with α being an infinitesimal quantity. The first term describes an infinitesimal transformation of the occupied MOs leaving Ψ unchanged, but the second term leads to:

$$\langle \phi_a | \hat{F} | \phi_i \rangle = 0 \tag{1.14}$$

which is the general Hartree-Fock equation. If Eq. (1.14) is written as:

$$\hat{F}\phi_i = \sum_k \lambda_{k,i}\phi_k \tag{1.15}$$

where k runs over all occupied MOs. If a new matrix diagonializing λ (V) is introduced, new MOs can be formed by:

$$\widetilde{\phi}_j = \sum_i \phi_i V_{ij} \tag{1.16}$$

which leads to the most common form of the Hartree–Fock equations:

$$\hat{F}\widetilde{\phi}_j = \epsilon_j \widetilde{\phi}_j \tag{1.17}$$

From which, the total energy can be obtained:

$$E = \sum_i \epsilon_i - \frac{1}{2}\sum_i \langle \phi_i | \hat{J} - \hat{K} | \phi_i \rangle \tag{1.18}$$

It should be noted that all variations to the MOs need to maintain orthonormality.[1, 2]

1.1.2 Density Functional Theory Ground State

Unfortunately, for systems containing large numbers of nuclei and electrons, the scaling for wavefunction-based methods becomes untenable. As such density functional theory (DFT) was introduced. DFT is able to take the many-body problem of N-interacting electrons and reduce it into a problem of non-interacting electrons within a static potential containing the Coulomb and exchange/correlation terms. Rewriting Eq. (1.7) as:

$$\hat{H} = \hat{T} + \hat{W}_{ee} + \hat{V}_{ne} \tag{1.19}$$

with $\hat{T}$ being the kinetic-energy operator, $\hat{W}_{ee}$ the electron–electron interaction operator, and $\hat{V}_{ne}$ the nuclei–electron interaction operator. The idea for DFT is to reformulate the variational theorem to be in terms of the electron density, given by:

$$n(\mathbf{r}) = N \int |\Psi(x_1, x_2, ..., x_N)|^2 d\sigma_1, dx_2, ..., dx_N \tag{1.20}$$

which is normalized so that the integral over all space returns the number of electrons in the system ($\int n(\mathbf{r})d\mathbf{r} = N$).

If an applied external potential ($v(\mathbf{r})$) can be applied to a system in place of the nuclear-electron potential ($v_{ne}(\mathbf{r})$), a ground-state density can be obtained by solving the Schrödinger equation. In 1964 Hohenberg and Kohn showed that the mapping can be inverted (e.g. $n(\mathbf{r}) \rightarrow v(\mathbf{r}) + const.$) and also conclude that two local potentials differing by more than an additive constant cannot share the same ground-state wave function.[3] Thus the ground-state density determines the potential which then determines the Hamiltonian. The potential is a unique (up to an additive constant) functional of the ground state density. Thus, the ground-state wave function for a given potential is a functional of n which can be used to define the universal density functional:

$$F[n] = \langle \psi[n] | \hat{T} + \hat{W}_{ee} | \psi[n] \rangle \tag{1.21}$$

which can be used to define the total electronic energy functional:

$$E[n] = F[n] + \int v_{ne}(\mathbf{r}) n(\mathbf{r}) d\mathbf{r} \tag{1.22}$$

for the specific external potential, $v_{ne}(\mathbf{r})$, of the system considered. The energy is variational so the minimum energy can be given as:

$$E_0 = \min_n \left\{ F[n] + \int v_{ne}(\mathbf{r}) n(\mathbf{r}) d\mathbf{r} \right\} \tag{1.23}$$

The existence of both a mapping from a ground-state density to a local potential, and the universal density functional, along with the variational behavior of the energy with respect to the density constitutes the Hohenberg-Kohn theory.[3] Unfortunately, the exact form for the universal functional is unknown, with the difficulty of approximating the functional Kohn and Sham proposed to decompose the functional as:[4]

$$F[n] = T_s[n] + E_{HXC}[n] \tag{1.24}$$

where $T_s[n]$ is the kinetic-energy functional and $E_{HXC}[n]$ is the Hartree–exchange–correlation functional.$T_s[n]$ can be defined with a constrained-search formulation:

$$T_s[n] = \langle\Phi[n]|\,\hat{T}\,|\Phi[n]\rangle \tag{1.25}$$

where Φ are normalized single-determinant wave functions yielding a fixed density n. For a given density, the minimizing $\Phi[n]$ is called the KS wave function. The KS method is thus able to express $F[n]$ in terms of single-determinate wave functions:

$$E_0 = \min_{\Phi}\{\langle\Phi|\,\hat{T} + \hat{V}_{ne}\,|\Phi\rangle + E_{HXC}[n_\Phi]\} \tag{1.26}$$

While a wavefunction has been reintroduced compared to Eq. (1.23), since it is only a single-determine wave function it still simplifies a multi-determinant wavefunction (Ψ). In addition, since the T_s term can be treated explicitly, only the $E_{HXC}[n]$ requires approximation in terms of the density. $E_{HXC}[n]$ is written as:

$$E_{HXC}[n] = E_H[n] + E_{XC}[n] \tag{1.27}$$

where $E_H[n]$ is the Hartree energy functional given by:

$$E_H[n] = \frac{1}{2}\int\int \frac{n(\mathbf{r}_1)n(\mathbf{r}_2)}{|\mathbf{r}_{12}|}d\mathbf{r}_1 d\mathbf{r}_2 \tag{1.28}$$

giving the classical electrostatic repulsion for the charge distribution. The exchange-correlation energy is thus left to be approximated. A commonly-used approximation for this, named the generalized-gradient approximation or GGA, expresses E_{XC} as:

$$E_{XC}^{GGA}[n] = \int f(n(\mathbf{r}), \nabla n(\mathbf{r}))d\mathbf{r} \tag{1.29}$$

where f is a determined function. GGAs are considered semi-local approximations since it depends on both the density and the gradient of the density. Examples include, but are not limited to, the B88 exchange functional,[5] the LYP correlation functional[6], and the PBE exchange-correlation functional.[7] This then lead to mixing of the exact (Hartree-Fock) exchange with GGA functionals. One of the more common so-called ‘hybrid functionals’ was proposed by Becke in 1993 including a three-parameter hybrid approximation taking the form:[8]

$$E_{XC}^{3H} = aE_X^{HF} + bE_X^{GGA} + (1 - a - b)E_X^{LDA} + cE_c^{GGA} + (1 - c)E_C^{LDA} \tag{1.30}$$

where the three parameters a, b, c are determined through fitting to experimental data. For large molecules, however, an additional approximation (range-separation) is often included where the amount of the included exchange is tempered by the distance between centers. This leads to methods such as the Coulomb-attenuating method (CAM) taking the form:

$$E_{XC}^{CAM} = aE_X^{sr,HF} + bE_X^{lr,HF} + (1 - a)E_X^{sr,DFA} + (1 - b)E_X^{lr,DFA} + cE_c^{DFA} \tag{1.31}$$

with sr and lr being for the short- and long-range interactions. The inclusion of HF exchange at short range can help improve thermodynamic properties.[2, 9]

1.2 Nanomaterials

With the ability of DFT to accurately handle large systems, a field of intense recent study has been semiconductor nanoparticles for their wide range of uses in applications such as sensing, imaging, signal- generating, and photon conversion to name a few.[10–15] They become especially interesting when either defects (impurities in the nanocrystal structure) or dopants (a defect containing a different atom than expected in the nanocrystal structure) are present as this can lead to unique properties and selection rules in comparison to the bulk structure. In addition to being able to control the properties and selection rules of the systems by introducing defects and dopants, the resulting properties can often be further tuned through modulating the size of the nanocrystals. Largely due to the quantum confinement effect, this results in highly-controllable materials that can be fine-tuned for many applications.

In order to most effectively generate these devices, however, theoretical insights are required. Theory can give the energies for formation, molecular insights into observed absorption and emission features, and information about lifetimes of excitations lending insight into the structure and how of defect formations, the why of observed spectral responses, and the how long or even where-to of excited states. These observations provide valuable insight to experimentally-generated (and in some cases fully-theoretical) systems and can help lead to better materials or more efficient designs.

Chapter 2

DEFECTS IN DIAMOND

2.1 Diamond Introduction

Nanodiamonds are interesting materials due to their stability which allows the use in biological imaging, quantum computing, drug delivery, and sensing due to their lack of photobleaching, spin polarized photoluminescence, and long spin lifetimes when doped.[10–13, 16–20] Bulk, undoped diamonds are insulators with a band gap of approximately 5.5 eV,[21] and have a very dense lattice that both restricts defect diffusion and phase transitions at high temperatures. When the crystal size approaches the nano-dimension ($\sim$5 nm), diamonds no longer express bulk properties. A band gap opening is observed and discrete electronic levels (typical of molecules) emerge at band edges. These are all consequences of the quantum confinement effect.[13, 22–30] Therefore, the interaction between diamonds and light may be modulated by adjusting the host nanocrystal size. In addition, implanting dopants into the lattice, such as the nitrogen vacancy and silicon split divacancy, or the presence of surface defects can lead to unique and tunable optical and vibrational signatures.[10, 31–36]

2.2 Methodology

Nanodiamonds were constructed to be nearly spherical with a bulk fcc lattice parameter of $a = 0.357$ nm[21] according to the procedure presented in Ref. 31. Hydrogen was chosen to passivate the surface carbon dangling bonds, given that hydrogen surface termination can be realized experimentally using a hydrogen plasma process.[10, 37, 38] Other moieties such as those containing oxygen and nitrogen are commonly found on the surface as a byproduct of the manufacturing and purification methods including the detonation of high explosives, high pressure high temperature multi-anvil press, and, most recently, laser-heated diamond anvil cells (LH-DAC).[10, 33, 39, 40] The unique use of noble gas pressure media during LH-DAC processing, however, maximizes the probability of graphitic surface reconstruction.

Before hydrogen removal or defect implantation the diamonds have C_{3v} symmetry and three sizes, ~1.4 nm ($C_{182}H_{142}$), ~1.2 nm ($C_{121}H_{104}$), and ~0.8 nm ($C_{44}H_{42}$) in diameter diamond clusters, have been used throughout. These systems are similar, but slightly smaller, than commercially available nanodiamonds from laser-heated diamond anvil cell synthesis or detonation synthesis.[10, 33, 39] Given that the Bohr exciton radius for diamond is ~1.6 nm[41], the electronic properties of these diamond clusters are expected to exhibit quantum confinement effects.[31] Calculations were performed using the Gaussian electronic structure software package.[42] To ensure that the optimized structures represent physically valid models, XAS and Raman vibrational spectra were computed and compared to experimental results.

The electronic structures of excited states were calculated using TDDFT within the linear response framework[43–45] and its energy specific implementation for the high-energy states.[46–48] Transitions for X-ray absorption spectroscopy (XAS) were uniformly shifted[47] in discussions, reported spectra, and tables so as to better compare with experimentally obtained results for the onset of the pure bulk diamond carbon K-edge obtained with both electron energy loss spectroscopy[17, 49]and XAS.[16, 50]

2.3 Surface Defects

Reprinted with permission from R. Beck, A. Petrone, J. M. Kasper, M. Crane, P. Pauzauskie, X. Li *J. Phys. Chem. C.*, 122, 8573-8580, **2018** copyright 2018 American Chemical Society.[35]

2.3.1 Diamond Surface Introduction

In diamond, carbon is arranged into a highly symmetric, tetrahedral, sp^3 lattice. However due to graphitic pre-edge features that appear in the carbon K-edge energy region of X-ray and electron energy loss spectroscopy of nanodiamonds, it has been theorized that as diamond approaches the nano-scale the surface carbons arrange to form sp^2 features.[16, 33, 50, 51] Briefly, earlier theories on the arrangement of the carbons predicted a diamond core with a graphitic shell around it.[10, 52] This model for describing the surface of the diamond still cannot describe an experimentally determined deviation from perfect lattice Bragg peaks.[52] Thus an improved model was proposed where nanodiamonds arrange themselves in a manner similar to that in Fig. 2.1.[10, 52] In this model, there is an sp^3 diamond core surrounded by a shell of sp^3 carbon atoms where the diamond lattice deviates from its perfect tetrahedral arrangement, labeled S_2 in the figure. Finally, this intermediate shell interacts with the graphitic, sp^2, surface layer, labeled S_1 in the figure.[52]

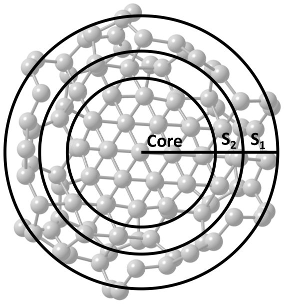

Figure 2.1: The proposed model for nanodiamond surface reorganization comprised of a diamond lattice core, a layer of sp^3 carbons but where the diamond lattice deteriorates (S_2), and the surface (S_1).[10, 52]

Surface rearrangement, and thus the carbon hybridization, of nanodiamonds has been used to describe experimentally determined features on optical spectra, such as the carbon X-ray absorption 285 eV pre-edge.[16, 33, 50, 53] In the past few years, the effects of the surface passivation, symmetry, and functionalization on the diamond lattice reorganization have been also computationally studied.[49, 54–57] However, a detailed understanding of the interplay between the surface rearrangement (i.e. sp^2 moieties, graphitic and sp^3 strained layers) and the presence of localized defects in the lattice (i.e. dopants)[52] on the pre-edge features that appear in the carbon K-edge energy region of the X-ray absorbance spectrum is still not fully accomplished.

Thus, the effect of different surface hybridizations on the Raman scattering vibrational spectroscopy and X-ray absorption are examined using a finite-cluster approach and the effect of different surface hybridizations on optical properties is investigated. Rearrangement of the surface carbon hybridization is predicted through the structural response to different surface passivations.

2.3.2 Diamond Surface Methodology

The ground-state electronic structures were obtained by solving the Kohn-Sham equation using the hybrid Becke, 3-parameter, Lee-Yang-Parr (B3LYP) functional[6, 8, 58] with a 6-31g(d) basis. The theory level employed has been previously validated for the description of the electronic structure and optical properties of both pure and nitrogen vacancy doped diamonds of the same dimensions.[31] To examine the effects of the surface passivation on the diamond lattice as the surface becomes more unsaturated, hydrogens were removed from the surface and the resulting structure was fully optimized.[59] This surface reorganization is analogous to what has been hypothesized to occur when nanodiamonds are synthesized within a laser-heated diamond anvil cell that uses a noble gas (i.e., neon, argon) as the near-hydrostatic pressure medium.[33] Hydrogens were removed in such a way so as to preserve the symmetry of the unoptimized structures and to obtain a homogeneous hydrogen density across the surface of the nanodiamond (see Fig. 2.2).

To verify the structure returned from the optimization were true minima, and to compute the vibrational frequencies, the second derivatives of the energy with respect to the Cartesian

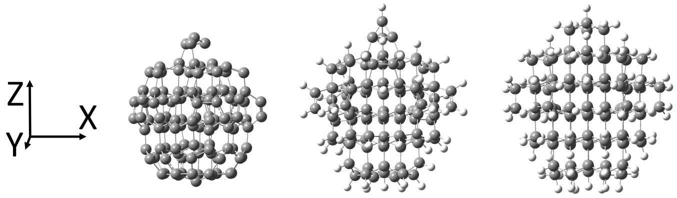

Figure 2.2: From left to right the B3LYP/6-31G(d) optimized $C_{121}H_0$, $C_{121}H_{58}$, and $C_{121}H_{104}$ diamond structures.

nuclear coordinates were calculated. Given the number of atoms and possible arrangements of the systems studied, there are several structures with similar bonding structures and degenerate energies that can result from the optimizations. A detailed analysis of the surface reorganization for the differently passivated nanodiamonds is presented providing a comparison with previous computational studies on diamonds of similar sizes.[16, 49, 57] The average computed properties over each optimized nanodiamond structure are similar and representative of experimental data, suggesting that the results presented herein are valid.

To compare the amount of tetrahedral character exhibited by different diamond atoms within the core and surface of a nanodiamond, and between nanodiamonds with different levels of surface passivation, the average carbon–carbon bond distance at different distances from the origin of the nanodiamond was examined. The average deviation from an ideal tetrahedral bond angle (109.5°) subtended at each carbon center was examined in addition to the bond length to show either the existence of a tetrahedral lattice, or the degradation of the lattice. Three surface passivations were analyzed for the 1.2 nm nanodiamond, where the surface has 0% (no hydrogens), 50%, and 100% (all surface carbon atoms are bound with hydrogens) of the original hydrogen passivation.

2.3.3 Structural Reorganization

The lattice structural reorganization and resulting surface layouts are summarized as functions of the different degrees of hydrogen passivation (0, 50, 100%) in Fig. 2.3, where the average bond length (top panels) and bond angle deviation (bottom panels) are shown. An

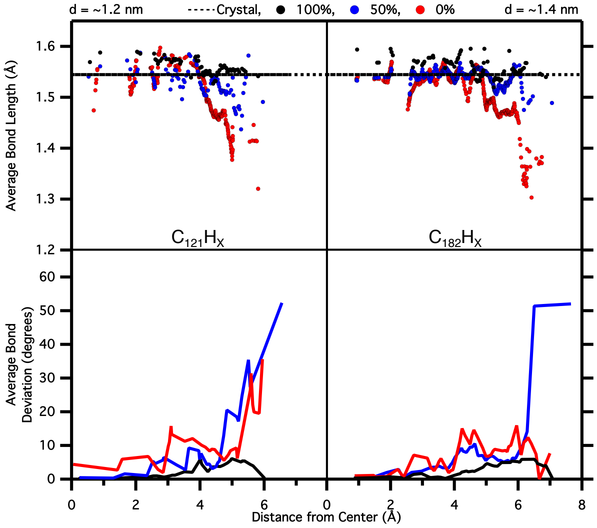

Figure 2.3: The bond lengths as a function of the distance from the center(top), and the root mean square deviation from the perfect tetrahedral bond angle of 109.5° (bottom) as a function of the distance from the center of the C_{121} diamond, left, and the C_{182} diamond, right are reported. The dashed line marks the crystallographic bond length of 1.54 Å.

overall lattice strain, a slight elongation of the carbon-carbon bonds with respect to the bulk, is still observed for the core atoms in all models, suggesting that these atoms are sensitive to the surface tension given the size of the nanodiamonds. Through the examination of Fig. 2.3, it is clear the studied nanodiamonds do not preserve a perfect tetrahedral sp^3 bond character through the entire structure as surface passivation is lost.

This model shows that the surface begins to undergo reconstructions when half of the hydrogens are removed. In this system, the carbon-carbon bond lengths at the surface of the nanodiamond, 5 Å to 6 Å from the center, decrease dramatically from $\sim$1.5 Å to $\sim$1.4 Å and from 1.5 Å to $\sim$1.3 Å for the 50 and 0% surface passivated nanodiamonds, respectively. A surface layer of $\sim$2 Å in width can be attributed to the studied systems, since the bond length begins to decrease significantly at $\sim$4 Å from the center of the nanodiamond which has a total radius of $\sim$6 Å. The bond length analysis presented here is very sensitive to the change of the carbon hybridization and therefore is very useful in highlighting the loss of sp^3 character at the surface carbon atoms. On the other hand, the bond length is less sensitive to the strained layer of sp^3 carbon (see Fig. 2.1).

To capture in a more detailed way the loss of tetrahedral character of the carbons beneath the surface of the nanodiamonds, the absolute deviation from tetrahedral bond angles, as a function of the distance from the center of the nanodiamond, is reported in Fig. 2.3. Examining the 1.2 nm nanodiamond, there is a dramatic loss of tetrahedral character starting ∼4 Å from the center of the nanodiamond shown as a sharp increase in the deviation from the ideal tetrahedral bond angle (109.5°). This further indicates the presence of a surface layer in both the 0% and 50% cases, in agreement with bond length analysis. When the nanodiamond surface is fully passivated by hydrogens, a limited deviation of the bond angles is found, showing that the tetrahedral lattice persists through the entire structure. On the other hand, when the nanodiamond has half of the surface hydrogens, there is already a significant deviation in the bond angles starting at a ∼2 Å distance from the surface. Moreover, when all of the hydrogens have been removed there is a region at ∼3 Å from the surface of the nanodiamond where the bonds are still in the tetrahedral bonding regime, according to their bond lengths, but their bond angles deviate from their tetrahedral value (109.5°). This is the first evidence, in this work, of the presence of the S_2 layer (see Fig. 2.1) in nanodiamonds. The 1.2 nm nanodiamonds thus consists of a surface layer of ∼3 Å in size where the sp^3 hybridization of the carbon atoms is no longer present, and is further comprised of both the S_1 and S_2 layers (see Fig. 2.1).

A similar result can be found for the 1.4 nm diamond, Fig. 2.3 (right panels). It is interesting to note that the bond angle deviation for the 1.4 nm 0% hydrogen passivated diamond is significantly less than in the corresponding 1.2 nm nanodiamond. Upon closer inspection of the resulting optimized structures, formation of a fullerene-like structure forming on the surface can be observed in the 1.4 nm system. This structure may be unable to form on the 1.2 nm nanodiamond as it may not be large enough to sustain the structure due to a larger surface tension present in smaller nanodiamonds. The dependence of this sp^2 surface formation on the size and shape of the nanodiamonds, along with the presence of graphitic/fullerene structures has been previously observed.[16, 49, 57] For both 1.2 and 1.4 nm nanodiamonds, when the surface has only 50% of the original hydrogen passivation there is a significant deviation from the tetrahedral bond angle close to the surface. This observed deviation is due to the formation of non-interacting sp^2 bonds on the surface,

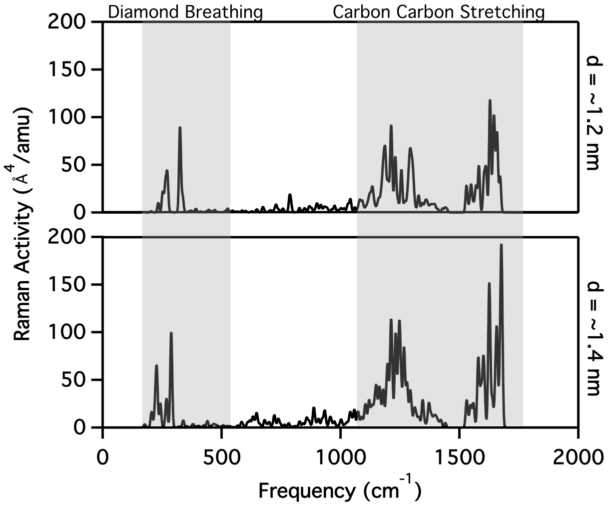

Figure 2.4: B3LYP/6-31G(d) Raman spectra for the 1.2 and 1.4 nm diameter fully hydrogen passivated nanodiamonds. The high-energy carbon–hydrogen stretches (3000 cm^{-1}) are not shown. Raman activity has a 4 cm^{-1} broadening applied to generate the spectra for both plots.

given the uniform hydrogen distribution scheme used in our models, that greatly distort the existing tetrahedral centers. This deviation is lessened in the 0% hydrogen cases as a more uniform graphitic structure is able to form on the surface. Given the 1.2 nm and 1.4 nm nanodiamonds undergo a similar surface reconstruction the vibrational and X-ray absorption analyses were preformed on the spectra resulting from the 1.2 nm nanodiamond.

2.3.4 Vibrational Analysis

Vibrational spectra, most notably Raman, can be used to identify the size and structure of nanodiamonds, as well as their surface structure and composition.[60–63] Raman spectroscopy is sensitive to different carbon allotropes differing between various structures such as diamond, graphite, and amorphous carbons, through the appearance and shapes of various bands in separate regions of the vibrational spectrum.[60–62, 64] Two bands corresponding to the breathing mode of nanodiamond and lattice carbon–carbon stretching mode energy regions are marked in Fig. 2.4. Note that in the lattice carbon–carbon stretching region there is an overlap with hydrogen–carbon-hydrogen bending modes responsible for the two bands. The high energy carbon–hydrogen stretching peaks ($\sim$3000 cm^{-1}) are not of interest in this study and are thus not shown in the figure. In Fig. 2.4 are the fully hydrogen passivated Raman spectra for the 1.2 nm and 1.4 nm nanodiamonds. In particular, the measured Raman spectrum of nanodiamonds between 1200 and 1800 cm^{-1} has attracted attention given its complex nature due to several characteristic features:[63, 65–67] (a) the first order Raman mode of the cubic diamond lattice which appears broader and red-shifted ($\sim$1325 cm^{-1}) with respect to the bulk diamonds. This has been observed as the main spectral feature in this region for diamonds that have been fully passivated by hydrogen.[68, 69] (b) The so called "D-band" around 1400 cm^{-1} attributed to disorder and amorphous sp^2 carbons (mostly breathing motions). (c) A broad asymmetric peak between 1500 and 1800 cm^{-1} most often labeled as the "G-band" and assigned to the in-plane vibrations of graphitic carbon.[63, 70, 71] However, this peak in nanodiamonds differs from the G-band of graphitic materials both in shape and position.[72] The character of this "G-band" is still under debate in diamond approaching the nanosize and has been either attributed to mixed sp^2/sp^3 carbon structures,[73] or referred as a peak of sp^2 clusters,[74] without additional explanation of their exact nature (i.e. amorphous, graphitic, etc.). There also have been attempts to attribute these peaks to carbon carbon double bonded pairs (C=C) within the lattice.[75, 76] The lower energy ($\sim$ 350 cm^{-1}) diamond breathing mode has been shown to have a size dependence. This is seen through a slight redshift with increasing size of nanodiamond, with a more in-depth investigation of this peak having been done previously.[60, 61] This peak is examined as a function of decreasing surface passivation and the Raman spectra at the energy region of interest for the three surface passivations is plotted in Fig. 2.5. For the 100% and 50% hydrogen passivated surfaces this peak is shown to not alter drastically, however with the removal of all the surface passivation this band grows in intensity.

Examining the lattice carbon–carbon stretching region ($\sim$1300 cm^{-1}) in Fig. 2.4, two separate bands can be identified. These bands are due to hydrogen–carbon–hydrogen bending modes overlapping with carbon–carbon stretching modes. The obscuring of the carbon–carbon stretches has been noted in previous vibrational studies of nanodiamonds and has been addressed by artificially increasing the mass of the hydrogen atoms (to 100 amu) so

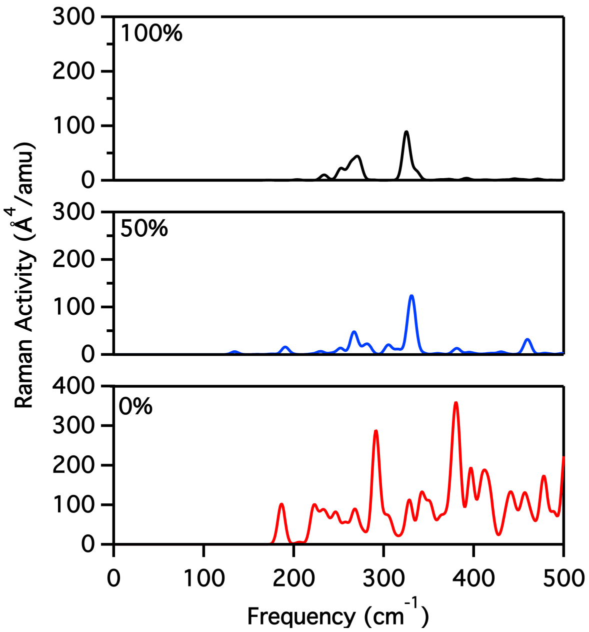

Figure 2.5: Diamond lattice breathing region of the B3LYP/6-31G(d) Raman spectra for the 100%, 50%, and 0% in black, blue, and red, respectively. Raman activity has had a 4 cm^{-1} broadening applied to generate the spectra for all three plots.

as to shift their response away from the carbon-carbon stretching energy regions.[60, 64] The Raman spectra with the heavy hydrogen for the 100%, 50%, and 0% surface passivated surfaces are plotted in Fig. 2.6. In the case where the nanodiamond has 100% surface hydrogen passivation a band is seen at 1318 cm^{-1}. This band is commonly referred to as the Raman diamond band and is seen in diamond samples as a sharp peak but, as previously mentioned, at the nanoscale the band has been observed to decrease in intensity, and a 10-20 cm^{-1} redshift of this peak (1325 cm^{-1})[66, 68, 69] is observed. Thus, our value of 1318 cm^{-1} shows a good agreement with the experiments. When part, or all, of the surface hydrogen is removed this band decreases in intensity and broadens in agreement with the Raman spectrum of nanodiamonds.[63, 65–67] A “D-band” around 1400 cm^{-1} starts to arise, and is attributed to disorder and amorphous sp^2 carbons (mostly breathing motions), as can be inferred from Fig. 2.4. This “D-band” appears in both the 50% and 0% models, because of the presence of amorphous sp^2 carbon giving rise to mixed sp^2 and sp^3 carbon ring breathing motions, in agreement with previous studies.[63] In our work concerning the "G-band" region, the 0% model shows a red shifted value for this band at 1564 cm^{-1}. Since the 0% coverage cannot support a truly graphitic structure on the surface, but rather sp^2 rings, mixed sp^2 rings, mixed sp^2/sp^3 rings and chains causing softer vibrational modes to appear, this is consistent with the "amorphous" sp^2, or disordered graphitic layer, interpretation of this peak for nanostructures.[63, 73, 74] The 50% model shows instead no vibrational modes between ~1470 and ~1650 cm^{-1} as the surface is forming more amorphous and isolated sp^2 features given the modeling strategy of uniformly passivating the surface with hydrogen. In addition, two isolated peaks are observed at ~1530 and ~1727 cm^{-1} (values using regular hydrogen mass are reported, since these two peaks show greater sensitivity to the hydrogen mass in contrast to those below ~1450 cm^{-1}) for the 50% model due to isolated sp^2 moieties that are supported by this model. The peak at ~1530 is ascribed to a breathing motion of a four membered carbon cage which resembles previously performed calculations and experiments on caged structures of similar size (~1580 cm^{-1}).[77, 78] The ~1727 cm^{-1} feature is due to isolated C=C double bond stretching and H-C=C-H bending mixed modes which happen to be blue shifted from the experimental Raman response for the C=C stretching motion (1622 cm^{-1}).[79] These shifts may be due to the harmonic treatment used in our work. However, in synthetic or natural diamond these regions might contain several modes from surface moieties such as carboxyl and hydroxyl groups, making the overall vibrational analysis even more complex.[67]

As the surface of the nanodiamond loses hydrogen atoms and begins to form graphitic structures, low energy breathing modes of the diamonds increase in their spectral response and additional bands are observed in the Raman spectra. For diamonds synthesized through detonations or in a multi-anvil press, however, significant differences in the Raman cross section of different surface moieties overshadow and obscure each other; though, diamonds synthesized with a laser-heated diamond anvil cell likely have the lowest degree of surface hydrogen or oxygen bonding due to the use of chemically inert noble gasses (neon, argon) as near-hydrostatic pressure media. A more specific analytical method is thus required to characterize these nanodiamonds.

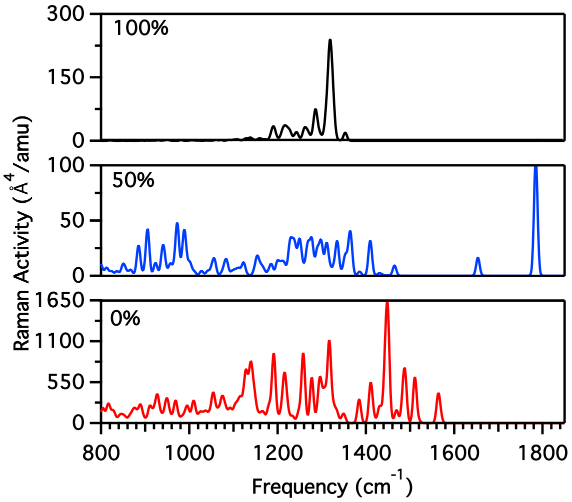

Figure 2.6: B3LYP/6-31G(d) Raman spectra of the diamond lattice carbon-carbon stretching region (800-1650 cm^{-1}) for the 0%, 50%, and 100% nanodiamonds (shown in red, blue, and black, respectively). A carbon carbon triple bonding peak is not shown at 2100 cm^{-1} in the 0% hydrogen nanodiamond spectrum. Raman activity has a 4 cm^{-1} broadening applied to generate the spectra for all three plots.

2.3.5 X-ray Carbon-K edge

X-ray absorption spectroscopy is an ideal spectroscopic technique because it is highly sensitive to both elemental composition and local changes in the molecular structures as electronic transitions from atomic core electrons to weakly bound states are involved.[80] In nanodiamond, XAS has been used to characterize heteroatomic dopants and study surface reconstruction.[50, 81] In this particular study, the different surface reconstructions can be probed by the different transitions involving carbon 1s core electrons and the electronic states involving the different antibonding molecular orbitals laying on the surface. To provide insights to the experimental X-ray data[33, 50], theoretical calculations are required to correlate the observed transitions with the molecular orbitals involved. The excited state orbitals involved in these transitions for nanodiamond typically have σ^* properties if located on sp^3 carbons or can be π^* and σ^* if they are centered on sp^2 carbons, when these are present. Thus electronic excitations in the carbon K-edge, which involves transitions from carbon 1s orbitals to virtual orbitals, were computed and analyzed. Once these transitions are computed, determining if the spatial extent of the virtual molecular orbitals involved in the transition exhibits π^* or σ^* character enables a direct correlation between the surface structure and X-ray spectral features. The resulting carbon K-edge X-ray absorption spectra from the 1.2 nm nanodiamond with 100%, 50%, and 0% hydrogen passivation are shown in Fig. 2.7.

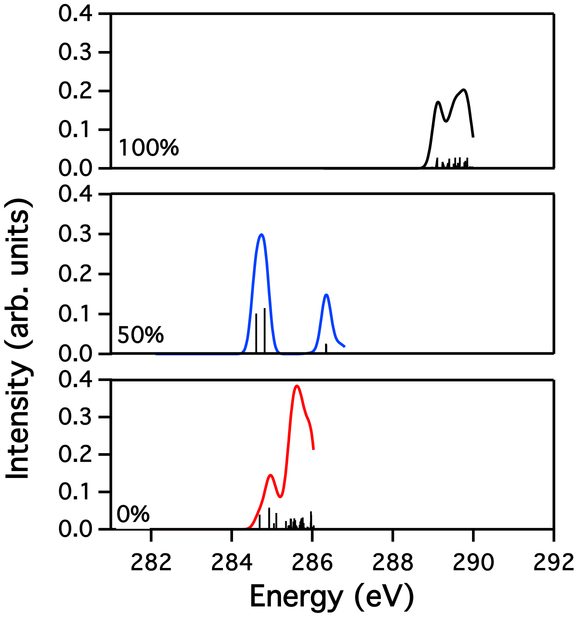

Figure 2.7: LR-B3LYP/6-31G(d) XAS for the optimized C_{121} diamond with 100%, 50%, and 0% surface passivation, in red, green, and blue respectively. A Gaussian broadening has been applied to the individual transitions labeled with black lines to form the spectrum with a full width half maximum value of 0.12 eV along with a uniform shift of 12 eV to align the computed results with the experiments. For the 100% diamond 35 unconverged states of the calculated 272 states were pruned, along with 14 unconverged states of the 121 states calculated for the 50% diamond.

When the surface is fully passivated the first transition in the carbon K-edge region is localized at 289 eV and is of the type carbon $1s \rightarrow \sigma^*$, determined through studying the molecular orbitals (plotted in Fig. 2.8). Upon loss of half of the surface passivation the surface forms sp^2 hybridized carbons. This rearrangement alters the calculated X-ray spectrum so that transitions around 285 eV arise, which is red-shifted from the sp^3 transition in pure diamond at 289 eV by approximately 4 eV indicating that the presence of sp^2

carbon is, at least partially, responsible for the experimentally observed pre-edge feature in synthesized nanodiamond[16, 53, 82]. The pre-edge features are due to carbon $1s \rightarrow \pi^*$ (shown in Fig. 2.8). For the 0% nanodiamond, the first peak is again red-shifted from the 100% surface passivated nanodiamond by about 4 eV to 285 eV and the excitations are still carbon $1s \rightarrow \pi^*$ (shown in Fig. 2.8) similar to the 50% surface passivated nanodiamond. The appearance of transitions that are red-shifted upon the loss of the surface passivation indicates that the shifted peak is dependent on the surface hybridization of the nanodiamond. In the case of both the 0% and 50% surface passivations, a second pre-edge feature arises (at ∼285.5 eV and at ∼286.7 eV for the 0% and 50%, respectively) which are still due to carbon 1s $\rightarrow \pi$*. These features differ from the first appearing features (at ∼285 eV) only in the spacial localization, with respect to the surface of the nanodiamond, of the virtual (arriving) orbitals mostly involved in the corresponding transitions. Therefore, as the surface of the nanodiamond becomes increasingly graphitized, through either heating or chemical treatment, an increase of this pre-edge feature is expected, proportional to the amount of sp^2 carbon.

2.3.6 Conclusions

Nanodiamond nanocrystals were modeled and examined in order to see how different surface layouts can affect the crystallinity of the diamonds as the systems approach the nanoscale. The nanodiamonds were found to form a ∼3 Å surface comprised of a layer of sp^2 hybridized carbon and a strained layer of sp^3 carbon, while the core of the nanodiamond remained in an sp^3 tetrahedral lattice to form the structure pictured in Fig. 2.1 as hydrogen atoms were removed from the surface. The spectroscopic fingerprints of nanodiamond in both the vibrational and X-ray absorption spectra were therefore analyzed to find evidence of this rearrangement. This rearrangement showed a response in the vibrational spectra as the appearance of sp^2 stretching vibrations in the Raman G band (∼1500 cm^{-1}), and a broadening of the Raman diamond band (1330 cm^{-1}). The significant sp^2 character present in unpassivated nanodiamonds has the effect of changing the X-ray absorption spectrum to show carbon $1s$ to π^* electronic transitions, absent in the calculated spectra for the

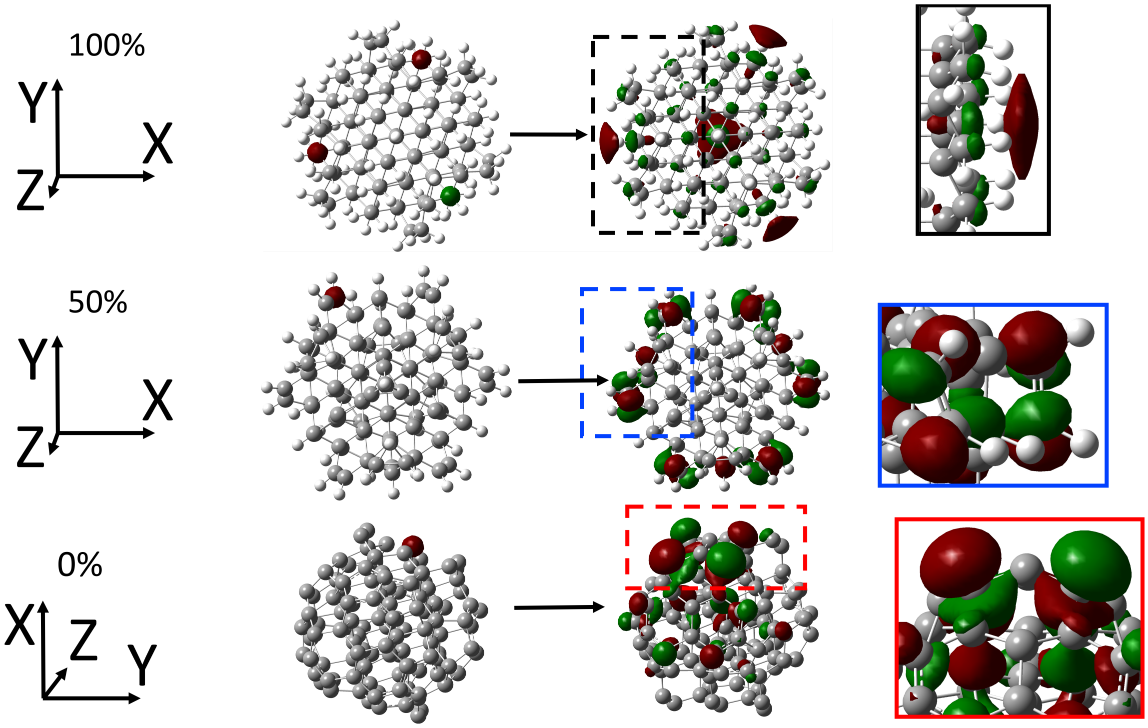

Figure 2.8: B3LYP/6-31G(d) molecular orbitals for the first transition in the carbon K-edge shown in Fig. 2.7 for the 100%, 50%, and 0% nanodiamonds, plotted with an isovalue of 0.025.

fully passivated systems. Thus surface rearrangement is responsible for observed pre-edge features (5 eV lower in energy peak) of the X-ray absorption carbon K-edge spectra of nanodiamonds and which was correlated to the carbon 1s to π^* electronic transitions.

2.4 The Silicon Split Vacancy

Reprinted with permission from A. Petrone, R. A. Beck, J. M. Kasper, X. Li, Y. Huang, M. Crane, and P. Pauzauskie, *Phys. Rev. B*, 98, 205405, **2018** copyright 2018 by the American Physical Society.[34]

2.4.1 Silicon Split Vacancy Introduction

Substitutional nitrogen and nitrogen–vacancy centers are common defects in diamond and have received attention for their sensitive optical and spin properties.[10, 12, 19, 20, 83–85] The peculiar low diffusion rate of NV centers enables the optical probing of local variations in time, which can affect the spin precession rate of the defects, making them suitable for quantum sensing applications.[86] Doping introduces new sub-band-gap levels, and it has been shown that NV centers in diamond give rise to new dopant-centered $sp^3 - sp^3$ mid-gap electronic transitions and charge-transfer (CT or "photoionization") excited states.[31] Similar applications in quantum information processing[87] have been shown for the negatively-charged silicon–vacancy (SiV^-) center due to its short fluorescent lifetime, narrow emission line-width, and high percentage of photons (∼70-80%) emitted through its zero-phonon line (ZPL).[88, 89] This defect has also been shown to be useful as a high-resolution high-pressure sensor.[90] Doped diamond based pressure probes can function at higher pressures than the currently used ruby sensors, as the rigid diamond lattice is still present above 100 GPa, while ruby undergoes a phase transition.

The SiV center can exist as either a neutral triplet in its ground state, neutral SiV , or as an anionic doublet state, anionic SiV^-.[32, 91–94] The latter is the most common stable ground state electronic configuration [95]. Experimentally, the ZPL measured in doped diamonds in the bulk limit is 1.31 eV and 1.68 eV for the neutral SiV and anionic SiV^-, respectively. Additionally, in SiV^- a blue-shift in the zero phonon line as a function of the decreasing crystal size has been observed for nanodiamonds.[96] For the reduced systems the ZPL splits into a four-line fine-structure at helium temperature[97, 98]. The origin of this fine structure splitting in the ground and excited states has been explained by dynamic Jahn-Teller and/or by spin-orbit effects.[91, 97, 99, 100]

Vibrational spectroscopy can also be used to probe the presence of these defects, since the changes in the dipole and the polarizability induced by the dopant can strongly modify the selection rules for the infrared and Raman active modes, respectively. In addition to UV-Vis, the K-edge X-ray absorption spectrum in diamonds has been proposed to be sensitive to the introduction of dopants.[51] Moreover, carbon K-edge spectra in nanodiamonds exhibit unidentified pre-edge features that have been either attributed to the presence of sp^2 carbon atoms lying on the surface, as a consequence of the surface reconstruction, or to the introduction of new empty levels within the band gap resulting from impurities.[51] Despite their importance, carbon K-edge X-ray and vibrational transitions for the characterization of SiV centers in nanodiamond, along with the effects of the SiV center location in the crystal lattice (i.e. surface effects, symmetry breaking) and system size (i.e. quantum confinement) on the electronic and vibrational excitations, have not been well studied. As such, the quantum confinement effects on the electronic (UV-Vis and X-ray) and vibrational (Raman) spectroscopies on several SiV-doped diamond nanoclusters is examined.

2.4.2 Silicon Vacancy Methodology

The SiV center in diamond consists of a silicon atom and a vacancy in a split-vacancy configuration.[32, 92, 101] The SiV$^-$ center was created by removing two carbon atoms near the center of the nanodiamonds along the $< 111 >$ axis of the models, and positioning the silicon at the center of the resulting divacancy in a local D_{3d} environment (namely SiV$^-$ *frozen*), as observed in previous computational studies.[91, 94, 102, 103] To evaluate the lattice distortion due to the presence of the SiV$^-$ center itself, the SiV$^-$ center and the nearest neighboring six carbon atoms were fully optimized while maintaining the rest of the diamond structure at the crystal lattice (namely SiV$^-$ *relaxed*). These optimization schemes have shown accurate results for describing the lattice distortion of nitrogen–vacancy doped diamonds of similar sizes.[31] In this work, we focus on the reduced SiV$^-$ center, whose ground state has been shown to be a doublet.[95] The ∼1.2 nm reduced SiV$^-$ $C_{119}SiH_{104}^-$ was used to estimate the excited state structural reorganization and relaxation energy. This system was further optimized according to the first bright excited state energy gradient provided by TDDFT and using the SiV- *relaxed* optimization scheme, described above. The relaxation energy in the excited state was computed as the energy difference between the vertical excitation energy using the ground-state and the excited-state optimized geometries. The ~1.2 nm diameter pure $C_{121}H_{104}$, and the reduced SiV$^-$ $C_{119}SiH_{104}^-$, were also further fully optimized in the ground state by relaxing all atoms to perform the vibrational analysis. Geometries were considered fully optimized when both the forces (maximum and RMS force, 0.450 and 0.300 mHartree/bohr, respectively) and displacement (maximum and RMS displacement, 1.80 and 1.20 mbohr, respectively) values for all free atoms were below the threshold criteria.

The ground-state electronic structures were obtained by solving the Kohn–Sham equation using the range-separated version of hybrid Becke, 3-parameter, Lee–Yang–Parr (B3LYP) density functional [6, 8, 58] with the Coulomb-attenuating approach (CAM-B3LYP).[9] The necessity of using basis sets with large spatial extent (i.e. diffuse functions) has been demonstrated to be important in nanodiamonds, since C-H bonds create low-energy empty states that are Rydberg-like, that may reduce the band gap.[104, 105] These states can play an important role for shallow implanted NV centers in diamond.[106] On the other hand, diffuse functions have been previously shown to be less important for localized defects located far from the surface.[96, 107, 108] CAM-B3LYP is known to outperform canonical hybrid (i.e. B3LYP, PBE0, etc.) for the description of Rydberg-like and charge-transfer states due to their high sensitivity to the treatment of exact exchange.[109–111] Since the presence of these Rydberg-like states can influence the predicted quantum confinement effects, CAM-B3LYP/6-31++G(d,p) was used for this study.

2.4.3 Structural Reorganization and Electronic Configurations

The models used in this work support local symmetry, but they do not preserve a global inversion symmetry operation, therefore the SiV$^-$ *frozen* conformation has an overall C_{3v} symmetry, given the asymmetry on the nanodiamond surface. Effects of the SiV$^-$ location in nanodiamonds (i.e. the position of the defect with respect to the surface) can also influence the electronic and optical properties of the systems and they are separately investigated in

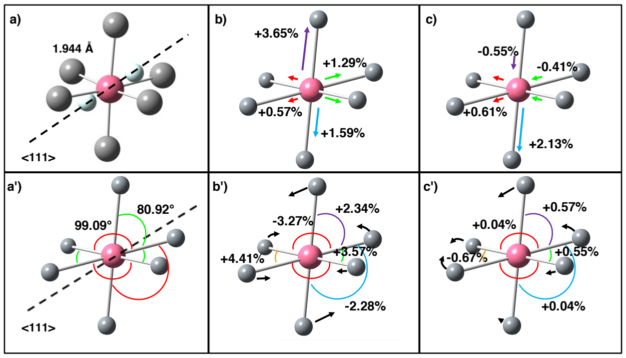

Figure 2.9: Geometry relaxation near the SiV$^-$ center for the ~1.2 nm diameter reduced SiV$^-$ $C_{119}SiH_{104}^-$ systems: carbon in gray, silicon in pink, and missing carbon atoms (vacancies) in blue (only in panel a). The SiV$^-$ *frozen* structure with the silicon located in a pseudo-local D_{3d} symmetry (panels a and a′) is represented, along with the ground (panels b and b′) and first bright excited state (panels c and c′) relaxed structures. Both the bond (top panels) and the angle (bottom panels) change in value, upon relaxation (according to the procedure detailed in the methods) with respect to the SiV$^-$ *frozen* configuration for the ground state and with respect to the ground state configuration for the excited state, are reported in percentages in panels b and c, respectively. The same color is used to highlight symmetric changes. The ground state *relaxed* geometry was also compared with the fully relaxed geometry showing a similar symmetry in the distortion.

detail in the next sections for one of the larger models. Despite this, the models can retain, in the SiV$^-$ *frozen* conformation, a local symmetric arrangement, where all Si-C distances are 1.944 Å and the C-Si-C angles are either 80.9° or 99.1°. The local symmetry of the defect may still be described as C_{3v} plus inversion, retaining a local D_{3d} symmetry (see **??**, panels a and a′).

The lattice structural reorganization in the electronic ground state in the ~1.2-nm-diameter, SiV$^-$ doped nanodiamond is summarized in Fig. 2.9 (panels b and b′). A uniform expansion of the Si pocket can be clearly seen from the elongation of all Si-C distances. Upon relaxation on the ground electronic state, the local D_{3d} symmetry is broken, although a pseudo C_s symmetry can be still observed by inspecting the Si-C distances. When the system is further allowed to relax on the first bright excited state, a non-uniform bond change is observed. Half of the Si-C distances undergo an expansion of the bond length and the other half undergo a compression (see panel c in Fig. 2.9) compared to the previously examined ground state relaxed geometry. The calculated relaxation/reorganization energy due to the optical excitation for this size is about 0.01 eV, which is much smaller than the one observed for the NV center (about 0.21 eV). This value agrees with previous calculation on Si doped diamonds[32] and explains the small contribution of the vibration sideband in the emission spectrum for these systems.[95]

Figure 2.10 shows the total and partial densities of states (PDOS) using the calculated molecular orbitals (MOs), with the spin-up and spin-down densities plotted as positive and negative values, respectively. Both the valence band (VB) and conduction band (CB) consist of carbon p and s characters, while multiple levels at the SiV$^-$ center appear inside the band gap and near the band edges. The VB and CB of the ∼2.1-nm-diameter nanodiamond are separated by an energy gap of 5.21 eV. As the system sizes decrease, the band gap increases due to stronger quantum confinement effects.

In the systems containing a SiV$^-$ center, the silicon atom contributes its four valence electrons to the SiV$^-$ center. There are also six dangling electrons from the six nearest-neighbor C atoms to the vacancies, giving rise to a total of ten electrons at the SiV$^-$ center (eleven for the reduced system). The local D$_{3d}$ symmetry splits the four sp^3 atomic orbitals of Si to a_{2u}, e_u, a_{1g}, and the six p atomic orbitals of nearby C atoms to e_g, e_u, a_{2u}, a_{1g} symmetry groups. The symmetry rules dictate that the set of orbitals of e_g symmetry has almost zero overlap with the Si atomic orbitals, resulting in a set of high energy (and mostly energetically "pinned" in the band gap) MOs with significant contributions from the carbon p orbitals surrounding the silicon (see colored PDOS in Fig. 2.10); all other atomic orbitals previously listed (e_g, e_u, a_{2u}, a_{1g}) can hybridize and form MOs surrounding the defect (depicted in Sec. 2.4.3). The resulting σ bonding and anti-bonding MOs of a_{2u} and a_{1g} symmetry are energetically buried in the VB and CB, respectively (not shown).

On the other hand, the hybridized bonding MOs of e_u symmetry are the most interesting ones because they are likely responsible for the peculiar optical properties of SiV$^-$ centers. These molecular orbitals lie at the VB edge (the antibonding ones are energetically located at the CB edge, not represented), and show a reasonable contribution from both the carbon p and silicon sp^3 orbitals. The resulting MOs show a non-zero overlap with the VB edge of the nanodiamonds, forming a set of three molecular orbitals at the VB edge. Only in the 0.8

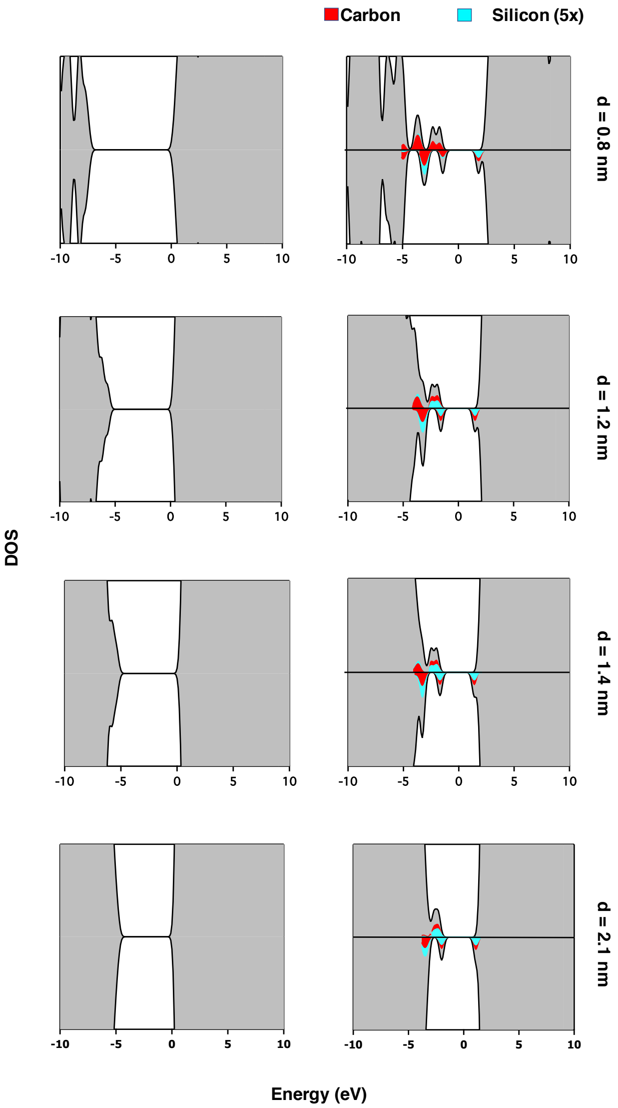

Figure 2.10: CAM-B3LYP/6-31++G(d,p) DOS and PDOS (this last visualized only for Si and its first neighboring C atoms levels within the band gap and the CB). The red and light blue colored regions show the C 2*p* and Si (magnified by 5x) 3*s* and 3*p* contributions to the PDOS diagrams, respectively. Spin-up, positive density values; spin down, negative density values. The DOS diagrams are calculated for the pure C_XH_Y, and the reduced *frozen* $C_{X-2}SiH_Y^-$ (left and right, respectively) nanodiamonds of increasing sizes (diameter $\sim$ 0.8 nm [$C_{44}H_{42}$], 1.2 nm [$C_{121}H_{104}$], 1.4 nm [$C_{182}H_{142}$], and 2.1 nm [$C_{487}H_{310}$], from top to bottom).

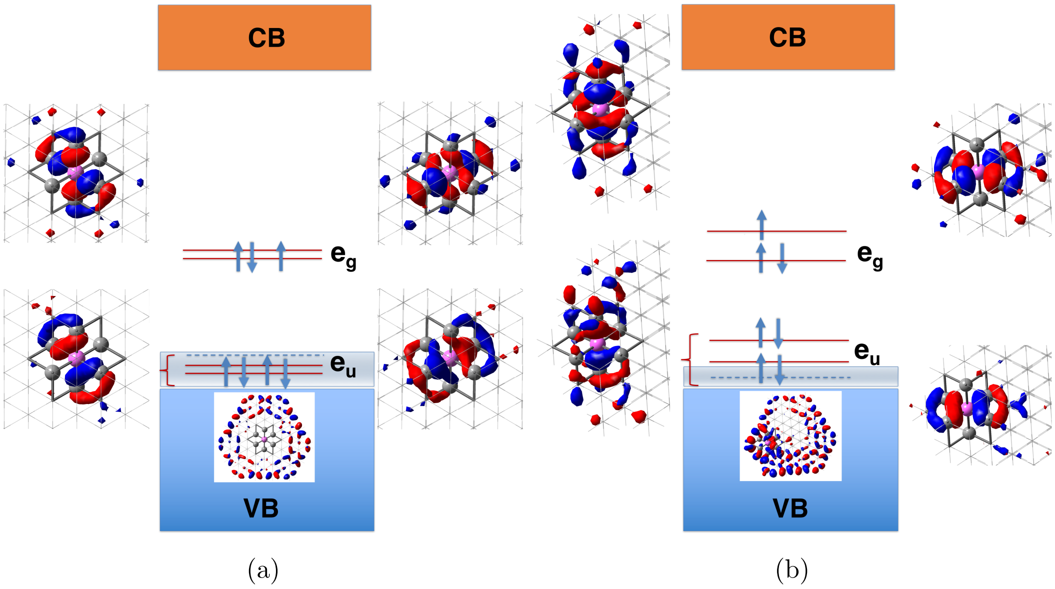

Figure 2.11: Schematic illustration of the SiV$^-$ center electronic layout, according to the D$_{3d}$ point group symmetry. Panel a, SiV$^-$ in the center of the nanodiamond, and panel b, where the SiV$^-$ defect is close to the surface and partially breaks the group symmetry (position 1 and 4 in Fig. 2.14, respectively). The zoomed in C$_{180}$SiH$^-_{142}$ CAM-B3LYP/6-31++G(d,p) beta MOs contour plots with the pseudo C$_{3v}$ axis parallel to the z-axis (entering the figure) are represented. The isodensity values of 0.05, 0.05 and 0.03 are used for the e_g, e_u and VB MOs contour plots, respectively. The energetic layout presents an uneven alignment between the alpha/beta filled e_g w.r.t. the beta e_g LUMO, please see Fig. 2.10 for a more detailed analysis. The resulting σ bonding and anti-bonding MOs of a_{2u} and a_{1g} symmetry are energetically buried in the VB and CB, respectively (not shown). From a theoretical point of view, the e_g has almost zero overlap with the Si atomic orbitals causing its higher energy layout "pinned" in the band gap. The resulting bonding MOs of e_u symmetry lie at the VB edge and are not localized only around the defects, overlapping with the VB edge orbitals in the 1.2, 1.4 and 2.1 nm nanodiamonds, forming a set of three filled molecular orbitals at the VB edge, responsible, along with the partially empty molecular orbital of e_g symmetry, of the electronic transitions in the visible range.

nm nanodiamond the MOs of e_u symmetry are energetically well separated from the VB. In this work, the negatively charged SiV$^-$ defect ground-state electronic state is ^2E_g (in a D$_{3d}$ perfect symmetry) and its electronic configuration can be described as $e_u^4 e_g^3$, where the e_g level is partially filled, in agreement with previous DFT calculations.[32, 91, 112]

2.4.4 Midgap Optical Transitions

As the size of nanodiamond decreases, the quantum confinement effect[13, 113] leads to an increase in the band-gap (5.21 eV for C_{487}, 5.78 eV for C_{182}, 6.07 eV for C_{121} and 7.77 eV for the C_{44}; reported as the HOMO/LUMO differences), as observed in other semiconducting nanocrystals.[114, 115] The previously presented electronic structures for anionic SiV^- defects in nanodiamond give rise to several characteristic sets of optical transitions exhibited in spectroscopic measurement of SiV^--containing nanodiamonds. Optical spectra for different sized SiV^--containing nanodiamonds using linear-response TDDFT are reported in Fig. 2.12. The energy levels of these SiV^- centers in the diamond lattice are illustrated in Sec. 2.4.3. This energetic layout leads to unique midgap optical transitions in SiV^--containing nanodiamonds.

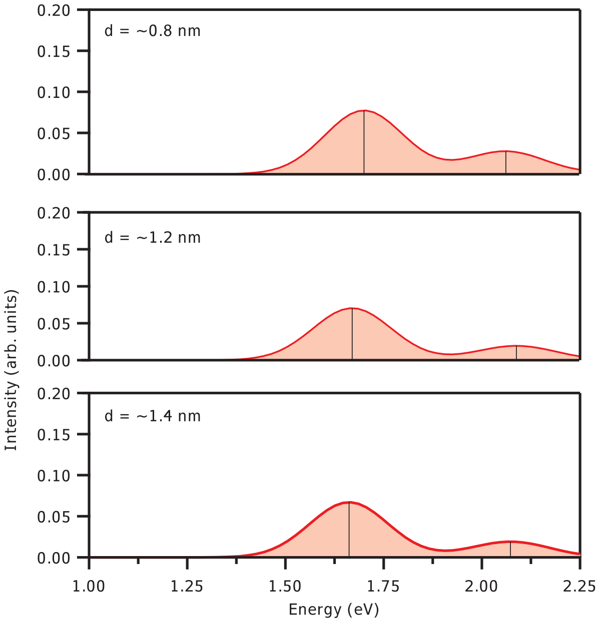

Figure 2.12: TD-CAM-B3LYP/6-31++G(d,p) UV-Vis spectra (only the two first mid-gap transitions involving the $e_u \rightarrow e_g$ beta manifold, are reported) for the relaxed anionic SiV^- $C_{X-2}SiH_Y^-$ nanodiamonds as a function of the increasing quantum dot diameter (d$\sim$ 0.8, 1.2, and 1.4 nm from top to bottom). A Gaussian broadening has been applied to the individual transitions labeled with black lines to form the spectrum with a full width half maximum value of 0.10 eV.

The optical spectra in Fig. 2.12 shows an spectroscopic feature between 1.70 and 2.10 eV consisting of two transitions, from the two filled MOs of e_u (β) symmetry to the empty e_g (β). Table 2.1 lists their vertical excitation energies in various SiV$^-$-containing nanodiamonds. These transitions give rise to the experimental zero-phonon line (ZPL) for the $^2E_g(e_u^4e_g^3) \rightarrow {}^2E_u(e_u^3e_g^4)$ excitation at 1.686 eV[95] and the main transition contributing to this feature undergoes a small blue shift with diminishing system size (from bottom to top in Fig. 2.12 and in Tab. 2.1). The partial charge-transfer characters of the ZPL in SiV$^-$ doped systems are due to the fact that MOs of e_u symmetry show a non-negligible delocalization along with a reasonable energy overlap with the VB edge (these last levels have a higher contribution arising from surface carbons, see Sec. 2.4.3), as can be seen in the computed DOS in Fig. 2.10.

Table 2.1: TD-CAM-B3LYP/6-31++G(d,p) mid-gap vertical excitation energies (e_u to e_g, beta manifold) for the anionic SiV$^-$ systems (in eV) and the corresponding oscillator strengths (reported in parenthesis). All systems present a dark state <100 meV apart from the ground state, due to the swap between the occupied and empty e_g orbitals (transitions not shown). We compare results between the SiV$^-$ *relaxed* (SiV$^-$ center position is optimized, see text) with the ones obtained from just inserting the SiV$^-$ center by replacing the corresponding atoms (SiV$^-$ *frozen*) in the center of the pure nanodiamond.

	SiV$^-$ *relaxed*	SiV$^-$ *frozen*
SiV$^-$ $C_{42}SiH_{42}^-$	1.70(0.077)	1.63(0.068)
	2.06(0.028)	1.81(0.014)
SiV$^-$ $C_{119}SiH_{104}^-$	1.67(0.070)	1.59(0.061)
	2.09(0.019)	1.82(0.014)
SiV$^-$ $C_{180}SiH_{142}^-$	1.59(0.064)	1.51(0.056)
	1.99(0.021)	1.90(0.015)

The quantum confinement effect on the spectral shift of the ZPL (ΔE_{ZPL}) as a function of the band-to-band-excitonic transition (ΔE_{EXC}) has the approximate relationship, according to the effective mass approximation for a spherical nanocrystal:[24, 115, 116]

$$\Delta E_{\mathrm{ZPL}} \approx \frac{m_e^{*-1}}{m_e^{*-1} + m_h^{*-1}} \Delta E_{\mathrm{EXC}} \tag{2.1}$$

where m_e^* and m_h^* are the effective masses (in units of electron mass) of the electron and

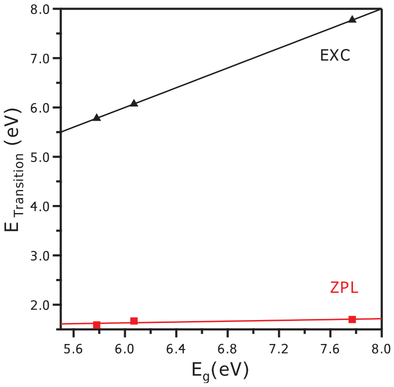

Figure 2.13: TD-CAM-B3LYP/6-31++G(d,p) SiV$^-$ ^2E_g $(e_u^4 e_g^3)$ $\rightarrow$ ^2E_u $(e_u^3 e_g^4)$ ZPL excitations, as a function of the band-to-band-excitonic transition, for the anionic SiV$^-$ systems. Extrapolation of the ZPL energies gives a value of 1.38 eV for the bulk and the ratio between ΔE_{ZPL} and ΔE_{EXC} as the slope of the linear fit is 0.04 (The reported EXC energy (band gap) is reported as a HOMO/LUMO difference, which can underestimate the experimentally observed optical band gap as it has not been computed at the TD-DFT level of theory, and also can be affected by the presence of surface defects in the experiment).

hole in the SiV$^-$-containing nanodiamond. The ^2E_g $(e_u^4 e_g^3)$ $\rightarrow$ ^2E_u $(e_u^3 e_g^4)$ excitations (as a weighted average of the first two excitations in Tab. 2.1) as a function of the band-to-band-excitonic transition for the different dot sizes is plotted in Fig. 2.13. The $\Delta E_{\text{ZPL}}/\Delta E_{\text{EXC}}$ value is 0.04, less than that in NV doped nanodiamonds,[31] and is significantly smaller than those for the free CB electron in diamond quantum dots. The observed size dependence of the ZPL is comparable with the one predicted using similar dimensions and level of theory.[96] Moreover, the quantitative analysis presented here, suggests that the photoexcited electrons in the SiV$^-$ ZPL excited states of diamonds are "heavier" than those in the pure diamond excitonic states.

2.4.5 Symmetry (or the lack thereof)

The two MOs of e_u symmetry have different spatial extent (i.e. different symmetry along the x and y directions, see Sec. 2.4.3) and subsequently different overlaps with the empty MOs of e_g symmetry, showing different relative intensities in their transitions, as can be inferred by inspecting computed oscillator strength values reported for different sized SiV$^-$-

doped nanodiamonds in Tab. 2.1. By analyzing these values for the SiV$^-$ *frozen* systems (right columns in Tab. 2.1), an average splitting of ∼0.27 eV is already noticed for the computed $^2E_g(e_u^4e_g^3) \rightarrow^2 E_u(e_u^3e_g^4)$ excitations. As mentioned before, although the SiV$^-$ *frozen* conformation has an overall C$_{3v}$ symmetry, both the asymmetry in the surface and the different spatial overlap of the filled MOs of e_u symmetry with the VB can be responsible for the energy splitting in the two $^2E_g(e_u^4e_g^3) \rightarrow^2 E_u(e_u^3e_g^4)$ transitions even in these *frozen* conformations (see the different overlap with the VB in Sec. 2.4.3). The asymmetric overlap between e_u MOs with the VB is, therefore, the key reason for both the excitonic behavior (analyzed in the previous paragraph) and the asymmetry of the absorption peak in the visible range for the SiV$^-$ doped systems. A similar interpretation has been previously provided for silicon doped nanodiamonds of similar dimensions.[96]

The effect of lattice reorganization on the $^2E_g(e_u^4e_g^3) \rightarrow {}^2E_u(e_u^3e_g^4)$ excitations as a function of the system size can be also analyzed in Tab. 2.1 (from right to left). The geometry reorganization is responsible for an additional blue shift in vertical excitation energies, from ∼0.07 (first excitation) to ∼0.25 eV (second excitation), with respect to the unrelaxed conformations. The degree of splitting of the two $^2E_g(e_u^4e_g^3) \rightarrow {}^2E_u(e_u^3e_g^4)$ excitations for the SiV$^-$ *relaxed* systems are comparable to the ones computed for the SiV$^-$ *frozen*, suggesting that the interactions of these levels with the VB band and surface are already significant to induce asymmetry in these excitations even in the SiV$^-$ *frozen* doped systems.

Since the relative position of the SiV$^-$ defect with respect to the nanodiamond surface can further perturb the overall symmetry of the system, we inspected how the location of the SiV$^-$ center within the nanodiamond can affect the SiV$^-$ ZPL transitions. As the SiV$^-$ center moves away from the C$_{3v}$ (pseudo-local D$_{3d}$ in SiV$^-$ *frozen* systems) symmetry center, its global symmetry is no longer C$_{3v}$. As a result, the set of MOs of e_u and e_g symmetry, as shown in Sec. 2.4.3, are even more energetically different due to the different interactions of the x and y subset of the e_u and e_g MOs (see their asymmetric distributions in Sec. 2.4.3) as the SiV$^-$ moves closer to the surface (e.g., positions 2-4 in Fig. 2.14). The consequence of the symmetry breaking due to the defect position on ^2E_g $(e_u^4e_g^3) \rightarrow {}^2E_u$ $(e_u^3e_g^4)$ excitations is summarized in Tab. 2.2. A splitting of $\sim$ 400 meV of SiV$^-$ midgap transitions is observed when the SiV$^-$ moves away from the C$_{3v}$ center of the nanodiamond for the SiV$^-$ *frozen*.

Table 2.2: TD-CAM-B3LYP/6-31++G(d,p) mid-gap vertical excitation energies (e_u to e_g, beta manifold) for the anionic SiV$^-$ systems (in eV)as a function of the SiV$^-$ center position moving from the center (position 1) towards the surface (position 4) for the $C_{180}SiH_{142}^-$ system. Results are compared between the SiV$^-$ *relaxed* (SiV$^-$ center position is optimized, see text) with the ones obtained by just inserting the SiV$^-$ center by replacing the corresponding atoms (SiV$^-$ *frozen*) in the center of the pure nanodiamond.

	SiV$^-$ *relaxed*	SiV$^-$ *frozen*
Position 1	1.59	1.51
	1.99	1.90
Position 2	1.66	1.67
	2.07	2.07
Position 3	1.69	1.67
	2.12	2.07
Position 4	1.67	1.60
	2.05	2.00

The magnitude of the splitting is not very sensitive to the defect position with respect to the surface, although the overall values show an overall 0.1 eV blue shift for the SiV$^-$ positions closest to the surface (larger if the systems are allowed to relax, as can be determined by looking at the values on the left in the table). This splitting of midgap transitions has been previously shown to be sensitive to the defect position relative to the surface, but its absolute value for SiV$^-$ defects appears to be larger than for the NV center.[31] Both the SiV$^-$ peak position and broadening of the emission line-width have experimentally been proved to be sensitive to either uniaxial stress or the position of the center within the matrix, in a similar way to the predicted values (∼200 meV in some observed broadening).[117–119] As the ZPL is sensitive to the surface reorganization and the size of the system, SiV$^-$ centers can be effective probes of the global and local distortions, i.e. mechanical stress or pressure.

2.4.6 Vibrational Analysis

Vibrational spectroscopy can be very sensitive to the presence of defects, since localized defects can strongly change the selection rules for infrared and Raman active modes. Presented in Fig. 2.15 is the Raman spectrum for the 1.2 nm pure (black) and reduced SiV$^-$

(blue) nanodiamond. Given the system size and the high computational cost of Raman calculations, a less expensive 6-31G(d) basis set was utilized for frequency and Raman intensity calculations. This choice is based on the observation that fully optimized geometries using 6-31++G(d,p) and 6-31G(d) bases show negligible differences, especially at the defect center. For the calculation of the vibrational response, it has been noted that, for large systems, this level of theory is sufficient,[120–123] although Raman intensity can be improved with additional diffuse function. The energy range discussed covers the region mostly affected by the presence of the SiV^{-} defects (the C-H stretching modes localized on the surface at $\sim>$ 3000 cm^{-1} are not represented). Two distinctive regions can be located by observing the Raman spectrum: the region between 1200 and 1650 cm^{-1}, involving surface H-C-H bending motions covering the typical diamond Raman band around 1300 cm^{-1} (due to the lattice C-C stretching), and the low frequency modes between $\sim$150 and $\sim$450 cm^{-1}, involving collective lattice breathing modes. The separation of these two regions has been showed to be sensitive to both the size and shape of nanodiamonds.[124]By introducing the SiV^{-} defect, an overall increase of the signal response in the region below 1100 cm^{-1} is observed. The main vibrational signatures of the presence of the SiV^{-} defect seem to be located around $\sim$910 and $\sim$156 cm^{-1}. These modes have a high contribution from the Si atom: the first are still collective stretching modes of the lattice in which C-Si are also strongly involved, while the lower energy ones are the vacancy stretching breathing modes (see Fig. 2.16 for their representations). This last spectral region seems to be the most sensitive to the isotopic substitution of the silicon atom as can be inferred by the examination of Sec. 2.4.6, where the isotopic pure Raman spectra for the most abundant isotopes of silicon is reported (^{28}Si, ^{29}Si, and ^{30}Si from top to bottom of the left panel). A progressive red shift of $\sim$1.5 cm^{-1} is observed for the peak around $\sim$156 cm^{-1} for each increase of the silicon atomic mass. In addition, the breathing mode at $\sim$442 cm $^{-1}$ (marked in red in Sec. 2.4.6 and represented in Sec. 2.4.6) strongly shows a decrease in intensity as an effect of the isotopic mass increment. Vibrational Raman responses associated with the anionic SiV^{-} and the Si substitutional defect were also compared. The substitutional defect was obtained by replacing a carbon atom close to the center of the $\sim$1.2 nm pure nanodiamond with a Si atom and optimizing the resulting structure. The SiV^{-} shows very distinct vibrational responses with respect to both the pure and the substitutional one.

Unfortunately, the spectral region presenting the typical diamond Raman peak, involving the C-C lattice stretching motions reported at ~1330 cm^{-1} for bulk diamonds[75, 125, 126], is completely washed out the by H-C-H bending motions, due to the hydrogen passivation of the surface. This problem is solved by setting the atomic mass of hydrogen to a large value (100 amu), which corresponds effectively to shift away the overlapping features from the studied spectral window.[35, 61, 124] The obtained Raman spectra using heavy hydrogen atoms (from 800 to 1600 cm^{-1}) are reported in insets of Fig. 2.15. The pure nanodiamond presents a sharp peak around ~1310 cm^{-1}, due to the C-C lattice stretching motions (see Fig. 2.16). This is the typical diamond Raman fingerprint and it is 20 cm^{-1} red shifted with respect the experimental bulk phonon band.[61, 124] The SiV^- doped spectrum shows a broadening of this peak, where several lattice stretching C-C motions involving carbon atoms around the SiV^- are now gaining intensity due to the presence of the Si, related to changes in the polarizability for these modes. These results are in agreement with the broadening observed for Raman spectra of Si doped diamonds.[127–129]

2.4.7 X-ray Absorption Spectroscopy

X-ray absorption spectroscopy (XAS) is extensively used for sample analysis, since it is a highly element specific spectroscopic technique. The K-edge feature in the XAS is due to the excitations involving 1s core electrons and the virtual valence molecular orbitals, for these reasons the structure of these peaks can provide useful information on the local order around the absorbing centers.[80, 131–133] The resulting carbon K-edge X-ray absorption spectra for the ~1.2 nm diameter pure $\text{C}_{121}\text{H}_{104}$ and the reduced SiV^- $\text{C}_{119}\text{SiH}_{104}^-$ nanodiamonds are reported in Fig. 2.18. The pure nanodiamond presents a clear absorption peak starting at 290 eV due to the well studied $1s \rightarrow \sigma^*$ transitions. As the SiV^- is introduced, several pre-edge transitions start to appear around $284 - 285$ eV. The main peak at ~290 eV for the Si doped systems is still due to several $1s \rightarrow \sigma^*$ electronic transitions, as can be inferred by inspecting the MOs responsible for them in both the pure and doped systems (see their representation in Fig. 2.18). The pre-edge peaks around 285 eV are due to the presence of the SiV$^-$ defects, arising from several carbon $1s \rightarrow e_g$ transitions (see Fig. 2.18). These analyses suggest that the pre-edge feature experimentally observed at $\sim$ 285 eV can be a signature of the presence of defects (i.e. SiV$^-$ centers). While these carbon transitions are typically ascribed to sp^2 carbon atoms lying on the surface,[35] it should be noted that these are also available to the dangling bonds surrounding carbon vacancies. However, in defects like NV and SiV$^-$, the presence of heteroatoms influences the $1s \rightarrow e_g$ carbon transition. Thus, the location of the carbon K-edge pre-edge features can be used to probe the presence of different dopants in diamonds.[51]

2.4.8 Conclusions

The mid-gap states introduced by localized defects have been shown to affect UV-Vis, X-ray and vibrational transitions in diamonds approaching the nanoscale. Using group theory and DFT electronic structure, we showed how the mid-gap states introduced by the reduced SiV center have a non-negligible overlap with the diamond VB and CB. This explains the size-dependent nature of the computed SiV$^-$ ZPL and we predict an effective excitonic mass for these transitions comparable to charge transfer excitations in NV doped nanodiamonds. We also found the ZPL to be sensitive both to the lack of symmetry in all systems analyzed and to the defect position by measuring the band position, during the defect migration towards the surface. Two diamond Raman vibrational spectral regions are predicted to be significantly modified by the SiV$^-$ center: the large-amplitude breathing (120-450 cm^{-1}) and the stretching (800-1400 cm^{-1}) motions of the lattice. Core $1s \rightarrow e_g$ (mid-gap states) transitions introduced by SiV$^-$ centers are predicted to be responsible for the occurrence of pre-edge peaks in the computed carbon K-edge X-Ray absorption spectrum for nanodiamonds, showing for the first time how this spectral region ($\sim$285 eV) can be influenced by the presence of localized defects. This work provides an important *ab initio* analysis of the electronic and vibrational structure of semi-conductors in the presence of mid-gap states due to localized defects, providing a molecular description of the spectroscopic changes in doped systems.

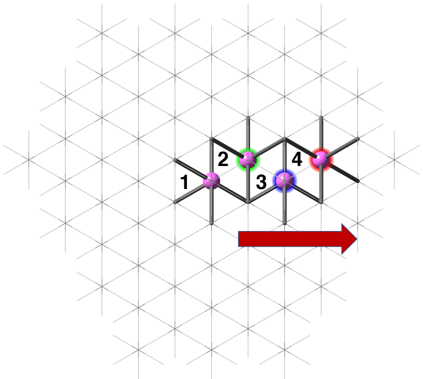

Figure 2.14: Four different SiV$^-$ positions the $C_{180}SiH_{142}^-$ system are investigated for anisotropic effects on SiV$^-$ mid-gap optical transitions

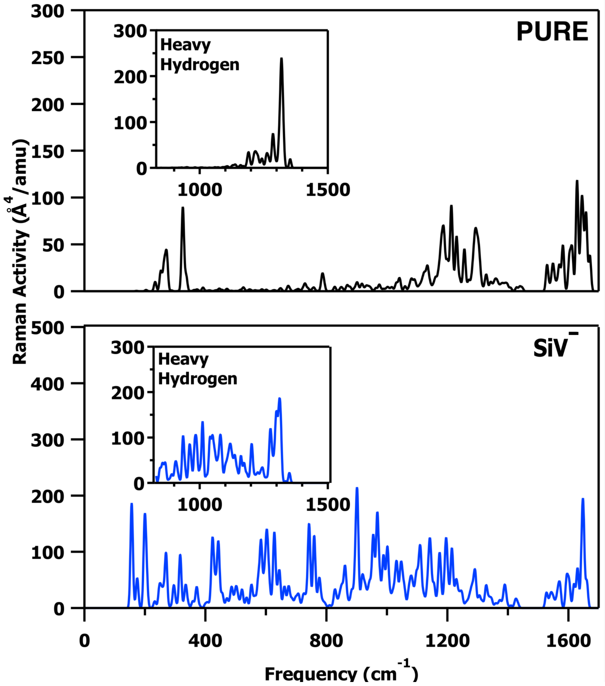

Figure 2.15: CAM-B3LYP/6-31G(d) calculated Raman spectra for the ~1.2 nm diameter pure $C_{121}H_{104}$ (black), and the reduced (isotopically averaged) SiV$^-$ $C_{119}SiH_{104}^-$ fully optimized nanodiamonds (blue). A Gaussian broadening has been applied with a full width half maximum value of 4 cm^{-1}. Insets of the spectral window originally overlapping with the H-C-H modes (from 800 to 1600 cm^{-1}) obtained using artificially heavy hydrogen atoms (100 amu) are reported for both spectra.

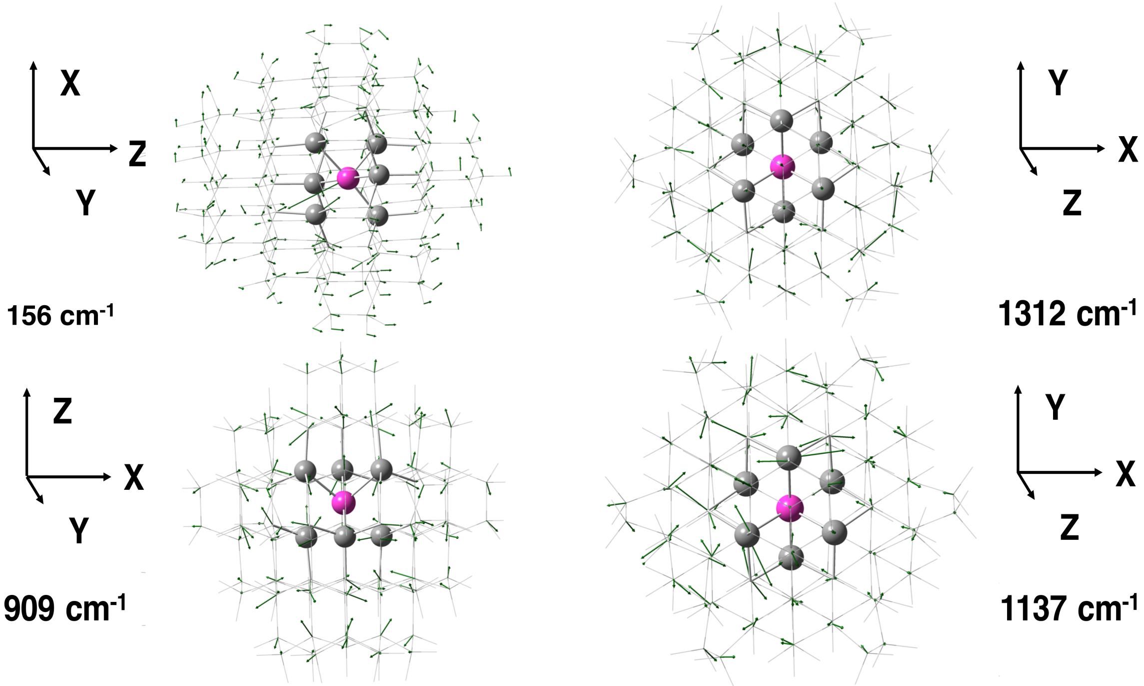

Figure 2.16: displacement vectors of the most representative normal modes for the ~1.2 nm diameter SiV$^-$ C$_{119}$SiH$_{104}^-$ doped fully optimized nanodiamond. The modes within the 909 to 1137 cm^{-1} energy range are represented using the 'heavy hydrogen' approximation for clarity, while the lowest pictured mode at 156 cm^{-1} is shown with the regularly massed system.

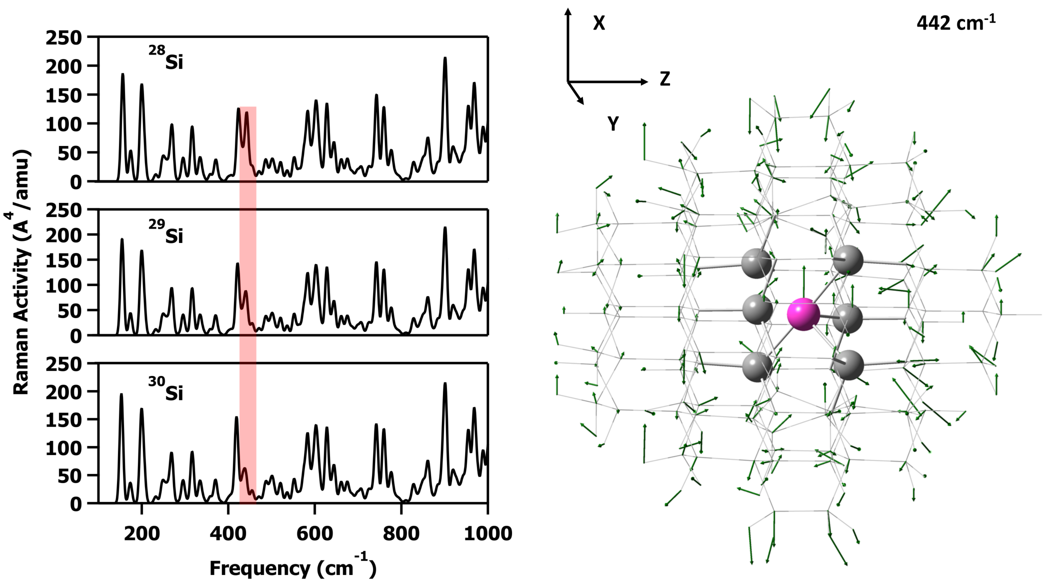

(a) (b)

Figure 2.17: (a) B3LYP/6-31G(d) isotopically pure calculated Raman spectra for the three most abundant[130] silicon isotopes ^{28}Si (92%), ^{29}Si (5%), and ^{30}Si (3%) from top to bottom of the left panel for the ~1.2 nm diameter SiV$^-$ $C_{119}SiH_{104}^-$ fully optimized nanodiamond. (b) displacement vectors of the most representative normal mode sensitive to the isotopic substitution.

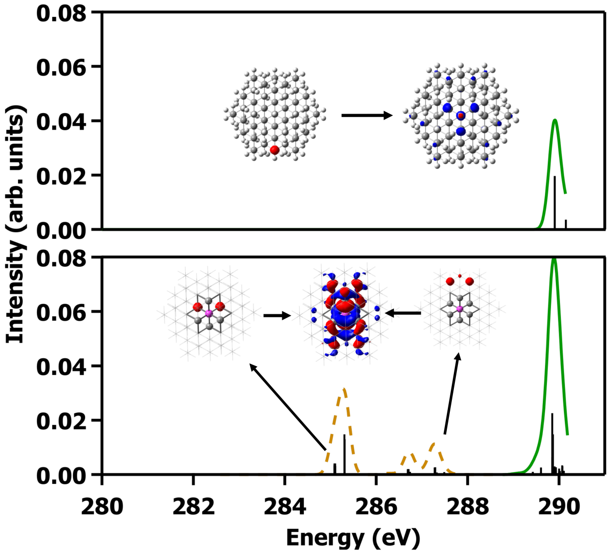

Figure 2.18: TD-CAM-B3LYP/6-31++G(d,p) calculated XAS for the ~1.2 nm diameter pure $C_{121}H_{104}$ (top, 10 states), and the reduced SiV^- $C_{119}SiH_{104}^-$ (bottom, 103 states) nanodiamonds. Carbon core $1s \rightarrow e_g$ and $1s \rightarrow \sigma^*$ transitions are grouped in orange and green, respectively. A Gaussian broadening has been applied to the individual transitions labeled with black lines to form the spectra with a full width half maximum value of 0.12 eV, and a uniform shift of 12 eV has been applied to the spectra to align theoretical results with experimental values. Contour plots of the molecular orbitals responsible for the carbon K-edge transitions, with the pseudo C_{3v} axis parallel to the z-axis (entering the figure) using an isodensity value of 0.025, are also represented.

2.5 Nitrogen Aggregate Defects

Reprinted with permission from R. A. Beck, L. Lu, A. Petrone, A. C. Ong, P. J. Pauzauskie, X. Li, *J. Phys. Chem. C.* 124, 18275-18283, **2020** copyright 2020 American Chemical Society.[36]

2.5.1 Nitrogen Aggregate Introduction

Nitrogen is a ubiquitous impurity in natural and synthetic nanodiamonds as it is difficult to fully isolate the systems from the environment. Single nitrogen-vacancy (NV) centers have been reported to have either a reduced-triplet or a neutral-doublet ground state, with the triplet state being the more stable ground-state configuration.[31, 134–137] The electronic structures, quantum confinement, and spectroscopic signatures of single NV centers have been thoroughly investigated previously,[31, 134–140] with the diamonds containing these NV centers labeled as type Ia diamonds. Depending on the structure and arrangement of the nitrogen atoms in the diamonds, as well as the conditions where the diamonds were formed, aggregate systems, known as either 'A' centers or 'B' centers, can form classifying the diamonds as type IaB.[141] These aggregate systems are classified by the number of nitrogens and vacancies contained within the defect. While significant work has gone into studying the A centers within diamonds,[142–144] less has been done for the B centers, the dominant form in type IaB diamonds.[141, 145] The form of the B center consists of 4 nitrogen atoms surrounding a single vacancy,[141] and more work is needed to identify the spectroscopic signatures of these B-center systems. The nitrogen-aggregates of central interest in this study are the N_4V (B-aggregate), and N_4V_2 (H_4-aggregate) doped systems as named in Ref. 146. They are identified theoretically through the complete neglect of differential overlap (CNDO) molecular-orbital *semi-empirical* method[147] to be the more stable of the aggregate configurations. These aggregate systems typically first exist as A aggregates (pairs of nitrogen atoms) where then, with enough time and pressure, two A centers can trap a vacancy forming the B-aggregate, the structure of which is shown in Fig. 2.19, consisting of four nitrogen atoms surrounding a vacancy. If the B-aggregate acquires an additional vacancy, and is able to undergo a slight structural rearrangement, the H_4-aggregate system is formed (Fig. 2.19).[146] The presence of these dopants can affect the selection rules for both the vibrational Raman and infrared absorption spectra, as well as introduce mid-gap states that give rise to unique UV-Visible (Vis) as well as X-ray absorption spectral features. As such, the effect of the presence of the N_4V_x-aggregates on the vibrational, UV-Vis, and X-ray spectral properties of nanodiamond systems is examined.

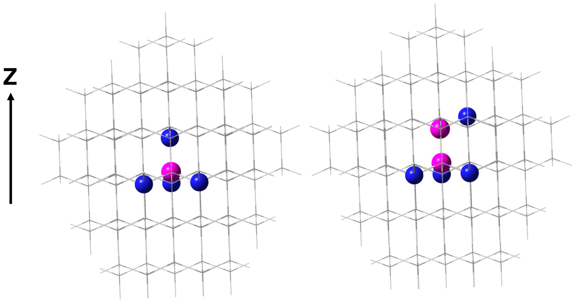

Figure 2.19: Doped 1.2 nm $C_{116}N_4H_{104}$ (as B aggregate, left) and $C_{115}N_4H_{104}$ (H_4 aggregate, right) ball and stick representation of the replaced atoms in the pure diamond matrix (this last represented as wireframe), nitrogen in blue and vacancy(s) in pink. The labeled Z axis is along the crystallographic $\langle 111 \rangle$ axis.

2.5.2 Nitrogen Aggregate Methodology

The N_4V center was created by replacing five carbon atoms near the center of the pure nanodiamond constructed from bulk parameters along the $\langle 111 \rangle$ axis of the model with four nitrogen atoms and positioning the vacancy at the center, assuming the so-called B aggregate configuration (Fig. 2.19). This defect has a local symmetry of T_d within the C_{3v} diamond host lattice. The N_4V_2 doped system was obtained by further replacing a carbon atom along the the $\langle 111 \rangle$ axis with a vacancy and replacing one of the neighboring carbons with a nitrogen resulting in a C_s symmetry. The pure diamond, B-aggregate, and H_4-aggregate systems were then independently fully optimized, and harmonic vibrational analysis was performed to verify the obtained geometries were true minima. Geometries were considered optimized when both the forces [maximum and root-mean-square (rms) of the force 0.450 and 0.300 mHartree/Bohr, respectively] and displacement [maximum and rms displacement 1.80 and 1.20 mBohr, respectively] values were below the threshold criteria. The ground-state electronic structures were obtained by solving the Kohn–Sham equation using the hybrid Becke, 3-parameter, Lee–Yang–Parr functional with the Coulomb-attenuating approach (CAM-B3LYP)[6, 8, 9, 58] with a 6-31++G(d,2p) basis. A basis set with a large spatial extent (*i.e.*, diffuse functions) has been utilized as it has been previously demonstrated to be important for describing low-energy Rydberg-like states created by C-H bonds (in this case the surface of the nanodiamonds).[104, 106]

2.5.3 Charge and Spin States

The charge and multiplicity for the B- and H_4-aggregate systems have not been well studied previously. As a result, several different possibilities for both defect structures were tested herein. A range of charges and multiplicities of the aggregate systems were examined by comparing their formation energies (Eq. (2.2)) and the difference between their highest occupied molecular orbital (HOMO) and lowest unoccupied molecular orbital (LUMO). The results are tabulated in Tab. 2.3.

Given that the defects have different numbers of electrons among the various spin states, their total energies cannot be directly compared. Thus the formation energy of a point defect in the nanodiamond was calculated using Eq. (2.2).

$$\Delta E_{\text{defect}}(q) = E_{\text{supercell}} - E_{\text{pure}} + \Sigma_i n_i \mu_i + \mu_e \tag{2.2}$$

where $E_{\text{supercell}}$ and E_{pure} are the total energies for the defect-containing and pure systems, respectively. Equation (2.2) accounts for the removal and addition of different atoms in the system (represented as the chemical potentials, felt by the chemical system, introduced by atoms removed from or added to the system, $+\mu$, or $-\mu$) as well as the difference between the charge of the systems, q, and the effect of the charge on the host crystal given by the μ_e term. Chemical potentials used for the calculation of formation energy were taken from DFT results, detailed in the Supporting Information.

The experimentally determined zero-phonon-line for bulk diamonds containing B-aggregates has been previously identified at 5.26 eV which is comparable with the neutral-singlet

Table 2.3: The LUMO-HOMO energy difference, $\Delta\epsilon$ in eV, for the examined potential electronic states (charge and multiplicity) for the H_4- and B-aggregate doped 1.2 nm nanodiamond systems optimized at the CAM-B3LYP/6-31++G(d,2p) level of theory. At this level of theory, the pure diamond has a LUMO-HOMO difference of 7.17 eV.

Charge	Multiplicity	B-aggregate		H_4-aggregate	
		$\Delta\epsilon$ (eV)	ΔE_{defect} (eV)	$\Delta\epsilon$ (eV)	ΔE_{defect} (eV)
−2	Triplet	1.11	8.34	1.05	10.82
−2	Singlet	0.81	8.71	0.77	11.90
−1	Doublet	0.87	4.79	2.56	6.95
0	Triplet	1.08	12.96	5.23	11.97
0	Singlet	5.79	3.69	5.60	7.00
1	Doublet	3.84	15.53	5.40	17.84
2	Triplet	0.04	32.61	3.68	34.74
2	Singlet	2.39	34.00	2.94	34.63

LUMO-HOMO difference of 5.79 eV,[141] suggesting that the neutral singlet is the most likely state. It is important to note that these band gaps are only examined through the difference between HOMO and LUMO, and the optical features may be of a slightly lower energy in the linear-response TDDFT framework when the electron-hole interaction is considered. In addition, this neutral, singlet state is associated with the lowest formation energy indicating that the neutral singlet B-aggregate is most likely to form.

In the case of the H_4-aggregate system, the experimentally measured photoluminescent (PL) feature for the H_4 defect is 2.50 eV.[143] There are several states (the negative doublet, neutral singlet and triplet, and the positive triplet and singlet) that have the HOMO-LUMO gap close to this energy. Through examination of the formation energies for the H_4-aggregate, the negative doublet and the neutral singlet state of the H_4 defect are most likely to form. Optical spectra computed using linear-response TDDFT show that the first excitation for the negative doublet lies at 1.33 eV and the neutral-singlet state has the first feature at 3.35 eV. As such the neutral-singlet state was chosen for further investigation, noting that the quantum confinement effect will influence the absorption spectra for these systems causing them to be higher than experiment.

2.5.4 Structures of B- and H_4-Aggregates

As shown in Fig. 2.19, the initial structure for the B-aggregate system has a local tetrahedral T_d symmetry in the C_{3v} diamond lattice. The H_4-aggregate system, however, with its additional vacancy, does not have a tetrahedral symmetry, instead it has an initial symmetry of C_s. Figure 2.20 shows the local effects of the geometry relaxation on the defects after the systems were fully optimized.

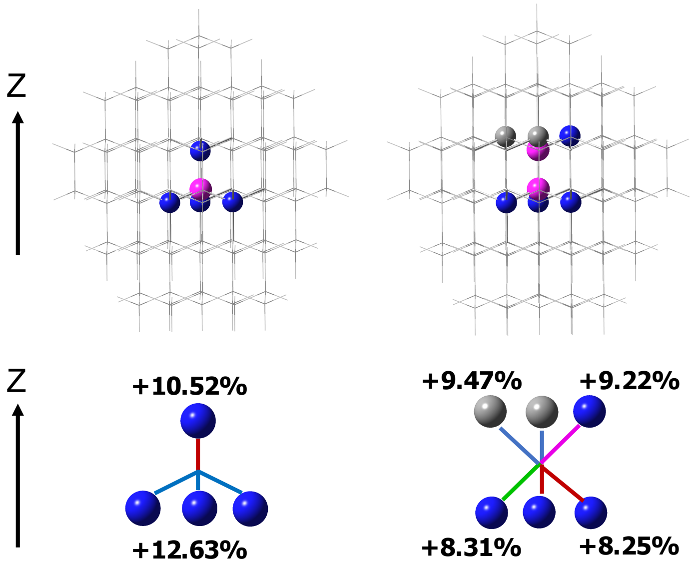

Figure 2.20: Geometry relaxation near the B- and H_4-aggregate centers ($C_{116}N_4H_{104}$ and $C_{115}N_4H_{104}$, respectively) for the 1.2 nm diameter nanodiamonds. Systems were optimized at the CAM-B3LYP/6-31++G(d,2p) level of theory. Left is the B-aggregate system with right being the H_4-aggregate system, top is the defect (nitrogen in blue, vacancies in pink) with the rest of the diamond in wireframe. Bottom shows the expansion, in percent, from the original, crystallographic bond length of 1.5446Å, with similar colors corresponding to equal expansions.

Upon optimization, the aggregate-containing systems expand out from the vacancies, compared to the initial diamond-like structures. In the case of the B-aggregate, a pseudo-tetrahedral local symmetry is mostly preserved with the NV bond length increased by 10.5%-12.6% percent compared to the crystallographic bulk diamond bond length of 1.5446 Å. The slight symmetry breaking is due to the C_{3v} symmetry of the host nanodiamond.

In the case of the H_4-aggregate system, in addition to the increased NV bond lengths, nearest carbon–vacancy bonds also increase by ∼9%. This increase in bond length has been noted before arising from the increased charge density in the vacancy given by the nitrogen atoms.[146]

2.5.5 Vibrational Analysis

Structural analysis suggests that vibrational spectroscopy can be used to differentiate between the different aggregates. While the Raman spectra are known to lack unique features that can be used to probe the nature of the nitrogen aggregate defect (see Fig. 2.21 for the pure diamond and B-aggregate Raman comparison),[145] the infrared (IR) spectra for the aggregate systems show several spectroscopic features different from both the pure nanodiamonds, and the nitrogen vacancy containing nanodiamonds.

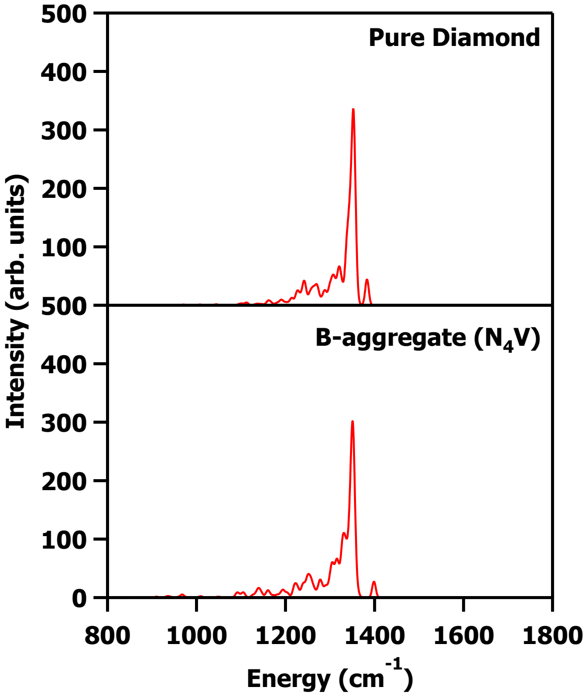

Figure 2.21: CAM-B3LYP/6-31++G(d,2p) Raman spectra for the pure ∼1.2 nm diamond (top) and the N_4V-Doped ‘B-aggregate’ diamond (bottom) with artificially heavy hydrogen mass. As can be noted the pure diamond peak at ∼1300 cm^{-1} is prominent, and there are not significant differences between the spectrum with and without the nitrogen aggregate.

Plotted in Fig. 2.22 are the calculated IR spectra for the pure diamond, nitrogen aggregates, and NV$^-$ systems. It can be noted that each species contains the diamond band at $\sim$1330 cm^{-1}.[68, 69, 148] Please see Ref. 35 for a more detailed examination of the pure diamond cluster vibrational properties. The area with the largest, most notable, differences between the aggregate and non-aggregated systems occurs in the $\sim$800 to $\sim$1200 cm^{-1} range. Given that this region has significant overlap from surface hydrogen-carbon-hydrogen bending modes, in an effort to isolate the responses due to the carbon and nitrogen vibrations, the mass of the surface hydrogen was artificially increased for analysis as has been reported in various studies examining nanodiamond vibrational spectroscopy.[34, 35, 60, 64] As can be seen in Raman spectra (Fig. 2.21), in the case of both the pure and NV$^-$-doped nanodiamonds the region of $\sim$800-1200 cm^{-1} is mostly featureless. The addition of nitrogen aggregate systems slightly increases the IR activity in this spectral region, and gives rise to one strong feature at 1116 cm^{-1} corresponding to an E vibration comprising mostly of the carbon lattice of the diamond.

Examining the IR spectra in Fig. 2.22, we identify that both of the aggregate systems contain increased responses in the $\sim$1095 cm^{-1} energy region, when compared to both the pure and NV$^-$ systems. In the case of the B-aggregate system, this vibration corresponds to an A_1 vibration primarily involving the diamond lattice around the nitrogen defect. For the H_4 defect, this is an A' vibration which involves both the diamond lattice as well as the nitrogen aggregate.

While IR spectroscopy is able to differentiate the nitrogen aggregate systems from both pure diamond and NV$^-$-doped diamonds with a fine enough resolution, the spectra for both of the aggregate systems is very similar given their similar geometries. There are two regions that show significant IR activities between the H_4- and the B-aggregate systems. At 1009 cm^{-1} which corresponds to an A_1 vibration, the B-aggregate system, compared to the H_4-aggregate, shows an increased IR activity. The 1009 cm^{-1} vibration is comprised mostly of the diamond lattice around the aggregate center similar to the $\sim$1095 cm^{-1} vibration. On the other hand, responses with an increase in activity for the H_4-aggregate system, compared to the B-aggregate, can be seen at 942 cm^{-1} and 1035 cm^{-1}. The 942 cm^{-1} vibration has A' character, and mostly involves the 'top' (as shown in Fig. 2.19) nitrogen

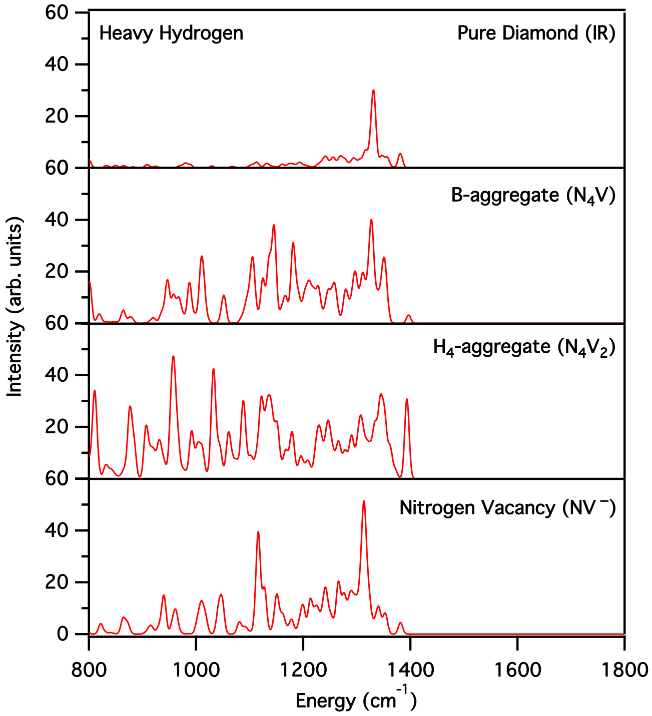

Figure 2.22: CAM-B3LYP/6-31++G(d,2p) IR spectra for, in descending order, the ~1.2 nm diameter pure diamond, B-aggregate containing diamond, the H_4-aggregate containing diamond, and the NV$^-$ diamond with artificially large hydrogen mass. IR activity has a 4 cm^{-1} broadening applied to generate the spectra for all four plots.

and vacancy within the diamond lattice. The 1035 cm^{-1} vibration has A'' character and mostly involves the 'bottom', as defined in Fig. 2.19, three nitrogens and vacancy. These features can be difficult to experimentally resolve, however recent work has been realized in aberration corrected, energy filtered low-loss electron energy loss spectroscopy enabling resolution reaching 5 meV which has allowed for the measurement of isotopically labeled bonds in molecular crystals.[149] These developments in combination with the photothermal heterodyne spectroscopic techniques may enable the experimental measurement of point defects in individual nanodiamonds.[150] As such the *ab initio* insights provided are important for distinguishing these nitrogen-containing systems. To be able to further separate the two aggregate systems the electronic structures have been investigated.

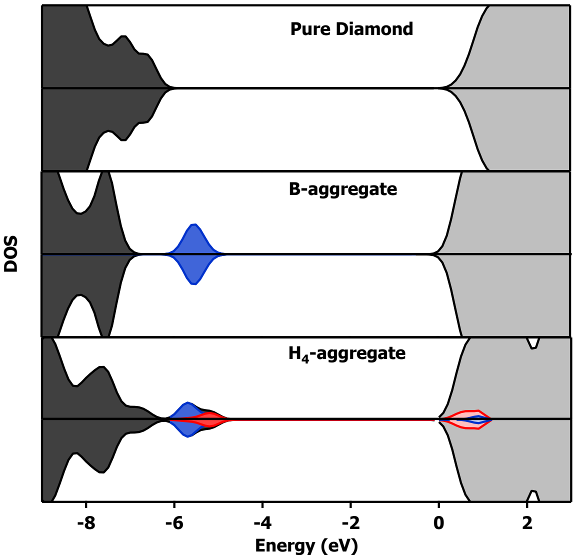

Figure 2.23: The density of states plots for the pure diamond (top), B-aggregate (middle), and H_4-aggregate (bottom) neutral, singlet systems identified earlier to be most probable. Contributions to the intraband states due to the defect are shown with nitrogen contributions in blue and, in the case of the H_4-aggregate, the carbons surrounding the 'top' vacancy in red. The partial DOS contributions by both carbon and nitrogen have been multiplied by a factor of two. The occupied orbitals are shown with a darker plot against the unoccupied orbitals.

2.5.6 Ground State Electronic Structures

The electronic density-of-states (DOS) plots in Fig. 2.23 show the presence of defect-centered intraband states when the defects are present in comparison to the pure diamond. The frontier molecular orbitals for the B- and H_4-defects are represented in Fig. 2.24, which appear as intraband states. In the case of the B-aggregate system, given that the overall symmetry of the diamond has relaxed from tetrahedral to C_{3v}, the tetrahedral t_2 orbitals are split into e and a_1 orbitals, shown in Fig. 2.24. It is interesting to note that the a_1 orbital of the B-aggregate is higher in energy than e_x and e_y orbitals unlike what is seen for the NV^- system.[31]

The presence of the H_4-aggregate causes the e_x and e_y orbitals to further split into the a' orbitals that can be seen in Fig. 2.24. These orbitals remain localized around the 'bottom' (Fig. 2.19) nitrogen atoms and vacancy with a large nitrogen contribution. The HOMO

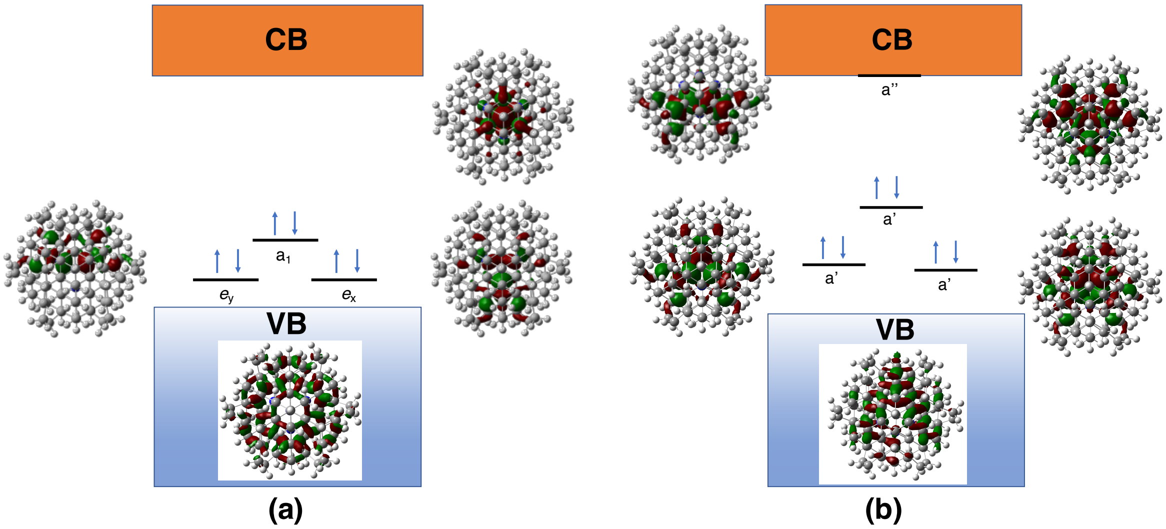

Figure 2.24: Molecular orbital diagrams for the neutral singlet, (a) B-aggregate and (b) H_4-aggregate systems. Inset pictures are plots of the MOs corresponding to the energy levels. Each surface has an isovalue of 0.03. The positioning of the MO levels is not drawn to scale.

level for the H_4-aggregate system is localized on the 'top' nitrogen and vacancy with a significant carbon contribution. Not only does the N_4-aggregate introduce the intraband occupied orbitals, it also contributes to the unoccupied levels which lie near the valence band edge. The significantly different localization schemes and symmetries of the intraband molecular orbitals localized around the B- and H_4-aggregate defects suggest that the two systems will have unique and distinct UV-Vis spectral features.

2.5.7 UV-Vis Spectra

The optical response of the nanodiamond systems in the UV-Vis region has been examined using the linear-response TDDFT formalism. Table 2.4 lists the first four excitations for both aggregate systems, and the simulated absorbance spectra can be viewed in Fig. 2.25. For the size of nanodiamond studied here, the band-to-band excitation (not shown) appears at ∼7 eV. The spectral features in Fig. 2.25 arise from transitions between defect levels to the conduction band edge of the nanodiamond. These transitions are red-shifted from

Table 2.4: CAM-B3LYP/6-31++G(d,2p) Linear-response TDDFT results for the diamond systems, the corresponding orbitals are plotted within Fig. 2.24.

Species	Absorption (eV)	Osc. Strength	Contributing Molecular Orbitals		
B-aggregate	4.47	0.0048	HOMO	→	LUMO
	4.52	0.0581	HOMO(−1)	→	LUMO
	4.52	0.0581	HOMO(−2)	→	LUMO
	4.60	0.0064	HOMO	→	LUMO(+1)
Species	**Absorption (eV)**	**Osc. Strength**	**Transition Character**		
H_4-aggregate	3.35	0.0020	a′ (HOMO)	→	a″
	3.52	0.0316	a′ (HOMO)	→	a″
	4.15	0.0010	a′ (HOMO-2)	→	a″
	4.16	0.0144	a′ (HOMO-2)	→	a″

the pure diamond band-band transitions as they originate from the orbitals introduced into the mid-gap by the aggregate as shown in Fig. 2.24. The absorption spectra of the B- and H_4-aggregates differ significantly from that of the NV^- containing nanodiamond which has features starting at ∼2 eV enabling the differentiation between aggregate systems and nitrogen vacancies.[31]

The first absorption response occurring at ∼4.5 eV for the B-aggregate is significantly red-shifted when compared to the literature absorption of ∼5.3 eV[141]. This can be attributed to the formation of Rydberg-like unoccupied states for the ∼1.2 nm nanodiamond. These states have been observed previously with hydrogen-capped ultrasmall diamond nanoparticles (adamantane, diamantane, *etc.*) as the cause of experimental bandgaps lower than anticipated, which were able to be described through TDDFT.[104] It can be seen in Fig. 2.25 and Tab. 2.4 that there are two degenerate responses with significant intensity corresponding to transitions from the e_x and e_y MOs, respectively, to the LUMO. As can be noted from the insets in Fig. 2.24, these orbitals have a larger spatial extent through the diamond than the a_1 orbital. As a result, transitions from e_x and e_y MOs are associated with a greater overlap with the conduction band orbital and thus a significantly larger intensity in the absorption spectrum.

The H_4 aggregate has several absorption features which appear red-shifted compared

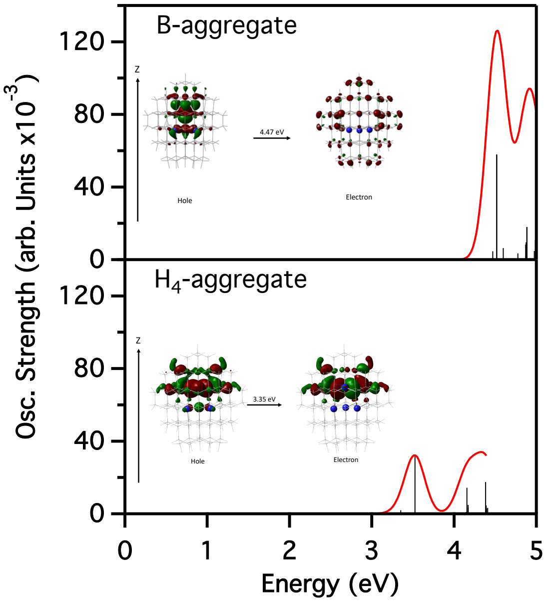

Figure 2.25: UV/Vis spectra for the B-aggregate system (top panel) and the H_4 aggregate system (bottom panel) at the LR-TDDFT CAM-B3LYP/6-31++G(d,2p) level of theory. A Gaussian broadening term has been applied to the transitions (represented as black sticks) of 0.12 eV. Inset are the are the natural transition orbitals (NTOs)[151] for the hole (left) and electron (right) orbitals for the first transition in B-aggregate and H_4-aggregate, respectively.

those in the B-aggregate, as the H_4-aggregate system introduces localized states both at the valence band edge and conduction band edge (Fig. 2.24). The lowest energy spectral peak at ∼3 eV consists of defect-centered transitions mixed with conduction band characters. This initial transition consisting of the a$'$ to a$''$ orbitals (Tab. 2.4) is significantly red-shifted when compared to the B-aggregate spectrum. Since the first transition for the H_4-aggregate center is defect-centered, the red-shift from the presence of the Rydberg states is less than for the B-aggregate.[34] While the B-aggregate excitation is largely size invariant, the spectral features of H_4-aggregate shows clear signs of quantum confinement. As previously noted,[146] and can be visualized in the inset of Fig. 2.25, the electron and hole properties of the H_4-aggregate are localized to the 'top' nitrogen and vacancy, but more delocalized compared to that of B-aggregate. As a result, UV-Vis spectral features of H_4-aggregate is more sensitive to the quantum confinement.

2.5.8 X-ray Absorption

XAS is sensitive to elemental composition of the material being probed as well as changes to the structure of the material. The XAS K-edge feature specifically examines the transition from 1s core electrons to virtual valence molecular orbitals. XAS thus can be used to study local properties of the absorbing centers. In nanodiamonds there has been previous success in characterizing heteroatomic dopants and in the study of surface reconstruction using carbon K-edge spectral features.[34, 35, 50, 80, 81, 131–133] As has been both experimentally and theoretically identified, the surface reconstruction of the nanodiamonds causes a pre-edge feature to appear in the carbon K-edge energy region of the XAS, commonly attributed to the carbon 1s to carbon π^* orbitals lying on the surface of the diamond.[33, 35, 50] In a recent work it was shown that silicon-vacancy defect was able to introduce similar pre-edge features in nanodiamonds.[34]

In this section, carbon and nitrogen K-edge XAS are examined for nanodiamonds containing different polyatomic nitrogen defect configurations. Figure 2.26 and Tab. 2.5 compare XAS carbon K-edge spectra in several different defect-containing nanodiamond. The pure diamond has one major peak appearing at ~289 eV corresponding to carbon 1s to σ^* transitions. In the case of the B-aggregate system there is a lack of a noticeable pre-edge feature. As can be determined from Fig. 2.23, the B-aggregate does not introduce unoccupied intraband orbitals. As a result, the carbon K-edge spectrum of the B-aggregate is similar to that of pure diamonds.

In contrast, unoccupied intraband levels in nanodiamonds containing H_4 and NV^- defects give rise to a noticeable pre-edge feature. This feature corresponds to transitions from the carbon 1s to the dopant-centered LUMO (a'' for the H_4-aggregate and e_x for the NV^- center). It is important to note that both of these systems have very similar energetic values for their pre-edge features. In the case of the H_4 system, the unoccupied orbitals are localized on the top nitrogen and vacancy pair and as such behaves similarly to that of the NV^- system. The pre-edge feature in H_4-aggregate and NV^- systems is ~3 eV red-shifted in comparison to the pure diamond peak. This is less than the ~5 eV shift which was previously reported in the presence of silicon split-vacancy centers or of surface reorganization

Table 2.5: The CAM-B3LYP/6-31++G(d,2p) LR-TDDFT XAS results for the carbon and nitrogen K-edge.

Species	ω (eV)*	Transition Characters
Pure nanodiamond	288.85	Carbon 1s $\rightarrow \sigma*$
	288.95	Carbon 1s $\rightarrow \sigma*$
	289.08	Carbon 1s $\rightarrow \sigma*$
	289.22	Carbon 1s $\rightarrow \sigma*$
B-aggregate	288.85	Carbon 1s $\rightarrow \sigma*$
	288.94	Carbon 1s $\rightarrow \sigma*$
	289.09	Carbon 1s $\rightarrow \sigma*$
	289.18	Carbon 1s $\rightarrow \sigma*$
	402.72	Nitrogen 1s$\rightarrow \sigma*$
	402.84	Nitrogen 1s$\rightarrow \sigma*$
H_4-aggregate	285.44	Carbon 1s $\rightarrow$ A$''$
	285.45	Carbon 1s $\rightarrow$ a$''$
	288.57	Carbon 1s $\rightarrow$ a$''$
	288.65	Carbon 1s $\rightarrow$ a$''$
	402.10	Nitrogen 1s$\rightarrow$ a$''$
	402.10	Nitrogen 1s$\rightarrow$ a$''$
	402.15	Nitrogen 1s$\rightarrow$ a$''$
NV^-	286.03	Carbon 1s $\rightarrow e_y$
	286.03	Carbon 1s $\rightarrow e_x$
	286.03	Carbon 1s $\rightarrow e_y$
	402.06	Nitrogen 1s $\rightarrow \sigma*$

*Please note values are uniformly shifted by 13 eV to better align theoretical results with experimental spectra.[34]

in nanodiamonds,[34, 35] and as such may be useful for distinguishing between the various systems.

In the case of the nitrogen K-edge, a pure diamond system will not have responses due to the absence of nitrogens in the system. As is reported in Tab. 2.5 , the nitrogen K-edge of the nitrogen-containing nanodiamonds are in the $\sim$ 402 eV range. This energetic range is similar to that for tri-valent nitrogen in non-aromatic organic molecules.[152] It can be noted that the B-aggregate is blue-shifted in comparison to the H_4-aggregate and NV^- centers as is also seen for the carbon K-edge responses. It should be noted that the response by the H_4-aggregate and NV^- center are similar since the leaving orbital for the response is the ‘top’ nitrogen which, as referenced earlier, behaves similar to an NV^- center. However, the H_4-aggregate center response is slightly blue-shifted indicating that the electron density for the center is slightly less than that of the isolated NV^- center. These responses can be beneficial for examining the nature of the nitrogen doping within the nanodiamond, and can be experimentally realized through processes such as scanning transmission X-ray absorption microscopy to compare with theoretical predictions. Additionally, to further distinguish between NV^- centers and the B-aggregate it may be possible to take advantage of polarized XAS as the NV^- centers, due to the non-centrosymmetric one-dimensional C_{3v} rotation axis, will have polarization-dependent spectra while the B-aggregate, due to the centrosymmetric T_d symmetry, will not. This can be seen by examining the electronic transition dipoles for the nitrogen K-edge transitions where in the case of the NV^- center the only strength lies along the $\langle 111 \rangle$ axis which the NV^- center is aligned with, while in the case of the B-aggregate there is dipole strength along both the $\langle 111 \rangle$ as well as the $\langle 110 \rangle$ axis. One potential issue with this is that the NV center has four potential arrangements, however work has been done previously to constrain the NV orientation during synthesis.[19]

2.5.9 Conclusions

Spectroscopic features arising from introducing nitrogen aggregates into a nanodiamond lattice were investigated. It was determined that the presence of nitrogen aggregates introduced features unique from either NV^- systems or pure nanodiamonds into their vibrational spectra. Unfortunately the infrared spectroscopic responses for both aggregate systems were very similar in the ~ 800 - ~ 1200 cm^{-1} range which sets them apart from either NV^- or pure diamond systems. It was shown that optical absorption spectroscopy can differentiate between the two investigated aggregate systems with the B-aggregate system introducing transitions at ~4.5 eV and the H_4-aggregate system introducing responses at ~3.3 eV. It was also shown that these aggregate systems affect the pre-edge region (~285 eV) of carbon’s K-edge XAS. This information can be used to differentiate further between the aggregate systems and possibly other doped diamond species. In this study, though the predicted responses in the XAS can be difficult to detect due to surface defects[35] or other dopant species[34], chemical treatments of the nanodiamond system can help reveal these features.[10, 37, 38] In addition we were able to identify vibrational and optical fingerprints of the N_4V_x-aggregate systems aiding in the future detection and characterization of these defect systems.

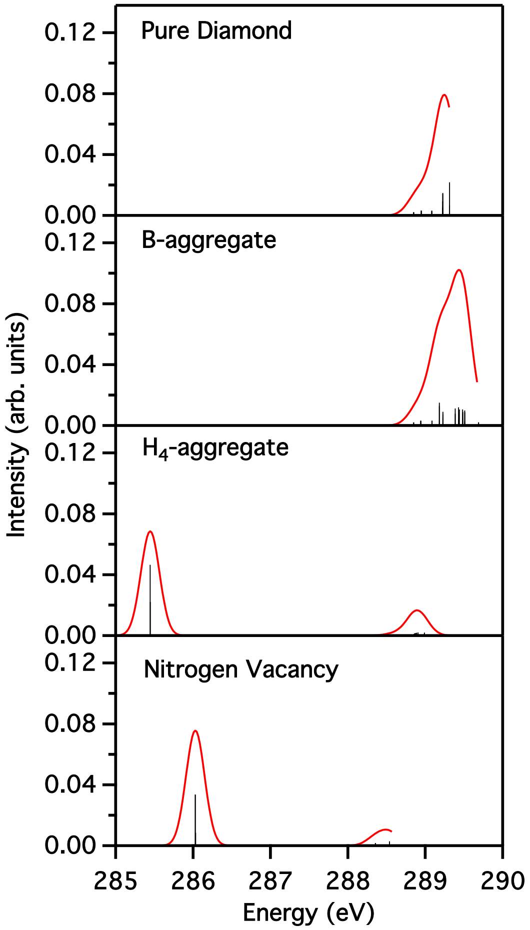

Figure 2.26: The CAM-B3LYP/6-31++G(d,2p) carbon K-edge for the ~1.2 nm diameter nanodiamond systems, uniformly shifted by 13 eV to better align with experimental values. Plotted, in descending order, are the spectra for the pure diamond, the B-aggregate system, the H_4-aggregate system, and the NV^- system. The first (shifted) excitations are listed in Tab. 2.5.

Chapter 3

SKYRMION FORMATION IN CRI$_3$ MONOLAYER

3.1 Relativity

For the above studies, the systems involved were modeled with non-relativistic methodology. Given the 'lightness' of the atoms (their low atomic numbers), and the lack of external magnetic fields the relativistic effects were deemed to not matter. The lack of relativistic effects could be seen, even for the light atoms, in the large (12 eV) energetic shifts required by the XAS results to align them with experiments to which, these effects contribute significantly. In chemistry relativity is commonly split into two regimes: scalar relativistic effects, associated with relativistic mass increase of electrons, and the spin–orbit interaction, generated by magnetic induction. Scalar effects, important for heavy elements due to high electron speed close to the nucleus, can be introduced to non-relativistic calculations with little additional cost.[153] Spin-orbit interactions, however, require at least a two-component formalism and will increase the calculation cost by at least an order of magnitude due to transition from real to complex algebra, as well as a reduction of symmetry. These interactions are required when examining, for example, X-ray spectroscopy of edges such as L or M where the leaving (absorption) or arriving (emission) orbitals have non-zero angular momentum, or when investigating materials exhibiting magnetocrystalline anisotropy.[154–158] These effects can be introduced by the Hamiltonian chosen. A common method to distinguish the different relativistic Hamiltonian choices is the dimension of the one-electron operator. As shown in Sec. 1.1 the one-electron operator ($\hat{h}(i)$, as shown in Eq. (1.7)) is a scalar operator when not in the relativistic regime. In the case of a fully-relativistic system, however, this operator is a 4×4 matrix operator due to the explicit inclusion of spin and the description of both electrons and positrons. Also available (in between the non-relativistic and four-component methods in terms of cost and accuracy) are two-component methods where the positronic degrees of freedom are frozen (as chemists are mostly concerned about electronic solutions).

In order to get to the fully-relativistic Hamiltonian, the energy of a relativistic free particle is examined:

$$\begin{aligned} E^2 &= m^2c^4 + c^2p^2 \\ E &= \pm\sqrt{m^2c^4 + c^2p^2} \end{aligned} \tag{3.1}$$

where m is the rest mass, c is the speed of light, and p is the momentum. To align Eq. (3.1) with the non-relativistic energy we can subtract or add the quantity mc^2 to or from the non-relativistic energy for the positive and negative energy bands, respectively. In order to quantize the energy expression, the relativistic energy expression is rearranged and the momentum and position operators are substituted to get:

$$(-\frac{1}{c^2}\frac{\partial^2}{\partial t^2} - p^2)\phi_1 = \left[\tfrac{i}{c}\tfrac{\partial}{\partial t} + (\sigma \cdot \hat{\mathbf{p}})\right]\left[\tfrac{i}{c}\tfrac{\partial}{\partial t} - (\sigma \cdot \hat{\mathbf{p}})\right]\phi_1 \tag{3.2}$$

Factorization is achieved using the relation $(\sigma \cdot \hat{\mathbf{p}})(\sigma \cdot \hat{\mathbf{p}}) = p^2$, where the three Pauli spin matrices are collected in the vector σ which is an instance of the Dirac identity $((\sigma \cdot \mathbf{A})(\sigma \cdot \mathbf{B}) = \mathbf{A} \cdot \mathbf{B} + i\sigma \cdot (\mathbf{A} \times \mathbf{B}))$. A second wave function ϕ_2 is introduced to obtain two coupled equations:

$$\begin{aligned} \left[\tfrac{i}{c}\tfrac{\partial}{\partial t} - (\sigma \cdot \hat{\mathbf{p}})\right]\phi_1 &= mc\phi_2 \\ \left[\tfrac{i}{c}\tfrac{\partial}{\partial t} + (\sigma \cdot \hat{\mathbf{p}})\right]\phi_2 &= mc\phi_1 \end{aligned} \tag{3.3}$$

and by taking the linear combinations:

$$\begin{aligned} \frac{i}{c}\frac{\partial}{\partial t}\left[\phi_1 + \phi_2\right] - (\sigma \cdot \hat{\mathbf{p}})\left[\phi_1 - \phi_2\right] &= mc\left[\phi_1 + \phi_2\right] \\ \frac{i}{c}\frac{\partial}{\partial t}\left[\phi_1 - \phi_2\right] - (\sigma \cdot \hat{\mathbf{p}})\left[\phi_1 + \phi_2\right] &= mc\left[\phi_1 - \phi_2\right] \end{aligned} \tag{3.4}$$

This introduces the large ($\Psi^L = \phi_1 + \phi_2$) and small ($\Psi^S = \phi_1 - \phi_2$) components of the wave function which can be cast into matrix form:

$$\begin{bmatrix} \tfrac{i}{c}\tfrac{\partial}{\partial t} & -(\sigma \cdot \hat{\mathbf{p}}) \\ (\sigma \cdot \hat{\mathbf{p}}) & -\tfrac{i}{c}\tfrac{\partial}{\partial t} \end{bmatrix}\begin{bmatrix} \Psi^L \\ \Psi^S \end{bmatrix} = mc\begin{bmatrix} \Psi^L \\ \Psi^S \end{bmatrix} \tag{3.5}$$

In order to utilize the free-particle Dirac equation, above, an external field is introduced by casting $\hat{\mathbf{p}} \rightarrow \hat{\mathbf{p}} - q\mathbf{A}$ and $E \rightarrow E - q\phi$ where a charged particle (q) and the vector potential ($\mathbf{A}$) have been introduced. Given that chemically-relevant solutions involve the electronic (positive-energy) manifold the value of q is set to $-e$ with the note that the positronic (negative-energy) solutions are related to the electronic ones through charge conjugation. To actually solve for the electronic structure the Born–Oppenheimer approximation is again applied, and the nuclear charge is limited by introducing the term for the nuclear potential ($\mathbf{V} = -e\phi_{nuc}$), where ϕ_{nuc} is the electrostatic potential of the clamped nuclei. This leaves the Dirac equation for an electron in a molecular field:

$$\begin{aligned} h_D\psi &= E^+\psi \\ &= \begin{bmatrix} V & c(\sigma \cdot \hat{\mathbf{p}}) \\ c(\sigma \cdot \hat{\mathbf{p}}) & V - 2mc^2 \end{bmatrix} \end{aligned} \tag{3.6}$$

The introduction of the minimal field corresponds to a relativistic coupling of particles and fields.[159] Non-relativistic theory is unable to properly model these interactions, such as magnetic induction which forms the basis for spin–orbit interaction. The spin–orbit mechanism originates (for the one electron) from the electrons interacting with both electric and magnetic fields due to the nucleus in relative motion.

Continuing the previous, one-electron, clamped-nuclei equations to the two-electron leads to the Coulomb term:

$$\phi(\mathbf{r}_1, t) = \int \frac{\rho(\mathbf{r}_2, t)}{\mathbf{r}_{12}} d\tau_2 \tag{3.7}$$

Where the complexity of the relativistic two-electron interaction appears in the accompanying vector potential:

$$\mathbf{A}(\mathbf{r}_1, t) = \frac{4\pi}{c^2} \int \frac{\mathbf{j}_\perp(\mathbf{r}_2, t_r)}{\mathbf{r}_{12}} d\tau_2 \tag{3.8}$$

where $t_r = t - \frac{\mathbf{r}_{12}}{c}$ and $\mathbf{j}_\perp$ is the current density. Through this the time is no longer instantaneous which reflects the finite speed for interactions in a relativistic domain. The first-order correction to the two-electron interaction can be obtained by starting with the approximation:[160]

$$\begin{aligned} E_{int} &= q_1\phi_2 - q_1 v_1 \cdot \mathbf{A}_2 \\ &\sim \frac{q_1 q_2}{r_{12}} - \frac{q_1 v_1 \cdot q_2 v_2}{2c^2 r_{12}^3} \end{aligned} \tag{3.9}$$

where the first term is the Coulomb term, and the second two terms involve the vector potential of the second electron. When quantized it becomes the Breit term:

$$g^B(1,2) = -\frac{ec\alpha_1 \cdot ec\alpha_2}{c^2 r_{12}} - \frac{(ec\alpha_1 \cdot \nabla_1)(ec\alpha_2 \cdot \nabla_2)\mathbf{r}_{12}}{2c^2} \tag{3.10}$$

of which the first term is known as the Gaunt term.[161] The Coulomb terms includes charge-charge interactions and the Gaunt term includes current-current interactions, both terms give rise to spin–orbit interaction. The Coulomb term gives rise to spin–same-orbital (SSO) as does the one-electron nuclear-electron interaction, with the Gaunt term being responsible for spin–other-orbit (SOO) interactions.

Before giving the form of the relativistic Hamiltonian, the coupling between the large and small components must be addressed. The exact coupling, as determined from Eq. (3.6), can be written as:

$$\Psi^S = R\Psi^L \tag{3.11}$$

where R is given by:

$$\begin{aligned} R(E) &= P2mc^2 - V + E^+)^{-1} c(\sigma \cdot \hat{\mathbf{p}}) \\ &= \frac{1}{2mc}\left[1 + \tfrac{E^+ - V}{2mc^2}\right]^{-1} (\sigma \cdot \hat{\mathbf{p}}) \end{aligned} \tag{3.12}$$

where due to the factor $\left[1 + \frac{E^+ - V}{2mc^2}\right]$ the Ψ^S terms are on average a factor c smaller than the large components for the electronic solutions. Given the cost (due to the dependence on the energy in Eq. (3.12)) the non-relativistic limit is commonly substituted:

$$\lim_{c\to\infty} c\Psi^S = \frac{1}{2m}(\sigma \cdot \hat{\mathbf{p}})\Psi^L \tag{3.13}$$

however this form is only valid if $|E^+ - V| << 2mc^2$. Imposing the kinetic balance, and thus transforming into the large (Ψ^L) and the pseudo-large (Φ^L) components by:

$$\begin{bmatrix} \Psi^L \\ \Psi^s \end{bmatrix} = \begin{bmatrix} I_2 & 0_2 \\ 0_2 & \frac{1}{2mc}(\sigma \cdot \hat{\mathbf{p}}) \end{bmatrix} \begin{bmatrix} \Psi^L \\ \Phi^L \end{bmatrix} \tag{3.14}$$

and thus to the modified Dirac equation:

$$\begin{bmatrix} V & T \\ T & W_0 - T \end{bmatrix} \begin{bmatrix} \Psi^L \\ \Psi^s \end{bmatrix} = \begin{bmatrix} I_2 & 0_2 \\ 0_2 & \frac{1}{2mc^2}T \end{bmatrix} \begin{bmatrix} V & T \\ T & W_0 - T \end{bmatrix} \tag{3.15}$$

with $T = \frac{\hat{\mathbf{p}}^2}{2m}$ and $W_0 = \frac{1}{4m^2c^2(\sigma \cdot \hat{\mathbf{p}})V(\sigma \cdot \hat{\mathbf{p}})}$. One important note is that the bound orbitals are not selected to be those with the lowest energy (due to the presence of the negative-energy manifold), rather they are the ones starting from the orbitals of lowest positive-energy orbitals, identified through the gap of $2mc^2$. [153]

3.2 Skyrmion Introduction

The work in this section is adapted with permission from R. A. Beck, L. Lu, P. V. Sushko, X. Xu, and X. Li, *JACS Au.* **Article ASAP. 2021** copyright 2021 American Chemical Society.[162]

Magnetic skyrmions are local whirls of the spins that both have a fixed chirality and do a full spin rotation.[163, 164] Isolated skyrmions can be treated as single particles and used in applications, such as system memory, radio frequency generators and filters, as well as spintronic devices.[163, 165–167] Magnetic skyrmions have been found to manifest in both single-crystals of magnetic materials (such as MnSi, FeGe, $Fe_{1-x}Co_xSi$, and Cu_2OSeO_3) as well as in thin films such as Fe monolayers and PdFe bilayers on Ir.[163, 166] In order for a skyrmion to be usable for memory or spintronic applications, however, they need to be realizable at, or close to, room temperature and with minimal electromagnetic fields.

Skyrmions form in crystals that lack inversion symmetry in the crystal lattice enabling the formation of Dzyaloshinskii–Moriya interactions (DMIs) through spin–orbit coupling, or in the case of thin films at the interface between the layer and the substrate facilitated through the strong spin–orbit coupling of the nearby metal center.[163, 166] This DMI takes the form:[168]

$$H_{DMI} = (S_1 \times S_2) \cdot \mathbf{D_{12}} \tag{3.16}$$

where S_1 and S_2 are spins of two neighboring magnetic atoms and $\mathbf{D_{12}}$ is the corresponding Dzyaloshinskii–Moriya vector. If the exchange interaction between S_1 and S_2 is mediated by an anion, $\mathbf{D_{12}}$ can be approximated as $\mathbf{D_{12}} = \mathbf{r_1} \times \mathbf{r_2}$, where $\mathbf{r_1}$ and $\mathbf{r_2}$ link the anion with the two magnetic ions.[155] In materials containing inversion symmetry, this term is missing as the contributions associated with anionic pathways linking magnetic centers cancel out.

Chromium trihalides and, more broadly, MX_3 (where M is a transition metal) compounds are actively investigated for their unusual properties. They have a low synthesis and processing cost and can be easily exfoliated to obtain few-layer materials. In chromium trihalide (CrX_3, X=Cl, Br, I) structures, the Cr^{3+} ions are arranged into honeycomb lattices surrounded by six halogen anions giving rise to local octahedral symmetry. The halogen atoms are each bound to two neighboring Cr centers. At high temperature the layers stack with a monoclinic (space group $C2/m$) geometry. At low temperature the layers stack with a rhombohedral (space group $R\overline{3}$) geometry. The temperature at which this transformation occurs is dependent on the halogen (Cl = 240 K, Br = 420 K, and I = 210 K), and each bulk structure is known to have ferromagnetic moments between each Cr ion below their T_c (Cl = 17 K, Br = 37 K, and I = 68 K).[169, 170] Examples of the monolayer, hexagonal lattice can be seen in the insets to Fig. 3.1.

It has been shown that in the low-layer limit (number of layers $\lessapprox$10), MX_3 exhibits magnetic properties which appear to differ from their bulk properties.[171–174] Recently, mono- and bi-layers of chromium trihalide materials have been investigated for potential use in skyrmionic devices.[163, 165, 175, 176] Of the chromium trihalides, chromium triiodide (CrI_3) materials have been of the most interest as CrI_3 bulk has been shown to exhibit the highest reported magnetic ordering temperature and anisotropy among the chromium trihalides.[169, 171, 177–179]

Monolayer CrI_3, in disagreement with the Mermin–Wagner theorem, is known to have long-range ferromagnetic character[165, 180] which is enabled through the magnetic anisotropy.[158, 165] This magnetic anisotropy in CrI_3 arises from the spin–orbit coupling in iodine atoms, and favors a magnetic easy axis perpendicular to the atomic plane.[155, 158, 170] Magnetic interactions between the chromium ions in a CrI_3 layer arise from a superexchange mechanism between the Cr $3d$ orbitals and the I $5p$ orbitals.[155, 158, 174, 181] Geometric distortions in the CrI_3 layers can break the inversion symmetry, and thus induce finite Dzyaloshinskii–Moriya interactions, ultimately leading to the appearance of skyrmionic ground states. In the case of an applied electric field oriented perpendicular to the CrI_3 plane, the Cr^{3+} and I^- ions displace in the opposite directions out of their atomic planes. These displacements change distances between the chromium and iodine atomic planes by as much as $\sim$3.6% for a field with a magnitude of $\sim$0.2 V/nm which breaks the inversion symmetry and results in significant DMI effects. It has also been reported that Janus $Cr(I,X)_3$ monolayers have been able to realize ground-state skyrmions given the ability to manifest DMI terms due to their lack of inversion symmetry.[156, 163, 165, 176, 182, 183]

In this work we investigate the formation of skyrmionic states via breaking the inversion symmetry of the CrI_3 monolayer by substituting iodine atoms with chloride atoms (Cl_x). Unlike external electric fields, these defects produce localized atomic-scale distortions, which holds the promise of creating fine-tuned distortion patterns and, accordingly, may enable the formation of complex magnetic structures.

3.3 Methodology

Monolayer CrI_3 was represented using the isolated periodic slab model. The initial positions of atoms correspond to the bulk CrI_3 lattice as determined through single crystal X-ray diffraction at 90 K.[169] To find the optimal structure of the monolayer and its electronic properties, we performed *ab initio* simulations based on the density functional theory (DFT) as implemented in the Vienna *ab initio* simulation program (VASP).[184, 185] The projector augmented wave method and Perdew–Burk–Ernzerhof exchange-correlation functional were used.[7, 186] The calculations were performed in the spin-polarized mode. A plain-wave basis set was used with an energy cutoff of 600 eV, and the DFT-D3(0)[187] method was used for dispersion correction. All internal coordinates were fully relaxed. It has been noted that the Hubbard U correction applied within the DFT+U method does not significantly impact

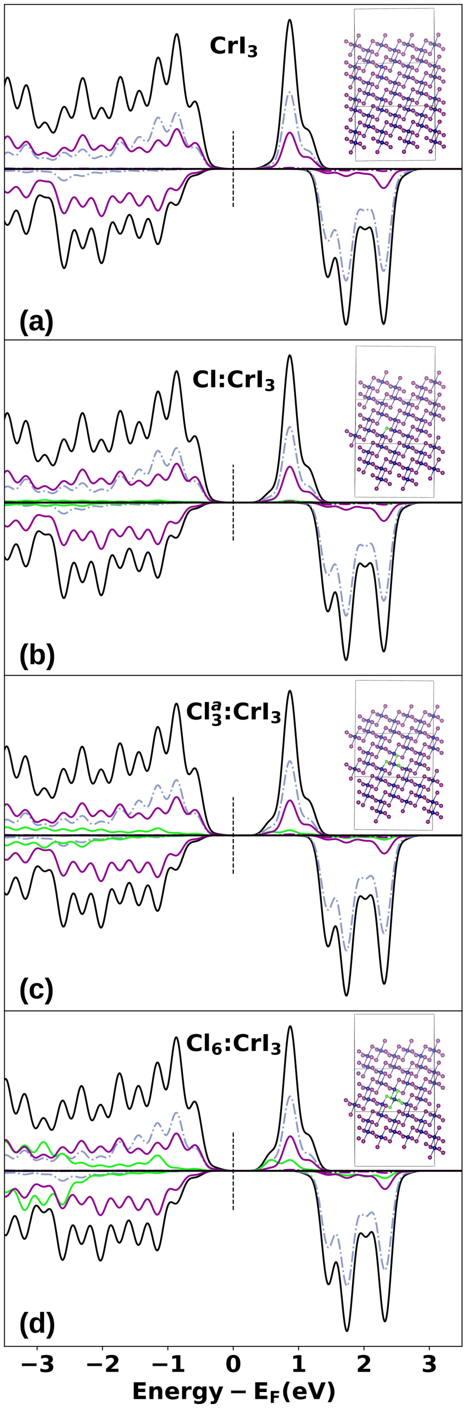

Figure 3.1: The spin-resolved projected density of states for the monolayer CrI_3 systems (shown as insets to each plot). The total DOS can be seen in each plot as the black line, the projected orbital contributions for the Cr-d (blue) and I-p (purple), and Cl-p (green) atoms are plotted as well. The pure CrI_3 monolayer is shown at the top (a), with the halogen-replaced structures shown beneath: $Cl:CrI_3$ (b), $Cl_3^a:CrI_3$ (c), and $Cl_6:CrI_3$ (d).

the results of the calculations, and as such is not used herein.[155, 158]

To find the properties of pristine CrI_3, we used a supercell containing two chromium and six iodine atoms. A 3.5 nm vacuum gap in the off-plane direction (z) was used to avoid the monolayer interactions with its periodic images. The Brillouin zone was sampled with a Monkhorst-Pack k-point mesh of $6 \times 6 \times 2$. The optimal lattice constant (a_0) was found to be 6.929 Å, which is in a close agreement with the experimentally observed value of 6.866 Å.[169]

The calculated Heisenberg isotropic symmetric exchange coefficient ($J = -2.99$ meV) and the magnetic anisotropy energy (MAE) (0.58 meV/Cr) are comparable with those previously reported for the CrI_3 systems (less than 10 layers): $J = -2.2$ meV and MAE = 0.65 meV/Cr.[155, 165, 188]

In order to examine the magnetic effects of Cl substitution, we used a CrI_3 supercell of 1.8 nm × 3.1 nm × 2.0 nm. Several I atoms near a chromium center were replaced with Cl atoms, and the internal coordinates were optimized for each case. The cutoff for energy minimization with respect to the atomic coordinates was set to 10^{-5} eV. With the optimized structure, a noncollinear (NC) spin calculation was run with the self-consistent-field (SCF) convergence cutoff set to 10^{-6} eV. The noncollinear wavefunction was used as a guess for the calculations incorporating spin–orbit coupling effects (NC-SOC) with SCF convergence set to 10^{-9} eV in order to capture the energy cost of spin rotations which typically are on the order of $10^{-6} \sim 10^{-4}$ eV in magnitude.[165]

3.4 Results and Discussion

3.4.1 Geometric Distortion

To investigate the coupling between the lattice distortions in CrI_3 and its magnetic properties, we considered several configurations of Cl substituted for I. Chlorine was specifically chosen as it has been previously shown that bulk $CrCl_3$ exhibits an in-plane ferromagnetism,[169] which was thought could be taken advantage of to promote skyrmion formation without drastically altering the properties of the CrI_3 layer. Also, of the CrX_3 systems commonly examined, Cl has the smallest atomic radius (*i.e.*, the largest mismatch with that of I), and

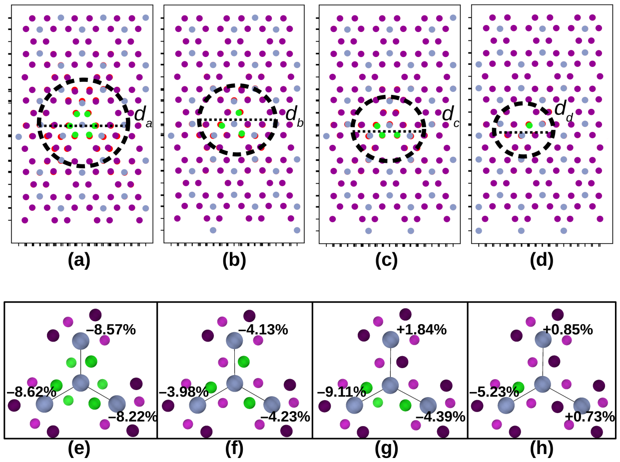

Figure 3.2: The optimized geometries of the Cl_x:CrI_3 systems. The initial position of the relevant atoms can be visualized by the red circles. The final geometries are shown with the gray circles representing Cr atoms, the purple circles representing iodine, and the green circles representing chlorine after optimization. The geometries consist of Cl_6:CrI_3 (**a**), Cl_3^a:CrI_3 (**b**), $Cl_2^aCl^b$:CrI_3 (**c**), and Cl:CrI_3 (**d**). **e-h** show the four central Cr atoms and bound halogen atoms. The text shows the difference in the bond length between the central Cr atom and those neighboring from the pure CrI_3 system and the optimized, doped systems (shown as a ±% of the original Cr-Cr bond length).

as such is thought to give rise to the largest geometric distortions. Four Cl_x:CrI_3 structures were examined, and can be viewed in the insets for Fig. 3.1. The four configurations considered have six iodine atoms replaced around a chromium center (Cl_6:CrI_3), three Cl replacing the iodine above the chromium atomic plane (Cl_3^a:CrI_3), three Cl replacing two iodine above and one iodine below the chromium atomic plane ($Cl_2^aCl^b$:CrI_3), and one Cl replacing a single iodine atom (Cl:CrI_3).

As can be seen in Fig. 3.2, replacing I atoms with Cl atoms results in a contraction of the Cr-Cl bonds (in comparison to the Cr-I bonds) as is expected given that Cl is both smaller and more electronegative than I. In the case where six I atoms are replaced, the geometric distortions extend through the monolayer for ∼1.7 nm, similar to the extent of skyrmion formation which has been observed when CrI layers are exposed to a field.[165] It should be noted that this size may be artificially constrained due to the size of the cluster used, as was also noted for the skyrmion formation by Liu *et al.* (Ref. 165). This distortion is shown in

Fig. 3.2a as the circle of diameter $d_a = 1.7$ nm. For systems where less Cl has been doped into the cell (in Fig. 3.2b-d) the extent of the distortion caused is lessened. Cl_3^a:CrI_3 shows an extent of $d_b = 1.2$ nm, and $\mathrm{Cl}_2^a\mathrm{Cl}^b$:$\mathrm{CrI}_3$ and Cl:CrI_3 (d_c and d_d, respectively) show an extent of 1.0 nm.

The effects of the larger spatial extent of the distortion mean that there are additional chromium centers that no longer have the full octahedral symmetry surrounding them. In an octahedral crystal field, Cr(III) d orbitals split into t_{2g} and e_g manifolds. The three-fold degenerate t_{2g} levels are singly occupied by three d electrons. This configuration corresponds to a high-spin $^4\mathrm{A}_2$ ground state at each Cr site with the excited $^4\mathrm{T}_2$ state being 1.5 eV above. Upon doping Cl in CrI_3, the structure around Cr(III) deviates from the perfect octahedral environment. However, the perturbation is not strong enough to alter the ligand field, and each Cr(III) center still retains the high-spin configuration. The loss of octahedral symmetry gives rise to DMI terms potentially leading to noncollinear spin solutions with no applied field. It is of particular interest that both the Cl_6:CrI_3 and Cl_3^a:CrI_3 systems have a symmetric distortion around the central Cr and thus the final geometries are similar, while the $\mathrm{Cl}_2^a\mathrm{Cl}^b$:$\mathrm{CrI}_3$ and Cl:CrI_3 systems are less symmetric about the central Cr. In the case of the $\mathrm{Cl}_2^a\mathrm{Cl}^b$:$\mathrm{CrI}_3$ and Cl:CrI_3 systems the central Cr is pulled slightly towards the Cr centers that are mediated by Cl atoms leading to a significant distortion to the angles and bond lengths of the surrounding systems.

The formation energy of each isovalent-doped Cl_x:CrI_3 configuration can be estimated by:

$$\Delta E = E(\mathrm{Cl}_x{:}\mathrm{CrI}_3) - E(\mathrm{CrI}_3) + n(\mu_\mathrm{I} - \mu_\mathrm{Cl}) \tag{3.17}$$

where $E(\mathrm{Cl}_x{:}\mathrm{CrI}_3)$ is the energy of the Cl_x:CrI_3 system, $E(\mathrm{CrI}_3)$ is the energy of the CrI_3 lattice without dopants, and n is the number of substituted ions. The chemical potential, μ, for the iodine and chloride atom are computed as $\frac{1}{2}E(\mathrm{I}_2)$ and $\frac{1}{2}E(\mathrm{Cl}_2)$, respectively. The formation energies tabulated in Tab. 3.1 show that the geometries most likely to appear are the singly-doped Cl_1:CrI_3 and the symmetric Cl_6:CrI_3.

As a result of the geometric distortions, the inversion symmetry for the doped systems (except the Cl_6:CrI_3 system) is broken. Thus the DMI terms become non-zero. The DMI

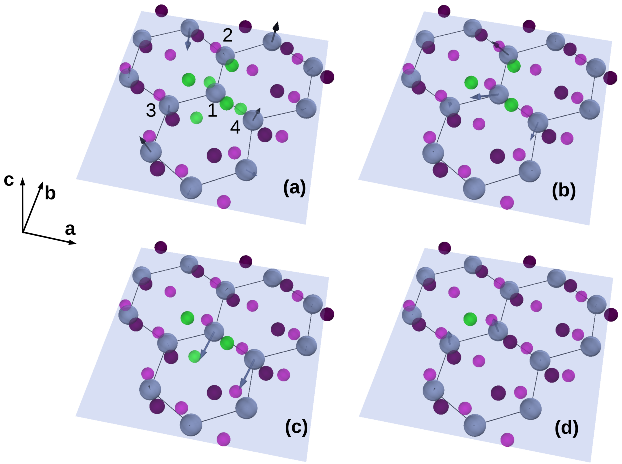

Figure 3.3: The DMI vectors (in black, determined as by in Ref. 157) on each Cr atom from the geometry optimized, Cl doped systems shown in Fig. 3.2, Cl_6:CrI_3 (a), Cl_3^a:CrI_3 (b), $Cl_2^aCl^b$:CrI_3 (c), and Cl:CrI_3 (d). Since the DMI vectors are only non-zero where the inversion symmetry is broken, and the symmetry breaking is a localized effect, only the atoms that lie roughly within the black circle in Fig. 3.2 have been plotted. The labeled atoms in (a) are the Cr atoms used in the four-state method to calculate the DMI vectors that are reported in Tab. 3.2.

vectors for the Cr atoms within the distorted areas marked in Fig. 3.2 are plotted in Fig. 3.3. This effect is localized to the areas with geometric distortion. This can be seen in Fig. 3.3(d), where the spatial extent of the geometry distortion is significantly less than in the other systems, by the fact that the Cr atoms on the far right (where there was little to no distortion) do not have applicable DMI vectors. As previously mentioned, the Cl_6:CrI_3 system is able to maintain inversion symmetry around the central atom, and as such the

Table 3.1: The formation energies, as determined by Eq. (3.17) for the four doped geometries.

System	Formation Energy (eV)
Cl_6:CrI_3	-3.96
Cl_3^a:CrI_3	28.06
$Cl_2^aCl^b$:CrI_3	27.99
Cl:CrI_3	-0.69

Table 3.2: DMI vectors calculated using the four-state method of Refs. 158, 176.For the Cl_6:CrI_3 and Cl_3^a:CrI_3, the three-fold symmetry surrounding the Cr center is maintained so only one vector is shown. For the other systems, this symmetry is broken and the DMI vectors between the central Cr and the three surrounding Cr centers are shown. Cr centers are identified in Fig. 3.3.

System	Pair	$\mathbf{D}_{ij}^X$ (meV)	$\mathbf{D}_{ij}^Y$ (meV)	$\mathbf{D}_{ij}^Z$ (meV)	J_{ij} (meV)	$\lvert\mathbf{D}_{ij}\rvert/J_{ij}$ (meV)
Cl_6:CrI_3	Cr_1-Cr_2	-0.28	0.34	-0.22	-0.07	7.24
Cl_3^a:CrI_3	Cr_1-Cr_2	-0.90	0.79	-1.47	-0.86	2.20
$Cl_2^aCl^b$:CrI_3	Cr_1-Cr_2	0.22	0.72	1.02	-1.38	0.92
$Cl_2^aCl^b$:CrI_3	Cr_1-Cr_3	0.22	1.81	0.21	-1.24	1.48
$Cl_2^aCl^b$:CrI_3	Cr_1-Cr_4	0.26	-0.02	-0.77	-0.08	10.16
Cl:CrI_3	Cr_1-Cr_2	-0.38	-0.16	1.15	-0.89	1.37
Cl:CrI_3	Cr_1-Cr_3	0.22	-0.09	-0.56	-0.68	0.89
Cl:CrI_3	Cr_1-Cr_4	-0.13	-0.52	0.07	-1.16	0.47

DMI contributions along each halide pathway cancel out, which is not the case for the other systems.

3.4.2 Formation of Spin Bubble

Magnetic skyrmions are local whirls of the spins that both have a fixed chirality and do a full spin rotation.[163, 164, 167] Unfortunately none of the geometries attempted in this study are able to realize a full symmetric skyrmion at zero field. Instead, spin bubbles, localized spin-canted electronic configurations that are driven by DMI terms, can be observed in the CrI_3 monolayers arising from spin noncollinear solutions. In the case of the Cl:CrI_3 system a spin bubble solution was stabilized as can be seen in Fig. 3.4. Plotted in Fig. 3.4 are the atomic clusters shown in Fig. 3.3 with the magnetization vectors for each Cr atom plotted. It can be noted that in the case of the Cl_3^a:CrI_3 and $Cl_2^aCl^b$:CrI_3 systems, the spin bubble is unable to manifest and the ferromagnetic solution persists.

In the case of the Cl:CrI_3 system, the stabilization by the formation of the spin bubble over the ferromagnetic solution is 25.7 meV/Cr. This energetic difference is larger than what has been previously observed as the stabilization energy from the formation of skyrmions through the use of external fields (∼3 meV/Cr) is much larger than the cost of a spin

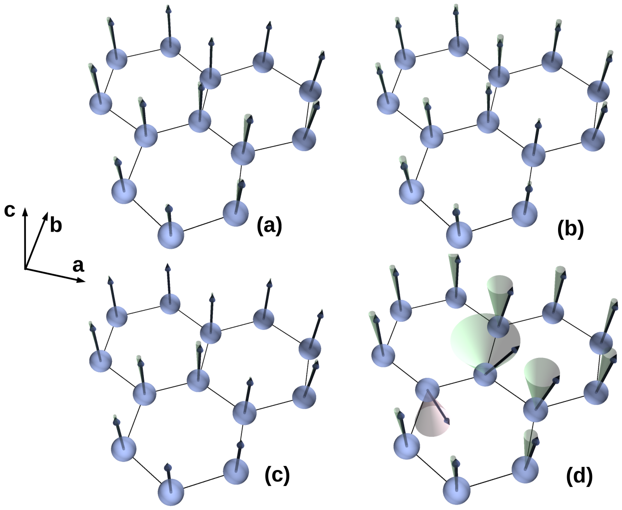

Figure 3.4: The canted spin states for each of the geometry optimized, Cl doped systems shown in Fig. 3.2, Cl_6:CrI_3 (a), Cl_3^a:CrI_3 (b), $Cl_2^aCl^b$:CrI_3 (c), and Cl:CrI_3 (d) resulting from the presence of the doped Cl. Magnetic vectors are shown by black vectors on each Cr atom. The difference between the canted spins and the collinear spins perpendicular to the crystal plane are shown by the cones (where green cones are spins above the layer and red cones are spins beneath the layer).

rotation (<1 meV/Cr).[165] Thus, similar to the skyrmions formed through the application of external fields, the spin bubbles are topologically-protected spin configurations. It is interesting to note that while able to form in the Cl:CrI_3 system, a spin bubble configuration is not manifested in the $Cl_2^aCl^b$:CrI_3 system. Even though, in the $Cl_2^aCl^b$:CrI_3 system, there is both a lack of symmetry in the geometry (as in either the Cl_6:CrI_3 or Cl_3^a:CrI_3 cases), and there exists a pathway with only a single Cl atom that has a similar geometric distortion to the Cl:CrI_3 system. This can be seen in Fig. 3.2g and Fig. 3.2h, with a 4.39% reduction in Cr-Cr distance for the $Cl_2^aCl^b$:CrI_3 compared to a 5.23% reduction for the Cl:CrI_3. It was previously noted that a minimum field was required in order to induce skyrmions which introduced a distortion between the Cr and I layers in the monolayer CrI_3.[165] Measuring geometric changes for the systems finds that the $Cl_2^aCl^b$:CrI_3 system has a distortion of 2.2% while the Cl:CrI_3 system has a distortion of 3.1%. Given that the distortion of the $Cl_2^aCl^b$:CrI_3 system is less than the previously determined minimum may contribute to why a magnetic bubble state is unable to manifest even though there are DMI vectors present.

In order to gain insights into the formation of the spin bubble in the Cl:CrI$_3$ system, the DMI vectors were calculated for the Cr atoms shown in Fig. 3.3. The numerical values for the DMI vectors have been tabulated in Tab. 3.2 and calculated through the four-state method detailed in Refs. 176 and 158. This method takes specific chromium pairs (labeled in the table) and directs their local spin orientations in order to extract the energetic values of the coupling between the select centers and their DMI vectors. For the Cl$_6$:CrI$_3$ and Cl$_3^a$:CrI$_3$ systems only the Cr$_1$ and Cr$_2$ pair were calculated due to the presence of the rotational symmetry. For the other systems, the DMI vectors for the nearest neighbors to the central Cr were all explicitly calculated. Previous work has identified that skyrmions are more likely to form when values of $^{D_{ij}}/_{J_{ij}}$ (where $D_{ij} = |\mathbf{D}_{ij}|$) are between 0.1-0.2 meV.[166, 176] Larger values of the $^{D_{ij}}/_{J_{ij}}$ value favors faster spin rotations about $\mathbf{D}_{ij}$ leading to smaller skyrmions.[166] Our values for $^{D_{ij}}/_{J_{ij}}$ are significantly larger than those reported for previous CrI$_3$ systems. This is most likely due to the increased localized distortion surrounding the Cr centers. The values for $|\mathbf{D}_{ij}|$ are also larger than those previously reported,[176] though it should be noted that large values for the DMI vectors have been shown in previous studies and will often introduce other spin configurations than skyrmions.[166] Although the Cl:CrI$_3$ (Cr$_1$,Cr$_3$) and Cl$_2^a$Cl^b:CrI$_3$ (Cr$_1$,Cr$_4$) systems are close in geometry and as such expected to both exhibit spin canted solutions, the Cl$_2^a$Cl^b:CrI$_3$ system has a $^{D_{1,4}}/_{J}$ value (tabulated in Tab. 3.2) that is too large to manifest a stable spin whirl solution at zero field. In contrast, while the value for $^{D_{ij}}/_{J}$ is larger than in other reports of skyrmion-forming monolayer chromium iodide systems, a spin canted solution is still able to manifest for the Cl:CrI$_3$ system.

3.5 Conclusion

We show that upon substituting select I atoms in a CrI$_3$ monolayer with Cl atoms, localized spin-bubble states form. These spin states arise from the lattice distortions induced by the ionic radii mismatch between the host and the defect species. While distortions are driven by the difference in the X-Cr bond lengths, the interactions between these distortions can induced long-range directional lattice polarization that may enable coupling between spatially-separated spin-bubble states. It was noted that when these spin-bubble systems formed they were topologically protected. They were significantly more stable than either the cost of a spin-flip or the stabilization noted by electric-field induced skyrmions. This work provided an important step toward manifesting skyrmions at conditions that would be useful for spintronic applications by potentially reducing the field required and increasing the operating temperature through controlled doping of CrI_3 monolayers.

BIBLIOGRAPHY

[1] A. Szabo and N. S. Ostlund. *Modern Quantum Chemistry: Introduction to Advanced Electronic Structure Theory.* Dover, New York, United States of America, first, revised edition, 1996.

[2] S. Reine and T. Saue, editors. *European Summerschool in Quantum Chemistry 2019.* Fotograph S.R.L, Palermo, Italy, eleventh edition, 2019.

[3] P. Hohenberg and W. Kohn. Inhomogeneous Electron Gas. *Phys. Rev.*, 136:B864–B871, 1964.

[4] W. Kohn and L. J. Sham. Self-Consistent Equations Including Exchange and Correlation Effects. *Phys. Rev.*, 140:A1133–A1138, 1965.

[5] A. D. Becke. Density-Functional Exchange-Energy Approximation with Correct Asymptotic Behavior. *Phys. Rev. A*, 38(6):3098, 1988.

[6] C. Lee, W. Yang, and R. G. Parr. Development of the Colle-Salvetti Correlation-Energy Formula into a Functional of the Electron Density. *Phys. Rev. B*, 37(2):785, 1988.

[7] J. P. Perdew, K. Burke, and M. Ernzerhof. Generalized gradient approximation made simple. *Phys. Rev. Lett.*, 77(18):3865–3868, 1996.

[8] A. D. Becke. Density-Functional Thermochemistry. III. The Role of Exact Exchange. *J. Chem. Phys.*, 98:5648, 1993.

[9] T. Yanai, D. P. Tew, and N. C. Handy. A New Hybrid Exchange-Correlation Functional Using the Coulomb-Attenuating Method (CAM-B3LYP). *Chem. Phys. Lett.*, 393(1):51–57, 2004.

[10] K. B. Holt. Diamond at the Nanoscale: Applications of Diamond Nanoparticles from Cellular Biomarkers to Quantum Computing. *Phil. Trans. R. Soc. A*, 365(1861): 2845–2861, 2007.

[11] F. Dolde, M. W. Doherty, J. Michl, I. Jakobi, B. Naydenov, S. Pezzagna, J. Meijer, P. Neumann, F. Jelezko, N. B. Manson, and J. Wrachtrup. Nanoscale Detection of a Single Fundamental Charge in Ambient Conditions Using the NV^- Center in Diamond. *Phys. Rev. Lett.*, 112:097603, Mar 2014.

[12] G. Balasubramanian, I. Y. Chan, R. Kolesov, M. Al-Hmoud, J. Tisler, C. Shin, C. Kim, A. Wojcik, P. R. Hemmer, A. Krueger, T. Hanke, A. Leitenstorfer, R. Bratschitsch, F. Jelezko, and J. Wrachtrup. Nanoscale Imaging Magnetometry with Diamond Spins Under Ambient Conditions. *Nature*, 455(7213):648–651, 2008.

[13] M. G. Bawendi, M. L. Steigerwald, and L. E. Brus. The Quantum Mechanics of Larger Semiconductor Clusters ("Quantum Dots"). *Annu. Rev. Phys. Chem.*, 41(1):477–496, 1990.

[14] T. A. Cohen, T. J. Milstein, D. M. Droupa, J. D. MacKenzie, and C. K. Luscombe. Quantum-Cutting Yb^{3+}-Doped Perovskite Nanocrystals for Monolithic Bilayer Luminescent Solar Concentrators. *J. Mater. Chem. A*, 7:9279–9288, 2019.

[15] K. E. Hughes, J. L. Stein, M. R. Friedfeld, B. M. Cossairt, and D. R. Gamelin. Effects of Surface Chemistry on the Photophysics of Colloidal InP Nanocrystals. *ACS Nano*, 13:14198–14207, 2019.

[16] G. Galli. *Structure, Stability and Electronic Properties of Nanodiamonds*, pages 37–56. Springer, Dordrecht, the Netherlands, 2010. ISBN 978-1-4020-9718-8.

[17] V. Mortet, L. Zhang, M. Eckert, J. D'Haen, A. Soltani, M. Moreau, D. Troadec, E. Neyts, J.-C. D. Jaeger, J. Verbeeck, A. Bogaerts, G. V. Tendeloo, K. Haenen, and P. Wagner. Grain Size Tuning of Nanocrystalline Chemical Vapor Deposited Diamond by Continuous Electrical Bias Growth: Experimental and Theoretical Study. *Phys. Status Solidi A*, 209:1675–1682, 2012.

[18] S. Pezzagna, D. Rogalla, D. Wildanger, J. Meijer, and A. Zaitsev. Creation and Nature of Optical Centres in Diamond for Single-Photon Emission-Overview and Critical Remarks. *New J. Phys.*, 13(3):035024, 2011.

[19] T. Karin, S. Dunham, and K.-M. Fu. Alignment of the Diamond Nitrogen Vacancy Center by Strain Engineering. *Appl. Phys. Lett.*, 105(5):053106, 2014.

[20] M. Drake, E. Scott, and J. A. Reimer. Influence of Magnetic Field Alignment and Defect Concentration on Nitrogen-Vacancy Polarization in Diamond. *New J. Phys.*, 18(1):013011, 2015.

[21] M. E. Levinshteĭn, S. L. Rumyantsev, and M. Shur. *Handbook Series on Semiconductor Parameters: Si, Ge, C (Diamond), GaAs, GaP, GaSb, InAs, InP, InSb.* World Scientific Publishing, Singapore, 1996.

[22] C. Kittel and P. McEuen. *Introduction to Solid State Physics*, volume 8. Wiley, New York, NY, 1976.

[23] N. W. Ashcroft and N. D. Mermin. *Solid State Physics.* Saunders College, Philadelphia, PA, 1976.

[24] L. E. Brus. Electron-Electron and Electron-Hole Interactions in Small Semiconductor Crystallites: The Size Dependence of the Lowest Excited Electronic State. *J. Chem. Phys.*, 80(9):4403–4409, 1984.

[25] J. R. Chelikowsky, M. M. G. Alemany, T.-L. Chan, and G. M. Dalpian. Computational Studies of Doped Nanostructures. *Rep. Prog. Phys.*, 74(4):046501, 2011.

[26] R. Beaulac, S. T. Ochsenbein, and D. R. Gamelin. Colloidal Transition-Metal-Doped Quantum Dots. In V. I. Klimov, editor, *Semiconductor Quantum Dots*, chapter 11, page 397. CRC Press, 2 edition, 2010.

[27] L. Canham. Gaining Light from Silicon. *Nature*, 408:411–412, 2000.

[28] J. Chelikowsky. Silicon in All Its Forms. *MRS Bull.*, 27:951, 2002.

[29] J. Chelikowsky. Why Silicon is the Benchmark. *Mater. Today*, 5:64, 2002.

[30] J. R. Chelikowsky and M. L. Cohen. Electronic Structure of GaAs. *Phys. Rev. Lett.*, 32:674–677, 1974.

[31] A. Petrone, J. J. Goings, and X. Li. Quantum Confinement Effects on Optical Transitions in Nanodiamonds Containing Nitrogen Vacancies. *Phys. Rev. B*, 94:165402, 2016.

[32] A. Gali and J. R. Maze. Ab Initio Study of the Split Silicon-Vacancy Defect in Diamond: Electronic Structure and Related Properties. *Phys. Rev. B*, 88:235205, Dec 2013.

[33] P. J. Pauzauskie, J. C. Crowhurst, M. A. Worsley, T. A. Laurence, A. L. D. Kilcoyne, Y. Wang, T. M. Willey, K. S. Visbeck, S. C. Fakra, W. J. Evans, J. M. Zaug, and J. H. Satcher. Synthesis and Characterization of a Nanocrystalline Diamond Aerogel. *Proc. Natl. Acad. Sci. U.S.A.*, 108(21):8550–8553, 2011.

[34] A. Petrone, R. A. Beck, J. M. Kasper, M. J. Crane, P. J. Pauzauskie, and X. Li. Electronic Structures and Spectroscopic Signatures of Silicon-Vacancy Containing Nanodiamonds. *Phys. Rev. B*, 98:205405, 2018.

[35] R. Beck, A. Petrone, J. M. Kasper, M. J. Crane, P. J. Pauzauskie, and X. Li. Effect of Surface Passivation on Nanodiamond Crystallinity. *J. Phys. Chem. C*, 122(15): 8573–8580, 2018.

[36] R. A. Beck, L. Lu, A. Petrone, A. C. Ong, P. J. Pauzauskie, and X. Li. Spectroscopic Signatures of the B and H_4 Polyatomic Nitrogen Aggregates in Nanodiamond. *J. Phys. Chem. C*, 124:18275–18283, 2020.

[37] J.-C. Arnault, T. Petit, H. Girard, A. Chavanne, C. Gesset, M. Sennour, and M. Chaigneau. Surface Chemical Modifications and Surface Reactivity of Nanodiamonds Hydrogenated by CVD Plasma. *Phys. Chem. Chem. Phys.*, 13:11481–11487, 2011.

[38] P. John and M. D. Stoikou. Hydrogen Plasma Interaction with (100) Diamond Surfaces. *Phys. Chem. Chem. Phys.*, 13:11503–11510, 2011.

[39] V. N. Mochalin, O. Shenderova, D. Ho, and Y. Gogotsi. The Properties and Applications of Nanodiamonds. *Nat. Nano.*, 7:11–23, 2012.

[40] M. Mandal, F. Haso, T. Liu, Y. Fei, and K. Landskron. Size Tunable Synthesis of Solution Processable Diamond Nanocrystals. *Chem. Commun.*, 50:11307–11310, 2014.

[41] K. Takahashi, A. Yoshikawa, and A. Sandhu. *Wide Bandgap Semiconductors: Fundamental Properties and Modern Photonic and Electronic Devices.* Springer, New York, NY, 2007.

[42] M. J. Frisch, G. W. Trucks, H. B. Schlegel, G. E. Scuseria, M. A. Robb, J. R. Cheeseman, G. Scalmani, V. Barone, G. A. Petersson, H. Nakatsuji, X. Li, M. Caricato, A. V. Marenich, J. Bloino, B. G. Janesko, R. Gomperts, B. Mennucci, H. P. Hratchian, J. V. Ortiz, A. F. Izmaylov, J. L. Sonnenberg, D. Williams-Young, F. Ding, F. Lipparini, F. Egidi, J. Goings, B. Peng, A. Petrone, T. Henderson, D. Ranasinghe, V. G. Zakrzewski, J. Gao, N. Rega, G. Zheng, W. Liang, M. Hada, M. Ehara, K. Toyota, R. Fukuda, J. Hasegawa, M. Ishida, T. Nakajima, Y. Honda, O. Kitao, H. Nakai, T. Vreven, K. Throssell, J. A. M. Jr, J. E. Peralta, F. Ogliaro, M. J. Bearpark, J. J. Heyd, E. N. Brothers, K. N. Kudin, V. N. Staroverov, T. A. Keith, R. Kobayashi, J. Normand, K. Raghavachari, A. P. Rendell, J. C. Burant, S. S. Iyengar, J. Tomasi, M. Cossi, J. M. Millam, M. Klene, C. Adamo, R. Cammi, J. W. Ochterski, R. L. Martin, K. Morokuma, O. Farkas, J. B. Foresman, and D. J. Fox. Gaussian 16 Revision B.01, 2016. Gaussian Inc. Wallingford CT 2016.

[43] M. E. Casida. *Recent Advances in Density Functional Methods:(Part I)*, volume 1. World Scientific Publishing, Singapore, 1995.

[44] A. Dreuw and M. Head-Gordon. Single-Reference Ab Initio Methods for the Calculation of Excited States of Large Molecules. *Chem. Rev.*, 105(11):4009–4037, 2005.

[45] R. E. Stratmann, G. E. Scuseria, and M. J. Frisch. An Efficient Implementation of Time-Dependent Density-Functional Theory for the Calculation of Excitation Energies of Large Molecules. *J. Chem. Phys.*, 109(19):8218–8224, 1998.

[46] W. Liang, S. A. Fischer, M. J. Frisch, and X. Li. Energy-Specific Linear Response TDHF/TDDFT for Calculating High-Energy Excited States. *J. Chem. Theor. Comput.*, 7(11):3540–3547, 2011.

[47] P. J. Lestrange, P. D. Nguyen, and X. Li. Calibration of Energy-Specific TDDFT for Modeling K-Edge XAS Spectra of Light Elements. *J. Chem. Theor. Comput.*, 11: 2994–2999, 2015.

[48] R. Van Beeumen, D. B. Williams-Young, J. M. Kasper, C. Yang, E. G. Ng, and X. Li. Model Order Reduction Algorithm for Estimating the Absorption Spectrum. *J. Chem. Theor. Comput.*, 13(10):4950–4961, 2017.

[49] S. L. Chang, C. Dwyer, E. Osawa, and A. S. Barnard. Size Dependent Surface Reconstruction in Detonation Nanodiamonds. *Nanoscale Horiz.*, 3:213–217, 2018.

[50] J.-Y. Raty, G. Galli, C. Bostedt, T. W. van Buuren, and L. J. Terminello. Quantum Confinement and Fullerenelike Surface Reconstructions in Nanodiamonds. *Phys. Rev. Lett.*, 90:037401, 2003.

[51] S. L. Y. Chang, A. S. Barnard, C. Dwyer, C. B. Boothroyd, R. K. Hocking, E. Ōsawa, and R. J. Nicholls. Counting Vacancies and Nitrogen-Vacancy Centers in Detonation Nanodiamond. *Nanoscale*, 8(20):10548–10552, 2016.

[52] B. Palosz, C. Pantea, E. Grzanka, S. Stelmakh, T. Proffen, T. W. Zerda, and W. Palosz. Investigation of Relaxation of Nanodiamond Surface in Real and Reciprocal Spaces. *Diamond Relat. Mater.*, 15(11):1813–1817, 2006.

[53] A.-L. Hamon, J. Verbeeck, D. Schryvers, J. Benedikt, and R. M. C. M. vd Sanden. ELNES Study of Carbon K-edge Spectra of Plasma Deposited Carbon Films. *J. Mater. Chem.*, 14(13):2030–2035, 2004.

[54] A. S. Barnard and M. Sternberg. Crystallinity and Surface Electrostatics of Diamond Nanocrystals. *J. Mater. Chem.*, 17:4811–4819, 2007.

[55] L. Lai and A. S. Barnard. Surface Phase Diagram and Thermodynamic Stability of Functionalisation of Nanodiamonds. *J. Mater. Chem.*, 22:16774–16780, 2012.

[56] L. Lai and A. S. Barnard. Site-Dependent Atomic and Molecular Affinities of Hydrocarbons, Amines, and Thiols on Diamond Nanoparticles. *Nanoscale*, 8:7899–7905, 2016.

[57] A. S. Barnard, S. P. Russo, and I. K. Snook. *Ab initio* Modeling of B and N in C_{29} and $C_{29}H_{24}$ Nanodiamond. *J. Chem. Phys.*, 118:10725–10728, 2003.

[58] B. Miehlich, A. Savin, H. Stoll, and H. Preuss. Results Obtained with the Correlation Energy Density Functionals of Becke and Lee, Yang and Parr. *Chem. Phys. Lett.*, 157 (3):200–206, 1989.

[59] X. Li and M. J. Frisch. Energy-Represented Direct Inversion in the Iterative Subspace within a Hybrid Geometry Optimization Method. *J. Chem. Theor. Comput.*, 2(3): 835–839, 2006.

[60] J. Filik, J. Harvey, N. Allan, and P. May. Raman Spectroscopy of Nanocrystalline Diamond: An ab initio Approach. *Phys. Rev. B*, 74:035423, 2006.

[61] W. Li, S. Irle, and H. A. Witek. Convergence in the Evolution of Nanodiamond Raman Spectra with Particle Size: A Theoretical Investigation. *ACS Nano*, 4(8):4475–4486, 2010.

[62] S. Prawer, I. Rosenblum, J. Orwa, and J. Adler. Identification of the Point Defects in Diamond as Measured by Raman Spectroscopy: Comparison Between Experiment and Computation. *Chem. Phys. Lett.*, 398:458–461, 2004.

[63] A. C. Ferrari and J. Robertson. Raman Spectroscopy of Amorphous, Nanostructured, Diamond–Like Carbon, and Nanodiamond. *Phil. Trans. R. Soc. A*, 362(1824):2477–2512, 2004.

[64] F. Negri, C. Castiglioni, M. Tommasini, and G. Zerbi. A Computational Study of the Raman Spectra of Large Polycyclic Aromatic Hydrocarbons: Toward Molecularly Defined Subunits of Graphite. *J. Phys. Chem.*, 106:3306–3317, 2002.

[65] M. Popov, V. Churkin, A. Kirichenko, V. Denisov, D. Ovsyannikov, B. Kulnitskiy, I. Perezhogin, V. Aksenenkov, and V. Blank. Raman Spectra and Bulk Modulus of Nanodiamond in a Size Interval of 2-5 nm. *Nanoscale Res. Lett.*, 12:561, 2017.

[66] V. Mochalin, S. Osswald, and Y. Gogotsi. Contribution of Functional Groups to the Raman Spectrum of Nanodiamond Powders. *Comp. Mater.*, 21:273–279, 2009.

[67] J. Cebik, J. K. McDonough, F. Peerally, R. Medrano, I. Neitzel, Y. Gogotsi, and S. Osswald. Raman Spectroscopy Study of the Nanodiamond to Carbon Onion Transformation. *Nanotechnology*, 24:205703, 2013.

[68] T. Ando, M. Ishii, M. Kamo, and Y. Sato. Diffuse Reflectance Infrared Fourier-Transform Study of the Plasma Hydrogenation of Diamond Surfaces. *J. Chem. Soc., Faraday Trans.*, 89:1383 – 1386, 1993.

[69] S. Stehlik, M. Varga, M. Ledinsky, V. Jirasek, A. Artemenko, H. Kozak, L. Ondic, V. Skakalova, G. Argentero, T. Pennycook, J. C. Meyer, A. Fejfar, A. Kromka, and B. Rezek. Size and Purity Control of HPHT Nanodiamonds dDown to 1 nm. *J. Phys. Chem. C*, 19(49):27708–27720, 2015.

[70] J. Birrell, J. Gerbi, O. Auciello, J. Gibson, J. Johnson, and J. Carlisle. Interpretation of the Raman Spectra of Ultrananocrystalline Diamond. *Diamond Relat. Mater.*, 14: 86–92, 2005.

[71] A. Ferari and J. Robertson. Origin of the 1150-cm^{-1} Raman Mode in Nanocrystalline Diamond. *Phys. Rev. B*, 63:121405(R), 2001.

[72] S. Reich and C. Thomsen. Raman Spectroscopy of Graphite. *Phil. Trans. R. Soc. A*, 362:2271 – 2288, 2004.

[73] O. O. Mykhaylyk and Y. M. Solonin. Transformation of Nanodiamond into Carbon Onions: A Comparative Study by High-Resolution Transmission Electron Microscopy, Electron Energy-Loss Spectroscopy, X-Ray Diffraction, Small-Angle X-Ray Scattering, and Ulraviolet Raman Spectroscopy. *J. Appl. Phys.*, 97:074302, 2005.

[74] M. Yoshikawa, Y. Mori, H. Obata, M. Maegawa, G. Katagiri, H. Ishida, and A. Ishitani. Raman Scattering from Nanometer-Sized Diamond. *Appl. Phys. Lett.*, 67: 694 – 696, 1995.

[75] S. Prawer and R. J. Nemanich. Raman Spectroscopy of Diamond and Doped Diamond. *Proc. R. Soc. London, Ser. A*, 362(1824):2537–2565, 2004.

[76] S. Prawer, K. W. Nugent, D. N. Jamieson, J. O. Orwa, L. A. Bursill, and J. L. Peng. The Raman Spectrum of Nanocrystalline Diamond. *Chem. Phys. Lett.*, 332(1):93–97, 2000.

[77] B. Andes Hess Jr. and L. J. Schaad. *Ab Initio* Second-Order Moller-Plesset Calculation of the Vibrational Spectrum of Tetrahedrane. *J. Am. Chem. Soc.*, 107:865–866, 1985.

[78] S. Masamune, F. A. Souto-Bachiller, T. Machiguchi, and J. E. Bertie. Cyclobutadiene Is Not Square. *J. Am. Chem. Soc.*, 100:4889 – 4891, 1978.

[79] T. Shimanouchi. *Tables of Molecular Vibrational Frequencies. Consolidated volume I.* National Bureau of Standards, U.S., Washington, DC, 1972.

[80] J. Stöhr. *NEXAFS Spectroscopy.* Springer-Verlag: Berlin, Heidelberg, Heidelberg, Germany, 2003.

[81] P. Castrucci, M. Scarselli, M. D. Crescenzi, M. A. E. Khakani, and F. Rosei. Probing the Electronic Structure of Carbon Nanotubes by Nanoscale Spectroscopy. *Nanoscale*, 2:1611–1625, 2010.

[82] A. J. Papworth, C. Kiely, A. Burden, S. Silva, and G. Amaratunga. Electron-Energy-Loss Spectroscopy Characterization of the sp^2 Bonding Fraction within Carbon Thin Films. *Phys. Rev. B*, 62:12628–12631, 2002.

[83] Y.-R. Chang, H.-Y. Lee, K. Chen, C.-C. Chang, D.-S. Tsai, C.-C. Fu, T.-S. Lim, Y.-K. Tzeng, C.-Y. Fang, C.-C. Han, H.-C. Chang, and W. Fann. Mass Production and Dynamic Imaging of Fluorescent Nanodiamonds. *Nat. Nano.*, 3(5):284–288, 2008.

[84] L. Mc Guinness, Y. Yan, A. Stacey, D. A. Simpson, L. T. Hall, D. Maclaurin, S. Prawer, P. Mulvaney, J. Wrachtrup, F. Caruso, R. E. Scholten, and L. C. L. Hollenberg. Quantum Measurement and Orientation Tracking of Fluorescent Nanodiamonds Inside Living Cells. *Nat. Nano.*, 6(6):358–363, 2011.

[85] K. Sasaki, E. E. Kleinsasser, Z. Zhu, W.-D. Li, H. Watanabe, K.-M. C. Fu, K. M. Itoh, and E. Abe. Dynamic Nuclear Polarization Enhanced Magnetic Field Sensitivity and Decoherence Spectroscopy of an Ensemble of Near-Surface Nitrogen-Vacancy Centers in Diamond. *Appl. Phys. Lett.*, 110(19):192407, 2017.

[86] N. Aslam, M. Pfender, P. Neumann, R. Reuter, A. Zappe, F. F. de Oliveira, A. Denisenko, H. Sumiya, S. Onoda, J. Isoya, and J. Wrachtrup. Nanoscale Nuclear Magnetic Resonance with Chemical Resolution. *Science*, page eaam8697, 2017.

[87] M. Leifgen, T. Schröder, F. Gödeke, R. Riemann, V. Metillon, E. Neu, C. Hepp, C. Arend, C. Becher, K. Lauritsen, and O. Benson. Evaluation of Nitrogen– and Silicon–Vacancy Defect Centres as Single Photon Sources in Quantum Key Distribution. *New J. Phys.*, 16(2):023021, 2014.

[88] E. Neu, D. Steinmetz, J. Riedrich-Möller, S. Gsell, M. Fischer, M. Schreck, and C. Becher. Single Photon Emission from Silicon–Vacancy Colour Centres in Chemical Vapour Deposition Nano–Diamonds on Iridium. *New J. Phys.*, 13(2):025012, 2011.

[89] A. Dietrich, K. D. Jahnke, J. M. Binder, T. Teraji, J. Isoya, L. J. Rogers, and F. Jelezko. Isotopically Varying Spectral Features of Silicon–Vacancy in Diamond. *New J. Phys.*, 16(11):113019, 2014.

[90] M. J. Crane, A. Petrone, R. A. Beck, M. B. Lim, X. Zhou, X. Li, R. M. Stroud, and P. J. Pauzauskie. High Pressure, High Temperature Molecular Doping of Nanodiamond. *Sci. Adv.*, 5:eaau6073, 2018.

[91] J. P. Goss, R. Jones, S. J. Breuer, P. R. Briddon, and S. Öberg. The Twelve-Line 1.682 eV Luminescence Center in Diamond and the Vacancy-Silicon Complex. *Phys. Rev. Lett.*, 77(14):3041, 1996.

[92] J. P. Goss, P. R. Briddon, and M. J. Shaw. Density Functional Simulations of Silicon-Containing Point Defects in Diamond. *Phys. Rev. B*, 76(7):075204, 2007.

[93] A. S. Zyubin, A. M. Mebel, M. Hayashi, H. C. Chang, and S. H. Lin. Quantum Chemical Modeling of Photoadsorption Properties of the Nitrogen-Vacancy Point Defect in Diamond. *J. Comput. Chem.*, 30(1):119–131, 2009.

[94] L. J. Rogers, K. D. Jahnke, M. W. Doherty, A. Dietrich, L. P. Mc Guinness, C. Müller, T. Teraji, H. Sumiya, J. Isoya, N. B. Manson, and F. Jelezko. Electronic Structure of the Negatively Charged Silicon-Vacancy Center in Diamond. *Phys. Rev. B*, 89: 235101, Jun 2014.

[95] T. Müller, C. Hepp, B. Pingault, E. Neu, S. Gsell, M. Schreck, H. Sternschulte, D. Steinmüller-Nethl, C. Becher, and M. Atatüre. Optical Signatures of Silicon-Vacancy Spins in Diamond. *Nat. Commun.*, 5:3328, 2014.

[96] I. I. Vlasov, A. A. Shiryaev, T. Rendler, S. Steinert, S.-Y. Lee, D. Antonov, M. Vörös, F. Jelezko, A. V. Fisenko, L. F. Semjonova, J. Biskupek, U. Kaiser, O. I. Lebedev, I. Sildos, P. R. Hemmer, V. I. Konov, A. Gali, and J. Wrachtrup. Molecular-Sized Fluorescent Nanodiamonds. *Nat. Nano.*, 9(1):54–58, 2014.

[97] C. D. Clark, H. Kanda, I. Kiflawi, and G. Sittas. Silicon Defects in Diamond. *Phys. Rev. B*, 51:16681–16688, Jun 1995.

[98] E. Neu, C. Hepp, M. Hauschild, S. Gsell, M. Fischer, H. Sternschulte, D. Steinmüller-Nethl, M. Schreck, and C. Becher. Low-Temperature Investigations of Single Silicon Vacancy Colour Centres in Diamond. *New J. Phys.*, 15(4):043005, 2013.

[99] C. Hepp, T. Müller, V. Waselowski, J. N. Becker, B. Pingault, H. Sternschulte, D. Steinmüller-Nethl, A. Gali, J. R. Maze, M. Atatüre, and C. Becher. Electronic Struc-

ture of the Silicon Vacancy Color Center in Diamond. *Phys. Rev. Lett.*, 112:036405, Jan 2014.

[100] G. Thiering and A. Gali. Ab Initio Magneto-Optical Spectrum of Group-IV – Vacancy Color Centers in Diamond. *arxiv*, page https://arxiv.org/abs/1804.07004, 2018.

[101] S. S. Moliver. Electronic Structure of Neutral Silicon-Vacancy Complex in Diamond. *Tech. Phys.*, 48(11):1449–1453, 2003.

[102] T. Feng and B. D. Schwartz. Characteristics and Origin of the 1.681 eV Luminescence Center in Chemical-Vapor-Deposited Diamond Films. *J. Appl. Phys.*, 73(3):1415–1425, 1993.

[103] G. Thiering and A. Gali. Complexes of Silicon, Vacancy, and Hydrogen in Diamond: A Density Functional Study. *Phys. Rev. B*, 92(16):165203, 2015.

[104] M. Vörös and A. Gali. Optical Absorption of Diamond Nanocrystals from Ab Initio Density-Functional Calculations. *Phys. Rev. B*, 80:161411(R), Oct 2009.

[105] T. Demján, M. Vörös, M. Palummo, and A. Gali. Electronic and Optical Properties of Pure and Modified Diamondoids Studied by Many-Body Perturbation Theory and Time-Dependent Density Functional Theory. *J. Chem. Phys.*, 141(6):064308, 2014.

[106] M. Kaviani, P. Deák, B. Aradi, T. Frauenheim, J.-P. Chou, and A. Gali. Proper Surface Termination for Luminescent Near-Surface NV Centers in Diamond. *Nano Lett.*, 14(8):4772–4777, 2014.

[107] C.-K. Lin, Y.-H. Wang, H.-C. Chang, M. Hayashi, and S. H. Lin. One-and Two-Photon Absorption Properties of Diamond Nitrogen-Vacancy Defect Centers: A Theoretical Study. *J. Chem. Phys.*, 129(12):124714, 2008.

[108] A. Gali. Time-Dependent Density Functional Study on the Excitation Spectrum of Point Defects in Semiconductors. *Phys. Status Solidi B*, 248(6):1337–1346, 2011.

[109] N. Mardirossian, J. A. Parkhill, and M. Head-Gordon. Benchmark Results for Empirical Post-GGA Functionals: Difficult Exchange Problems and Independent Tests. *Phys. Chem. Chem. Phys.*, 13:19325–19337, 2011.

[110] A. D. Laurent and D. Jacquemin. TD-DFT Benchmarks: A Review. *Int. J. Quant. Chem.*, 113(17):2019–2039, 2017.

[111] R. Derian, K. Tokár, B. Somogyi, A. Gali, and I. Štich. Optical Gaps in Pristine and Heavily Doped Silicon Nanocrystals: DFT versus Quantum Monte Carlo Benchmarks. *J. Chem. Theor. Comput.*, 13(12):6061–6067, 2017.

[112] H.-P. Komsa, T. T. Rantala, and A. Pasquarello. Finite-Size Supercell Correction Schemes for Charged Defect Calculations. *Phys. Rev. B*, 86:045112, Jul 2012.

[113] S. Veprˇek. Electronic and Mechanical Properties of Nanocrystalline Composites when Approaching Molecular Size. *Thin Solid Films*, 297(1):145–153, 1997.

[114] E. Badaeva, Y. Feng, D. R. Gamelin, and X. Li. Investigation of Pure and Co^{2+}-Doped ZnO Quantum Dot Electronic Structures Using the Density Functional Theory: Choosing the Right Functional. *New J. Phys.*, 10:055013, 2008.

[115] E. Badaeva, C. M. Isborn, Y. Feng, S. T. Ochsenbein, D. R. Gamelin, and X. Li. Theoretical Characterization of Electronic Transitions in Co^{2+}- and Mn^{2+}-Doped ZnO Nanocrystals. *J. Phys. Chem. C*, 113(20):8710–8717, 2009.

[116] J. W. May, J. Ma, E. Badaeva, and X. Li. Effect of Excited-State Structural Relaxation on Midgap Excitations in Co^{2+}-Doped ZnO Quantum Dots. *J. Phys. Chem. C*, 118 (24):13152–13156, 2014.

[117] H. Sternschulte, K. Thonke, J. Gerster, W. Limmer, R. Sauer, J. Spitzer, and P. C. Münzinger. Uniaxial Stress and Zeeman Splitting of the 1.681 eV Optical Center in a Homoepitaxial CVD Diamond Film. *Diamond Relat. Mater.*, 4(10):1189–1192, 1995. ISSN 0925-9635.

[118] E. Neu, M. Fischer, S. Gsell, M. Schreck, and C. Becher. Fluorescence and Polarization Spectroscopy of Single Silicon Vacancy Centers in Heteroepitaxial Nanodiamonds on Iridium. *Phys. Rev. B*, 84:205211, 2011.

[119] S. W. Brown and S. C. Rand. Site Symmetry Analysis of the 738 nm Defect in Diamond. *J. Appl. Phys.*, 78(6):4069–4075, 1995.

[120] S. Salustro, A. Erba, C. M. Zicovich-Wilson, Y. Nöel, L. Maschio, and R. Dovesi. Infrared and Raman Spectroscopic Features of the Self-Interstitial Defect in Diamond from Exact-Exchange Hybrid DFT Calculations. *Phys. Chem. Chem. Phys.*, 18:21288–21295, 2016.

[121] J. Bielecki and E. W. Lipiec. Basis Set Dependence Using DFT/B3LYP Calculations to Model the Raman Spectrum of Thymine. *J Bioinform Comput Biol*, 14:1650002, 2016.

[122] J. R. Cheeseman and M. J. Frisch. Basis Set Dependence of Vibrational Raman and Raman Optical Activity Intensities. *J. Chem. Theor. Comput.*, 7:3323–3334, 2011.

[123] F. Billes. A Systematic Study on the Basis Set Dependence of the Hartree-Fock, MP2 and CIS Harmonic Force Fields and Vibrational Frequencies of Formaldehyde in Comparison with the Experimental Results. *J. Mol. Struct.*, 339:15–24, 1995.

[124] J. Filik, J. N. Harvey, N. L. Allan, P. W. May, J. E. P. Dahl, S. Liu, and R. M. K. Carlson. Raman Spectroscopy of Nanocrystalline Diamond: An Ab Initio Approach. *Phys. Rev. B*, 74(3):035423, 2006.

[125] J. Cebik, J. K. McDonough, F. Peerally, R. Medrano, I. Neitzel, Y. Gogotsi, and S. Osswald. Raman Spectroscopy Study of the Nanodiamond-to-Carbon Onion Transformation. *Nanotechnology*, 24(20):205703, 2013.

[126] V. I. Korepanov, H. o Hamaguchi, E. Osawa, V. Ermolenkov, I. K. Lednev, B. J. M. Etzold, O. Levinson, B. Zousman, C. P. Epperla, and H.-C. Chang. Carbon Structure in Nanodiamonds Elucidated from Raman Spectroscopy. *Carbon*, 121(Supplement C): 322 – 329, 2017. ISSN 0008-6223.

[127] G. J. Wan, P. Yang, R. K. Y. Fu, Y. F. Mei, T. Qiu, S. C. H. Kwok, J. P. Y. Ho, N. Huang, X. L. Wu, and P. K. Chu. Characteristics and Surface Energy of Silicon-Doped Diamond-Like Carbon Films Fabricated by Plasma Immersion Ion Implantation and Deposition. *Diamond Relat. Mater.*, 15(9):1276–1281, 2006.

[128] S.-l. Chen, S. Bin, J.-G. Zhang, W. Liang, and F.-H. Sun. Evaluation on Residual Stresses of Silicon-Doped CVD Diamond Films Using X-Ray Diffraction and Raman Spectroscopy. *Trans. Nonferrous Met. Soc. China*, 22(12):3021–3026, 2012.

[129] Y.-X. Cui, J.-G. Zhang, F.-H. Sun, and Z.-M. Zhang. Si-Doped Diamond Films Prepared by Chemical Vapour Deposition. *Trans. Nonferrous Met. Soc. China*, 23 (10):2962–2970, 2013.

[130] M. Berglund and M. E. Wieser. Isotopic Compositions of the Elements 2009 (IUPAC Technical Report). *Pure Appl. Chem.*, 83(2):397–410, 2011.

[131] H. Moseley. XCIII. The High–Frequency Spectra of the Elements. *The London, Edinburgh, and Dublin Philosophical Magazine and Journal of Science*, 26(156):1024–1034, 1913.

[132] H. Moseley. The High-Frequency Spectra of the Elements. Part II. *The London, Edinburgh, and Dublin Philosophical Magazine and Journal of Science*, 27(160):703–713, 1914.

[133] A. Nilsson and L. G. M. Pettersson. Chemical Bonding on Surfaces Probed by X-Ray Emission Spectroscopy and Density Functional Theory. *Surf. Sci. Rep.*, 55(2):49 – 167, 2004.

[134] N. B. Manson and J. P. Harrison. Photo-ionization of the nitrogen-vacancy center in diamond. *Diamond Relat. Mater.*, 14(10):1705–1710, 2005.

[135] C. Bradac, T. Gaebel, N. Naidoo, M. J. Sellars, J. Twamley, L. J. Brown, A. S. Barnard, T. Plakhotnik, A. V. Zvyagin, and J. R. Rabeau. Observation and Control of Blinking Nitrogen-Vacancy Centres in Discrete Nanodiamonds. *Nat. Nano.*, 5(5): 345–349, 2010.

[136] N. B. Manson, K. Beha, A. Batalov, L. J. Rogers, M. W. Doherty, R. Bratschitsch, and A. Leitenstorfer. Assignment of the NV 0 575-nm zero-phonon line in diamond to a 2 E-2 A 2 transition. *Phys. Rev. B*, 87(15):155209, 2013.

[137] A. Ranjbar, M. Babamoradi, M. H. Saani, M. A. Vesaghi, K. Esfarjani, and Y. Kawazoe. Many-Electron States of Nitrogen-Vacancy Centers in Diamond and Spin Density Calculations. *Phys. Rev. B*, 84(16):165212, 2011.

[138] M. W. Doherty, N. B. Manson, P. Delaney, F. Jelezko, J. Wrachtrup, and L. C. L. Hollenberg. The Nitrogen-Vacancy Colour Centre in Diamond. *Phys. Rep.*, 528(1): 1–45, 2013.

[139] P. Deák, B. Aradi, M. Kavani, T. Frauenheim, and A. Gali. Formation of NV Centers in Diamond: A Theoretical Study Based on Calculated Transitions and Migration of Nitrogen and Vacancy Related Defects. *Phys. Rev. B*, 89:07203, 2014.

[140] A. Gali. *Ab initio* Theory of the Nitrogen-Vacancy Center in Diamond. *Nanophotonics*, pages 01–37, 2019.

[141] R. Jones, P.R.Briddon, and S. Öberg. First-principles Theory of Nitrogen Aggregates in Diamond. *Philos. Mag. Lett.*, 66:67–74, 1992.

[142] G. Davies. Dynamic Jahn-Teller distortions at trigonal optical centres in diamond. *J. Phys. C Solid State*, 12(13):2551–2566, 1979.

[143] M. I. Rakhmanova, V. A. Nadolinna, O. P. Yuryeva, N. P. Pokhilenko, and A. M. Logvinova. Peculiarities of Nitrogen Impurity Aggregation in Diamonds from the Sytykanskaya Pipe, Yakutia. *Eur. J. Mineral*, 27:51–56, 2014.

[144] R. Jones, V. Torres, P. Briddon, and S. Öberg. Theory of Nitrogen Aggregates in Diamond: The H3 and H4 Defects. *Mater. Sci. Forum*, 143-147:45–50, 1994.

[145] S. Salustro, A. M. Ferrari, F. S. gentile, J. kontak Desarais, M. R‘erat, and R. Dovesi. Characterization of the B-Center Defect in Diamond Through the Vibrational Spectrum: A Quantum-Mechanical Approach. *J. Phys. Chem. A*, 122:594–600, 2018.

[146] A. Mainwood. Nitrogen and Nitrogen-Vacancy Complexes and their Formation in Diamond. *Phys. Rev. B*, 49:7934–7941, 1994.

[147] J. A. Pople and D. L. Beveridge. *Approximate Molecular Orbital Theory.* McGraw-Hill, New York, USA, 1970.

[148] V. Vins and A. Eliseev. Effect of Annealing at High Pressures and Temperatues on the Defect-Admixture Structure of Natural Diamonds. *Inorg. Mat. App. Research*, 1: 303–310, 2010.

[149] J. A. Hachtel, J. Huang, I. Popovs, S. Jansone-Popova, J. K. Keum, J. Jakowski, T. C. Lovejoy, N. Delby, O. L. Krivanek, and J. C. Idrobo. Identification of Site-Specific Isotopic Labels by Vibrational Spectroscopy in the Electron Microscope. *Science*, 363: 525–528, 2019.

[150] Z. Li, K. Aleshire, M. Kuno, and G. V. Hartland. Super-Resolution Far-Field Infrared Imaging by Photothermal Heterodyne Imaging. *Phys. Rev. B*, 121:8838–8846, 2017.

[151] R. L. Martin. Natural Transition Orbitals. *J. Chem. Phys.*, 118:4775–4777, 2003.

[152] A. Vairavamurthy and S. Wang. Organic Nitrogen in Geomacromolecules: Insights on Speciation and Transformation with K-edge XANES Spectroscopy. *Environ. Sci. Technol.*, 36:3050–3056, 2002.

[153] T. Saue. Relativistic Hamiltonians for Chemistry: A Primer. *Comp. Phys. Comm.*, 12:3077–3094, 2011.

[154] T. F. Stetina, J. M. Kasper, and X. Li. Modeling $L_{2,3}$-Edge X-ray Absorption Spectroscopy with Linear Response Exact Two-Component Relativistic Time-Dependent Density Functional Theory. *J. Phys. Chem. A*, 150:234103, 2019.

[155] J. L. Lado and J. Fernández-Rossier. On the Origin of Magnetic Anisotropy in Two Dimensional CrI_3. *2D Mater.*, 4:035002, 2017.

[156] J. Liu, M. Shi, J. Lu, and M. P. Anantram. Analysis of Electrical-Filed-Dependent Dzyaloshinskii-Moriya Interaction and Magnetocrystalline Anisotropy in a Two-Dimensional Ferromagnetic Monolayer. *Phys. Rev. B*, 97:054416, 2018.

[157] F. Keffer. Moriya Interaction and the Problem of the Spin Arrangements in βMnS. *Phys. Rev.*, 126:896–900, 1961.

[158] C. Xu, J. Feng, H. Xiang, and L. Bellaiche. Interplay Between Kitaev Interaction and Single Ion Anisotropy in Ferromagnetic CrI_3 and $CrGeTe_3$ Monolayers. *Comp. Mater.*, page 57, 2018.

[159] T. Saue. Spin-Interactions and the Non-relativistic Limit of Electrodynamics. *Adv. Quantum Chem.*, 48:383–405, 2005.

[160] C. G. Darwin. LI. The Dynamical Motions of Charged Particles. *Phi. Mag.*, 39: 537–551, 1920.

[161] G. J. Arthur. The Triplets of Helium. *Proc. R. Soc. Lond. A*, 122:513–532, 1929.

[162] R. A. Beck, L. Lu, P. V. Sushko, X. Xu, and X. Li. Defect-Induced Magnetic Skyrmion in a Two-Dimensional Chromium Triiodide Monolayer. *J. Am. Chem. Soc. Au*, Article ASAP, 2021.

[163] A. Fert, N. Reyren, and V. Cros. Magnetic Skyrmions: Advances in Physics and Potential Applications. *Nat. Rev.*, 2:17031, 2017.

[164] A. B. Bogatyrëv and K. L. Metlov. What Makes Magnetic Skyrmions Different from Magnetic Bubbles? *J. Magn. Magn. Mater.*, 465:743–746, 2018.

[165] J. Liu, M. Shi, P. Mo, and J. Lu. Electrical-Field-Induced Magnetic Skyrmion Ground State in a Two-Dimensional Chromium Tri-Iodide Ferromagnetic Monolayer. *AIP Advances*, 8:055316, 2018.

[166] A. Fert, V. Cros, and J. Sampaio. Skyrmions on the Track. *Nat. Nano.*, 8:152–156, 2013.

[167] B. Ding, Z. Li, G. Xu, H. Li, Z. Hou, E. Liu, X. Xi, F. Xu, Y. Yao, and W. Wang. Observation of Magnetic Skyrmion Bubbles in a Van der Waals Ferromagnet Fe_3GeTe_2. *Nano Lett.*, 20:868–873, 2020.

[168] T. Moriya. Anisotropic Superexchange Interaction and Weak Ferromagnetism. *Phys. Rev.*, 120:91–98, 1960.

[169] M. A. McGuire, hemant Dixit, V. R. Cooper, and B. C. Sales. Coupling of Crystal Structure and Magnetism in the Layered Ferromagnetic Insulator CrI_3. *Comp. Mater.*, 27:612–620, 2015.

[170] M. A. McGuire. Crystal and Magnetic Structures in Layered, Transition Metal Dihalides and Trihalides. *Crystals*, 7:121, 2017.

[171] B. Huang, G. Clark, E. Navarro-Moratalla, D. R. Klien, R. Cheng, K. L. Seyler, D. Zhong, E. Schmidgall, M. A. McGuire, D. H. Cobden, W. Yao, D. Xiao, P. Jarillo-Herrero, and X. Xu. Layer-Dependent Ferromagnetism in a Van der Waals Crystal Down to the Monolayer Limit. *Nature*, 546:270–273, 2017.

[172] B. Huang, genevieve Clark, D. R. Klein, D. MacNeil, E. Navarro-Moratalla, K. L. Seyler, N. Wilson, M. A. McGuire, D. H. Cobden, D. Xiao, W. yao, P. Jarillo-Herrero, and X. Xu. Electrical Control of 2D Magnetism in Bilayer CrI_3. *Nat. Nanotechnol.*, 13:544–548, 2018.

[173] T. Song, Z. Fei, M. Yankowitz, Z. Lin, Q. Jiang, K. Hwangbo, Q. Zhang, B. Sun, T. Taniguchi, K. Watanabe, M. A. McGuire, D. Graf, T. Cao, J.-H. Chu, D. H. Cobden, C. R. Dean, D. Xiao, and X. Xu. Switching 2D Magnetic States via Pressure Tuning of layer Stacking. *Nat. Mater.*, pages 1476–4660, 2019.

[174] N. Sivadas, S. Okamoto, X. Xu, C. J. Fennie, and D. Xiao. Stacking-Dependent Magnetism in Bilayer CrI_3. *Nano Lett.*, 18:7658–7664, 2018.

[175] C. Lee, H. Y. Kwon, N. J. Kim, H. G. Yoon, C. Song, D. B. Lee, J. W. Choi, Y.-W. Son, and C. Won. Magnetic Structures in the Locally Inverted Interlayer Coupling Region of a Bilayer Magnetic System. *J. Magn. Magn. Mater.*, 501:166447, 2020.

[176] C. Xu, J. Feng, S. Prokhorenko, Y. Nahas, H. Xiang, and L. Bellaiche. Topological Spin Texture in Janus Monolayers of the Chromium trihalides Cr(I,X)$_3$. *Phys. Rev. B*, page 060404, 2020.

[177] C. Felser, G. H. Fecher, and B. Balke. Spintronics: A Challenge for Materials Science and Solid-State Chemistry. *Angew. Chem.*, 46:688–699, 2007.

[178] B. Behin-Aein, J.-P. Wang, and R. Wiesendanger. Computing with Spins and Magnets. *MRS Bull.*, 39:696–702, 2014.

[179] L. L. Handy and N. W. Gregory. A Study of the Chromous-Chromic Iodide Equilibrium. *J. Am. Chem. Soc.*, pages 5049–5051, 1950.

[180] N. D. Mermin and H. Wagner. Absence of Ferromagnetism or Antiferromagnetism in One- or Two- Dimensional Isotropic Heisenberg Models. *Phys. Rev. Lett.*, 17:1133, 1966.

[181] P. W. Anderson. Antiferromagnetism, Theory of Superexchange Interaction. *Phys. Rev.*, 79:350–356, 1950.

[182] A. K. Behera, S. Chowdhury, and S. R. Das. Magnetic Skyrmions in Atomic This CrI$_3$ Monolayer. *Appl. Phys. Lett.*, page 232402, 2019.

[183] R. Albaridy, A. Manchon, and U. Schwingenschlögl. Tunable Magnetic Anisotropy in Cr-Trihalide Janus Monolayers. *J. Phys.–Condens. Mat.*, 32:355702, 2020.

[184] G. Kresse and J. Furthmüller. Efficiency of Ab-Initio Total Energy Calculations for Metals and Semiconductors Using a Plane-Wave Basis Set. *Comput. Mater. Sci.*, 6: 15–50, 1996.

[185] G. Kresse and J. Furthmüller. Efficient Iterative Schemes for *ab initio* Total-Energy Calculations Using a Plane-Wave Basis Set. *Phys. Rev. B*, 54:11169, 1996.

[186] P. E. Blöchl. Projector Augmented-Wave Method. *Phys. Rev. B*, 50:17953, 1994.

[187] S. Grimme, J. Antony, S. Ehrlich, and S. Krieg. A Consistent and Accurate *ab initio* Parametrization of Density Functional Dispersion Correction (DFT-D) for the 94 elements H-Pu. *J. Chem. Phys.*, 132:154104, 2010.

[188] C. Wang, Y. gao, H. Lv, X. Xu, and D. Xiao. Stacking Domain Wall Magnons in Twisted van der Waals Magnets. *Phys. Rev. Lett.*, page 247201, 2020.